Long-range Interactions Between Ultracold Rydberg Atoms and the Formation Properties of Long-range Rydberg Molecules

Nolan S. Samboy, Ph.D.
University of Connecticut, 2011

The work presented in this dissertation represents a comprehensive study on long-range interactions between alkali Rydberg atoms. As a consequence of their size, Rydberg atoms possess very large dipole moments, making them highly sensitive to external fields and to other Rydberg atoms. The strong dipole-dipole interaction between two Rydberg atoms results in a mixing of their angular momentum characters, which is the cornerstone of the work presented here. We describe the ℓ-mixing between various local molecular asymptotes through a residual Coulomb potential, assuming no electron cloud overlap. We then directly diagonalize an interaction Hamiltonian consisting of these Rydberg-Rydberg interactions and spin-orbit (fine structure) coupling in the Hund's case (c). In this manner, we calculate potential energy curves for various molecular symmetries and find that some of these curves exhibit deep potential wells, capable of supporting very extended bound molecular states (*macrodimers*). We analyze the specific structure of the ℓ-mixing for these potential wells and derive convenient n-scaling relations for both their equilibrium separations R_e and well depths D_e. We also explore various properties of the macrodimers, including their response to small electric fields and stability with respect to predissociation. We note throughout the dissertation that the detection of such extended dimers could help progress studies in a variety of areas such as exotic, ultracold chemistry and quantum information and computing. To facilitate detection, we propose a scheme to form and study the macrodimers *via* photoassociation (PA). We present calculated PA lineshapes from two different electronic ground states based on a harmonic trapping model. We find that both PA signals vary significantly with the laser detunings, indicating that different ℓ-characters could be probed at different equilibrium lengths. Finally, we extend the two-body formalism to the case of three interacting Rydberg atoms and present preliminary results for triply excited $58p$ rubidium atoms along a common axis. We provide a few examples of surface plots corresponding to different local asymptotes, each with a unique three-dimensional "landscape" and discuss the relevance of the physical features. The highlight of our analysis is the appearance of a potential well, which indicates the formation of a linear trimer.

Long-range Interactions Between Ultracold Rydberg Atoms and the Formation Properties of Long-range Rydberg Molecules

Nolan S. Samboy
B.S. Siena College, Loudonville, NY 2004
M.S. University of Connecticut, Storrs, CT 2009

A Dissertation
Submitted in Partial Fulfillment of the
Requirements for the Degree of
Doctor of Philosophy
at the
University of Connecticut

2011

ProQuest LLC
789 East Eisenhower Parkway
P.O. Box 1346
Ann Arbor, MI 48106-1346

APPROVAL PAGE

Doctor of Philosophy Dissertation

Long-range Interactions Between Ultracold Rydberg Atoms and the Formation Properties of Long-range Rydberg Molecules

Presented by

Nolan S. Samboy, B.S., M.S.

Major Advisor

Robin Côté

Associate Advisor

Juha Javanainen

Associate Advisor

Susanne Yelin

University of Connecticut

2011

To my wife and family for their unconditional love, support, and patience during this process, and to Dr. Joshua B. Diamond for his unparalleled dedication, enthusiasm, and generosity.

“If I have seen further, it is only by standing on the shoulders of giants.”

- Isaac Newton

ACKNOWLEDGEMENTS

I have always been a pretty self-motivated person, but that will only get you so far when pursuing something as rigorous as a PhD. I would like to take this time to thank everyone who helped me through this amazing journey.

Firstly, I wish to thank my advisor, Robin Côté for taking me on as a graduate student and allowing me the opportunity to study among such distinguished faculty. Robin has always been very supportive of all of my professional and personal efforts and has been a great confidant with regard to my academic career. For those who don't know him that well, Robin is particularly gifted at explaining complicated material in a very comprehensive and visual manner and I have learned a lot under his guidance. I thank him for his academic, professional, and financial support over the years and for always treating me with kindness and respect.

I would also like to thank my associate advisors Juha Javanainen and Susanne Yelin. I had the priveledge of taking multiple classes with both of these professors and I deeply appreciate their dedication and passion for teaching physics. I thank them both for their time, energy, and overall amiability with respect to writing recommendation letters, meeting deadlines, and other such tasks associated with advisement. I especially want to thank Juha for his careful reading of the early draft of this dissertation and for his insightful suggestions. I found comments such as "nonsense sentence," "this chapter is probably hogwash," and "this expression is total trash and means nothing," particularly helpful.

In addition to my advisors, there are various faculty and staff members who helped me significantly along the way. I wish to thank Barry Wells for his friendship and advice; his door was always open to me, even though I was not his student. I also want to thank professors Stwalley, Eyler, Gould and Rawitscher for their input regarding my thesis work and professor Gibson for allowing me the opportunity to lecture. I thank the physics main office staff: especially Kim Giard, Lorraine Smurra, and Dawn Rawlinson for their patience, kindness, and professionalism towards me. Additionally, I very much thank Michael Rozman for all of his computer help, Carol Artacho-Guerra and Mike Rapposch for their assistance with the undergraduate labs, and Dave Perry for his input and suggestions with regard to lecturing and course demos.

I was fortunate to have worked with a tremendously talented group of students during my tenure at the University of Connecticut. In particular, I would like to acknowledge Tim "Tank" Bragdon, Jen Carini, Han Chen, Phil Gee, Wes Gohn, "Jimmy James" O'Brien, Renuka Rajapakse, Ila Sivarajah, Margo Staruch, and Anne Wrigley. I also would like to thank the members of our research group (both past and present) for their camaraderie and giving nature. My sincerest thanks to Jovica Stanojevic for his correspondence and assistance on the Rydberg project. Even though he had graduated, Jovica always had time for my questions and did his best to answer them through e-mails. In addition, I wish to thank Jason Byrd, Marko Gacessa, and Ionel Simbotin for all of their computer-related assistance. Many a time they helped me resolve linux issues that I never would have resolved on my own. I only hope that I have learned enough from them to survive without them!

My time at UCONN would not have been the same without the amazing set of friends that I have made. It is my great honor to acknowledge Sandipan and Jayita Banerjee, Drew Chieda, Sam Emery, Ting-Yu Huang, Naim Majdalani, J.C. Sanders, Kate Sekula, Ben and Jen Steinhurst and Don Telesca. Your support, friendship, and collaborative spirits are all evidenced in this dissertation. You are all family to me and I hope that we keep in touch.

Finally, I wish to thank my family without whom, none of this would have been possible. I especially thank my parents for providing me with everything that I have ever needed and for always stressing the importance of education. I would also like to take the opportunity to thank my wife's parents, who graciously welcomed me into their family and have been a great source of support, advice, and guidance. I thank my brother, Bret for his constant encouragement, support, and companionship, and my other "brother" Daryl for his unconditional friendship, love, and for introducing me to *Star Trek* all those years ago. I also thank my best friends Nick and Kevin and their families for all of the great memories and years of friendship. Lastly, I thank my beautiful wife, Anagha. She has been absolutely wonderful during this process, exhibiting immense patience and understanding. Without her, my accomplishments would be nowhere near as fulfilling or satisfying. I love you all and can never thank you enough.

TABLE OF CONTENTS

LIST OF FIGURES

LIST OF TABLES

Chapter 1

Introduction

1.1 Rydberg atoms

A Rydberg atom is an excited atom in which the valence electrons have very high principle quantum numbers. Although Rydberg states have been achieved *via* the excitation of multiple electrons [1], this dissertation studies the more traditional Rydberg atom: a single valence electron that has been excited very far from the core. In principle, any atom can be excited into a Rydberg state, but neutral alkali atoms are the most common candidates. Alkali metals are ideal for Rydberg atoms because they inherently have one electron in their outermost shell, making the excitation to a high orbital easier to perform experimentally. The excitation of a single electron leads to exaggerated atomic properties, such as long lifetimes, large cross-sections and very large polarizabilities [2], yet the atoms' neutrality allows for minimal interaction with the environment while in the ground state [3, 4]. The ability to control these atomic interactions by exciting trapped atoms at will has led to quantum information proposals involving entangled states [5].

Exciting a single electron to such a high orbital state leads to the Rydberg atom being very similar to hydrogen: one valence electron orbits a nucleus of overall +1 charge. For this reason, the potential energy of the atom is conveniently described by the $1/r$ Coulombic potential and thus the total energy of the Rydberg atom is very similar in form to that of the hydrogen atom (see Chapter 2). This similarity to hydrogen also means that the semi-classical Bohr model can be used to analyze many of their atomic properties. For example, equating the centripetal force of the orbiting electron with the Coulombic force between the electron and the core leads to a scaling relation between the orbital radius of the electron r_n and principal quantum number n, *i.e.* $r_n = a_0 n^2$, where a_0 is the Bohr radius. This expression indicates that the electron's excitation to a high n level corresponds to it being very far away from the nucleus. This makes the Rydberg atom especially responsive to electric and magnetic fields, as well as to other Rydberg atoms.

1.2 Summary of previous work

Strong Rydberg-Rydberg interactions have fueled immense interest in the field of quantum computing and over the past ten years, proposals such as fast quantum gates [6, 7] and quantum random walks [8] have been developed. Also of particular interest is the excitation blockade effect [9], where one Rydberg atom actually prevents the excitation of other nearby atoms in an ultracold sample [10–14]. This phenomenon was recently observed in microtraps [15, 16] and a C-NOT gate was implemented using this behavior [17]. A comprehensive review of the major works of the past decade in quantum information with regard to Rydberg atoms was recently published in [18].

Another interesting area of research involving atomic Rydberg interactions is the formation of long-range "exotic molecules." In one scenario, one atom remains in its ground state while a second atom is excited to a Rydberg state. The most famous examples of this type of interaction are the *trilobite* and *butterfly* states, so-called because of the resemblence of their respective wave functions to these creatures. The theoretical framework for such interactions was first proposed in [19], but evidence of their existence was not observed until more recently in [20].

The second type of interaction occurs when both atoms are excited to Rydberg states and interact with each other *via* multiple long-range forces. It was originally proposed in [21] that two interacting rubidium (Rb) Rydberg atoms could form very extended bound molecular states, labeled *macrodimers.* Specifically, long-range potential curves for various symmetry states were calculated using perturbation theory; some of these curves illustrated shallow potential wells, capable of supporting a few bound levels. Although these specific macrodimers have not been detected to date, other proposals involving Stark-shifted cesium atoms [22] have led to an experimental signature [23]. This will be discussed further in Chapter 3.

Another signature of strong interactions between two Rydberg atoms is that of molecular resonance features in excitation spectra. Such resonances were first observed in rubidium atoms [24], but have been more recently observed in cesium atoms as well [25]. In the rubidium experiment, the excitation of $5s$ ground state atoms to high np Rydberg states ($n = 50 - 90$) yielded pronounced molecular resonances corresponding to the average energy of the $(n-1)d + ns$ state pair. According to dipole transition rules, such $s \rightarrow s'$ and $s \rightarrow d$ excitations should not be allowed. It turned out that describing these observed resonances with the standard perturbation theory model [26] was not sufficient, mainly because the interaction energies of the Rydberg atom pairs contributing to the resonances were many times (~ 20) greater than the region of energy for which perturbation theory was applicable. Therefore, to properly describe the observed resonances, a much more accurate description of the long-range interactions was needed.

A detailed theoretical treatment describing these molecular resonances was given in [27, 28], in which an interaction Hamiltonian matrix was directly diagonalized. To properly describe the resonance features, the Hamiltonian contained not only the long-range Rydberg-Rydberg interaction potential, but atomic fine structure as well. The spin-orbit coupling of each atom causes an extensive mixing of their respective electronic wave functions [29] and results in the fine structure splitting of asymptotic energy levels. This is properly described by the Hund's case (c) coupling scheme. The potential curves presented in these works illustrated avoided crossings and strong ℓ-mixing between different electronic states, making for an interesting interaction picture. Due to the mixing of the asymptotic states, molecular states other than the directly excited $70p + 70p$ states became accessible. Thus, ℓ-mixing explained how access to normally forbidden states could be achieved via such excitations.

1.3 This dissertation

The theoretical model explaining the molecular resonances underscored an important point regarding long-range Rydberg-Rydberg interactions: perturbation theory is not enough to accurately describe the physical situation. The potential energy curves that result from diagonalizing the interaction Hamiltonian reveal details of complicated interactions not seen in curves calculated using perturbation theory, including avoided crossings and as we will see, new potential wells. We thus propose that the macrodimers predicted in [21] have not yet been realized because the physical model describing the interactions is incomplete.

In this dissertation, we adopt the same calculational methods used in [27] and [28] to produce interaction curves for various molecular symmetries and excited asymptotes of different alkali elements. All of these calculated curves demonstrate strong ℓ-mixing between molecular electronic states, but only some of them lead to deep potential wells. The wells we calculate here differ from those in [21] in two main respects: Our wells are significantly deeper for equivalent n values, and are formed *via* the mixing of different electronic character due to permanent multi-pole moments, not *via* induced van der Waals interactions.

This dissertation represents a comprehensive study of the long-range Rydberg-Rydberg interactions leading to bound molecular states. As such, we focus on the potential curves correlated to large potential wells and find that such wells are evident in the cases of rubidium and cesium. In our discussion of these macrodimers, we analyze a variety of properties such as responsivity to small electric fields, stability and scaling relations. We also propose a possible formation mechanism based on photoassociation, and include numerical calculations of lineshapes for that model.

1.3.1 Overview

In Chapter 2, we review the basic principles of molecular group theory and how group theory is useful to us in constructing properly symmetrized asymptotic basis states. We discuss the long-range Rydberg-Rydberg interaction potential and derive an analytical expression for the matrix elements. Finally, we discuss the potential curves that result from the diagonalization of the interaction matrix and provide examples of these curves.

In Chapter 3, we describe in detail several properties of the macrodimers. We begin by discussing the effect of a small electric field and show that the wells we focus on are stable with respect to such fields. We then calculate the energy levels and radial wave functions for the bound levels inside each potential well. We examine the effects of the ℓ-mixing by analyzing the eigenvectors of the potential curves. The electronic character of the wells will be important when describing formation properties in Chapter 4. We derive simple n-scaling relations for the dissociation energy and the equilibrium separation and conclude by showing that the bound excited states we predict are stable with respect to predissociation.

In Chapter 4, we review photoassociation and present a two-photon formation scheme to realize our marodimers. We derive the photoassociation rate expression for this two-photon process based on dipole transitions from two ground state atoms to two Rydberg state atoms. Finally, we provide calculated line shapes based on a collection of ground state atoms initially confined to a harmonic trap for two different electronic levels.

Finally, in Chapter 5, we provide an outlook of future work toward the extension of the two-body physics to a three-body system. We assume three identical Rydberg atoms along a common axis and calculate potential energy surfaces describing their interactions. We derive properly symmetrized asymptotic three-atom basis states and (assuming long-range conditions) use multiple two-body potentials to define the three-body interaction. We provide multiple surface plots illustrating various features for different basis states and discuss the relevance of these features.

Chapter 2

Molecular Potentials

Ultracold Rydberg atoms provide a very interesting avenue of study: translationally, the atoms are very slow, yet at the same time they have very high internal energies. For short experimental times, it has been shown [30, 31] that the translational motion of Rydberg atoms can be completely ignored and the sample can be treated as a "frozen Rydberg gas." Ignoring the translational dynamics of the atomic cores significantly simplifies the calculations of the interaction energies. Thus, the potential curves that we calculate in this chapter represent the internal energy of the Rydberg atoms as defined by their electronic energies.

In this chapter, we present potential energy curves associated with the long-range interactions of two identical ultracold Rydberg atoms. These curves are calculated by diagonalizing the interaction Hamiltonian in a basis set constructed in the Hund's case (c) coupling scheme. Hund's case (c) is appropriate when the spin-orbit coupling becomes significant and fine structure cannot be ignored, which is exactly the scenario we consider (see Chapter 1). This basis more accurately describes the molecular asymptotes at $R \to \infty$ and it more easily allows for a proper description of the ℓ-mixing at shorter R.

The strong coupling of the orbital $\vec{\ell}_\imath$ and spin $\vec{s}_\imath$ angular momenta of each electron $\imath$ (labeled 1 and 2) means that the only good quantum number in the Hund's case (c) basis is the projection Ω of the total angular momentum of the two-atom system $\vec{J} = \vec{\jmath}_1 + \vec{\jmath}_2$ along the internuclear axis (see Fig. 2.1). Here, $\vec{\jmath}_\imath = \vec{\ell}_\imath + \vec{s}_\imath$ is the total angular momentum of electron $\imath$. This means that the interaction Hamiltonian we consider will be diagonal in the basis of properly symmetrized $|n_1, \ell_1, \jmath_1, m_{\jmath_1}\rangle|n_2, \ell_2, \jmath_2, \Omega - m_{\jmath_1}\rangle$ states, where $n_\imath$ is the principal quantum number of electron $\imath$.

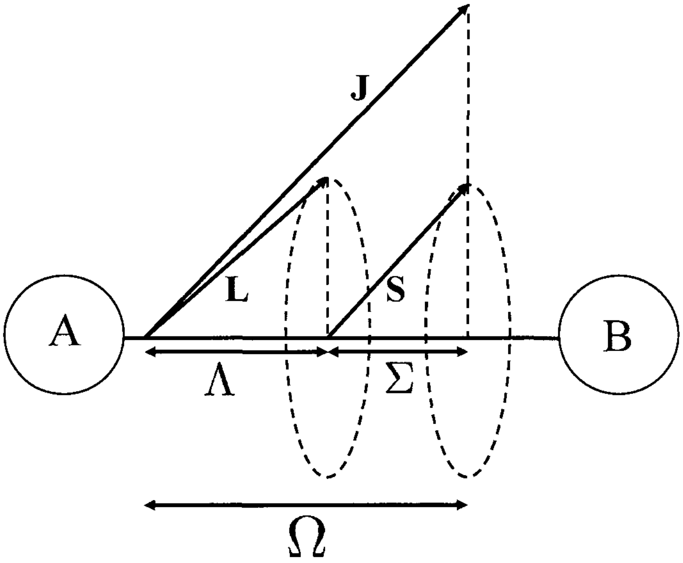

Fig. 2.1: Angular momenta of a diatomic molecule and their projections for both the coupled case (Hund's case (c)) and the uncoupled case (Hund's case (a)). Here, Λ is the projection of the total orbital angular momentum $\vec{L} = \vec{\ell}_1 + \vec{\ell}_2$, Σ is the projection of the total spin angular momentum $\vec{S} = \vec{s}_1 + \vec{s}_2$ and Ω is the projection of the total angular momentum $\vec{J} = \vec{\jmath}_1 + \vec{\jmath}_2$. We discuss the Hund's case (a) coupling scheme in Section 2.4.

In this chapter, we review the basics of molecular symmetries as applied to homonuclear dimers and show how this leads to properly symmetrized asymptotic basis states. We discuss the long-range interactions between two Rydberg atoms and derive an analytical expression for the matrix elements of the interaction Hamiltonians that we diagonalize. These diagonalizations lead to long-range potential energy curves. We present examples of such curves at the end of this chapter and include many more in Appendix A.

2.1 Molecular Symmetries and Symmetry Operations

Group theory has proven to be very useful in the study of molecules. Assigning molecules to groups based on their symmetry operations allows for considerable insight into their properties based solely on the properties of the individual symmetry group. For example, spatial symmetries of a molecule lead directly to energy and momentum conservation laws [32], which govern the dynamics of that molecule.

Molecules that possess the same spatial symmetries are classified according to their symmetry operations in what are called *point groups*, which is a symmetry group whose elements are the symmetry operations of molecules. Molecules in the same point group share the same symmetries and are therefore all invariant with respect to the same symmetry operations. The operators $\hat{O}$ that perform these symmetry operations leave the energy of the system unchanged, *i.e.* they commute with the Hamiltonian operator $\hat{H}$. This means that the set of eigenfunctions common to both $\hat{H}$ and $\hat{O}$ will form the basis for the matrix representation of the molecule's point group operations [29].

The homonuclear dimers discussed in this dissertation belong to the $D_{\infty h}$ point group, for which the relevant symmetry operations are rotations about the internuclear axis ($\hat{C}_n$), reflections through a plane containing the internuclear axis ($\hat{\sigma}_\nu$), and an inversion through the central spatial point of the two nuclei ($\hat{\imath}$) [29].

Given two identical atoms A and B, with respective electrons 1 and 2, the projection of the total electronic angular momentum $\Omega = m_{j_1} + m_{j_2}$ onto the internuclear axis is conserved as a consequence of the dimer's rotational symmetry [29, 32]. For $\Omega \neq 0$, a reflection through a plane containing the internuclear axis (see Figure 2.2) changes the direction of precession of the electron's angular momentum and thus changes the orientation of Ω [33]. Since the energy of this reflected state is the same as the original state, the two are degenerate. Consequently, symmetrizing the $\Omega \neq 0$ basis states with this reflection operator $\hat{\sigma}_\nu$ is redundant and unnecessary. For $\Omega = 0$, however, the (anti)symmetrization can give non-degenerate states and so this operation becomes mandatory when defining properly symmetrized basis states.

The inversion operator $\hat{\imath}$ acts to invert the electronic states of each electron relative to their respective atomic core and then exchange the two inverted electrons. The net result is that electron 1 is located around core B and electron 2 is located around core A (see Fig. 2.2). Since $\hat{\imath}^2 = 1$ (performing the inversion operator twice yields the original orientation), the eigenvalues p of $\hat{\imath}$ are $+1$ and -1. States that remain invariant under the inversion operator are known as *gerade* (g) states, while states that become negative under inversion are known as *ungerade* (u)

states.

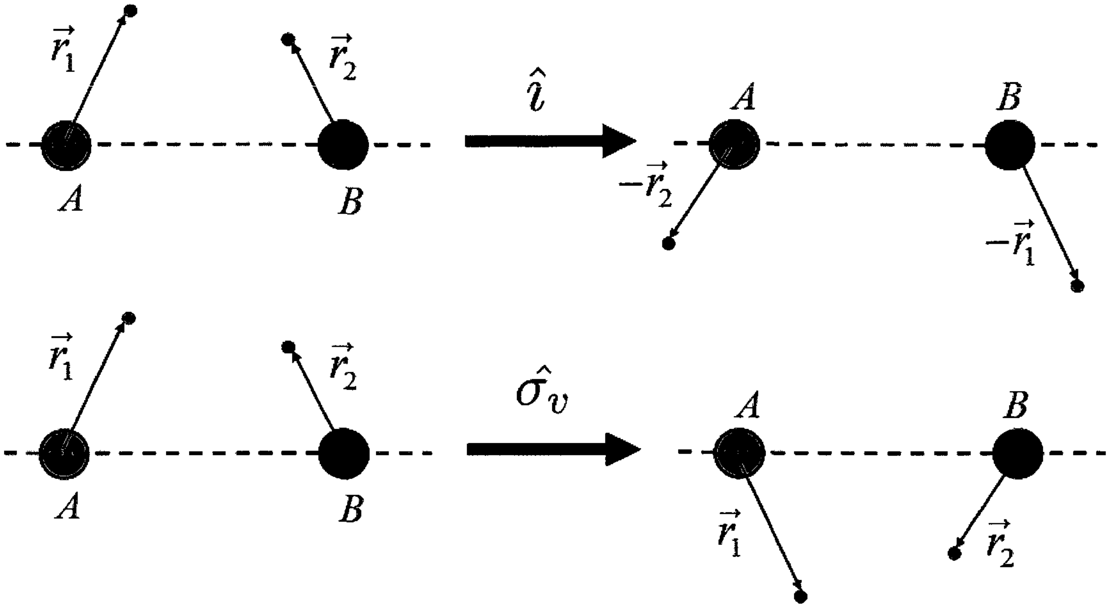

Fig. 2.2: Molecular symmetry operations for homonuclear dimers ($D_{\infty h}$ symmetry). The top panel illustrates an inversion of the electrons through a central point, while the bottom panel illustrates a reflection across a plane containing the internuclear axis.

2.2 The Basis

2.2.1 Basis States

As with any interaction picture, choosing an appropriate basis is crucial. The basis states must take into account the symmetries of the system, as well as the interactions of the physical problem. It has been shown [34] that the proper symmetrized Hund's case (c) basis states for $\Omega \neq 0$ take on the following form (we also review the derivation in Appendix B):

$$|a_1; a_2; \Omega_{g/u}\rangle = \frac{1}{\sqrt{2}} \left[|a_1\rangle|a_2\rangle - p(-1)^{\ell_1+\ell_2}|a_2\rangle|a_1\rangle\right] . \tag{2.2.1}$$

Here, $|a_1\rangle \equiv |n_1, \ell_1, j_1, m_{j1}\rangle$ and $|a_2\rangle \equiv |n_2, \ell_2, j_2, \Omega - m_{j1}\rangle$ are the states of two free Rydberg atoms described by the principle quantum number n_i, the orbital angular momentum quantum number ℓ_i, and the projection m_{j_i} of the total angular momentum $\vec{j_i} = \vec{\ell_i} + \vec{s_i}$ onto the internuclear axis (assumed to be in the z-direction). Ω is the total angular momentum projection as defined previously and p represents the eigenvalues of the inversion operator, also described previously.

For $\Omega = 0$, Equation (2.2.1) does not sufficiently define the basis states. Additionally, we need to account for the reflection symmetry through a plane containing the internuclear axis. Such a reflection will either leave the wave function unaffected or it will change the sign of the wave function. We distinguish between the symmetric and antisymmetric states under the $\hat{\sigma}_\nu$ operator via

$$|0^{\pm}_{g/u}\rangle = \frac{1 \pm \hat{\sigma}_\nu}{\sqrt{2}} |0_{g/u}\rangle \; , \tag{2.2.2}$$

where $\hat{\sigma}_\nu$ behaves according to the following rules [29, 35]:

$$\hat{\sigma}_\nu |\Lambda\rangle = (-1)^{\Lambda} | - \Lambda\rangle \, , \tag{2.2.3}$$

$$\hat{\sigma}_\nu |S, M_S\rangle = (-1)^{S - M_S} |S, -M_S\rangle \, . \tag{2.2.4}$$

When $\Lambda = 0$, Equation (2.2.3) does not properly describe the effect of $\hat{\sigma}_\nu$, which is to affect the orbital part of the electron wave function for the atomic states, *i.e.* $\hat{\sigma}_\nu |\ell, m_\ell\rangle = (-1)^{m_\ell} |\ell, -m_\ell\rangle$. Using these rules that describe the uncoupled case, we can formulate a convenient expression for the coupled case that we consider:

$$\hat{\sigma}_\nu|n,\ell,j,m_j\rangle|n',\ell',j',(\Omega-m_j)\rangle = \\ (-1)^{j+j'}|n,\ell,j,-m_j\rangle|n',\ell',j',(m_j-\Omega)\rangle \ . \tag{2.2.5}$$

2.2.2 Basis sets

To fully explore the ℓ-mixing, we build basis sets comprised of the properly symmetrized basis states discussed in Section 2.2.1. Of course, the physical parameters of the problem (such as the quantum state of the Rydberg atoms and the resulting Ω value) dictate which molecular states will be included in the basis set. In general, though, the basis sets consist of properly symmetrized states corresponding to those molecular asymptotes with significant coupling to both the molecular Rydberg level being considered and to other nearby asymptotes. Although dipolar coupling represents the strongest interaction between local asymptotes, quadrupolar coupling is significant for certain molecular levels and is thus taken into account when constructing the basis.

References [27] and [28] give the technical details for determining which asymptotic levels are used to build the basis states for the various symmetries in the case of $np + np$ rubidium. Although the procedure to find the basis states for different Rydberg molecular levels (such as $ns + ns$ and $nd + nd$) is the same, the relevant asymptotes upon which each basis set is constructed will be different. To gauge the relevance of nearby asymptotes, we compare their relative interaction strengths *via* the C_6 coefficient for dipole-dipole coupling:

$$C_6 \sim \frac{\langle\phi_1|r|\phi_2\rangle\langle\phi_3|r|\phi_4\rangle}{(E_1+E_3)-(E_2+E_4)} , \tag{2.2.6}$$

and the C_5 coefficient for quadrupole-quadrupole coupling:

$$C_5 \sim \langle\phi_1|r^2|\phi_2\rangle\langle\phi_3|r^2|\phi_4\rangle . \tag{2.2.7}$$

In these expressions, E_i is the asymptotic energy of atom i in state ϕ_i and $\langle\phi_i|r^k|\phi_j\rangle$ is the matrix element between atoms i and j. The fact that there are contributions from four atoms stems from the asymptotic nature of the two interacting molecular levels (two atomic states per molecular asymptote).

For Rydberg atoms, the energy E_i is given in atomic units by

$$E_i = -\frac{1}{2(n_i-\delta_{\ell_i})^2} , \tag{2.2.8}$$

where n_i is the principal quantum number and δ_{ℓ_i} represents a small corrective term known as the quantum defect. The quantum defect accounts for the fact that Rydberg electrons with small angular momenta have highly elliptical orbits that allow for penetration into the core. This exposes the electron to unshielded protons, increasing the electron's binding energy [2]. We calculate the quantum defect via [2]:

$$\delta_\ell = \delta_0 + \frac{\delta_2}{(n-\delta_0)^2} + \frac{\delta_4}{(n-\delta_0)^4} + \frac{\delta_6}{(n-\delta_0)^6} + \frac{\delta_8}{(n-\delta_0)^8} , \tag{2.2.9}$$

where the δ_i values are found experimentally and given in Table 2.1 for the alkali elements that we consider in this dissertation. We note that as the electron's angular momentum ℓ increases, the quantum defect decreases and for $\ell \geq 4$, the Rydberg atom is modeled as perfectly hydrogenic.

Using the relations given in Equations (2.2.6) and (2.2.7), we examine asymptotes within the vicinity ($\sim \pm 20$ GHz) of the molecular Rydberg level being considered and compare their relative interaction strengths. Again, we not only include the asymptotes that couple strongly to the molecular Rydberg level, we also include asymptotes that couple strongly to *these* levels. The matrix elements $\langle \phi_i | r^k | \phi_j \rangle$ are calculated using an inward-integrating Numerov method, as in [38] (see Appendix B for details). As shown in Table 2.2, we find that the dipole strength between two atomic states decays rapidly with the relative difference in their effective principal quantum numbers $\Delta n^* \equiv |n^* - n'^*|$, where $n^* \equiv n - \delta_\ell$ and $n'^* \equiv n' - \delta_{\ell'}$. We therefore only consider nearby asymptotic levels whose two constituent atoms have n_i^* values in the range $(n^* - 3) \leq n_i^* \leq (n^* + 3)$, where n^* is the effective principal quantum number of the Rydberg level being studied.

Once the relevant molecular asymptotes are determined from the above method, the properly symmetrized basis states are constructed from these asymptotes. We note that each molecular symmetry $\Omega^{\pm}_{g/u}$ results in a different set of basis states. As an example, Table 2.3 lists the basis set for the 0_g^+ symmetry near the Rb $70p + 70p$ molecular asymptote. For this $\Omega = 0$ symmetry, the basis states have been additionally symmetrized by the $\hat{\sigma}_\nu$ operator given in Equation (2.2.2). In this table, each $|a_1; a_2; 0_g\rangle$ state is defined by Equation (2.2.1).

Table 2.1: Quantum defects for the first five alkali elements All values are taken from [2], except for the δ_0 and δ_2 values of ^{85}Rb, which are taken from [36] and [37]

Series		δ_0	δ_2	δ_4	δ_6	δ_8
^{7}Li	$ns_{1/2}$	0 399468	0 030233	−0 0028	0 0115	
	$np_{1/2\ 3/2}$	0 47263	−0 02613	0 0221	−0 0683	
	$nd_{3/2\ 5/2}$	0 002129	−0 01491	0 01759	−0 8507	
	$nf_{5/2\ 7/2}$	0 0003055	−0 00126			
^{23}Na	$ns_{1/2}$	1 3479692	0 06137			
	$np_{1/2}$	0 855424	0 1222			
	$np_{3/2}$	0 854608	0 1220			
	$nd_{3/2\ 5/2}$	0 015543	−0 08535	0 7958	−4 0513	
	$nf_{5/2\ 7/2}$	0 001663	−0 0098			
^{39}K	$ns_{1/2}$	2 180197	0 136	0 0759	0 117	−0 206
	$np_{1/2}$	1 713892	0 2332	0 16137	0 5345	−0 234
	$np_{3/2}$	1 710848	0 2354	0 11551	1 105	−2 0356
	$nd_{3/2}$	0 276970	−1 0249	−0 709174	11 839	−26 689
	$nd_{5/2}$	0 277158	−1 0256	−0 59201	10 0053	−19 0244
	$nf_{5/2\ 7/2}$	0 010098	−0 100224	1 56334	−12 6851	
^{85}Rb	$ns_{1/2}$	3 1311804	0 1784	−1 8		
	$np_{1/2}$	2 6548849	0 2900	−7 904	116 437	−405 907
	$np_{3/2}$	2 6416737	0 2959	−0 97495	14 6001	−44 7265
	$nd_{3/2}$	1 34809171	−0 60286	−1 5017	−2 4206	19 736
	$nd_{5/2}$	1 34646572	−0 59600	−1 5017	−2 4206	19 736
	$nf_{5/2}$	0 0165192	−0 085	−0 36005	3 2390	
	$nf_{7/2}$	0 0165437	−0 086	−0 36005	3 2390	
^{133}Cs	$ns_{1/2}$	4 049325	0 246			
	$np_{1/2}$	3 591556	0 3714			
	$np_{3/2}$	3 559058	0 374			
	$nd_{3/2}$	2 475365	0 5554			
	$nd_{5/2}$	2 466210	0 0167			
	$nf_{5/2}$	0 033392	−0 191			
	$nf_{7/2}$	0 033537	−0 191			

Table 2.2: Dipole matrix elements for atomic transitions from Rb $70p_{3/2}$. We highlight the two largest elements and note the rapid decrease in coupling strength as $\Delta n^* = |n^* - n'^*|$ increases.

$\langle 70p_{3/2}\|r\|74s\rangle$	=	-162.74
$\langle 70p_{3/2}\|r\|73s\rangle$	=	286.53
$\langle 70p_{3/2}\|r\|72s\rangle$	=	-689.15
$\langle 70p_{3/2}\|r\|71s\rangle$	=	**4953.7**
$\langle 70p_{3/2}\|r\|70s\rangle$	=	**4082.5**
$\langle 70p_{3/2}\|r\|69s\rangle$	=	-690.75
$\langle 70p_{3/2}\|r\|68s\rangle$	=	243.06
$\langle 70p_{3/2}\|r\|67s\rangle$	=	-131.75
$\langle 70p_{3/2}\|r\|66s\rangle$	=	83.375

2.3 Long-range Interactions

In general, the interaction energy between two random charge distributions with centers A and B is calculated by summing over a bipolar expansion of the Coulombic potential [39, 40] between successive pairs of individual charges, *i.e.*

$$\begin{aligned} V &= \sum_{i,j} \frac{e_i e_j}{|\vec{r}_i - \vec{r}_j|} \\ &= \sum_{i,j} e_i e_j \sum_{\ell_A=0}^{\infty} \sum_{\ell_B=0}^{\infty} \sum_{m_\ell=-\ell_<}^{\ell_<} K_{\ell_A,\ell_B}^{m_\ell}(r_i, r_j; R)\, Y_{\ell_A}^{m_\ell}(\hat{R})\, Y_{\ell_B}^{-m_\ell}(\hat{u}_{ij}) \; . \end{aligned} \tag{2.3.1}$$

Here, $\vec{r}_k = r_k \hat{r}_k$ is the location of charge e_k, $\vec{R} = R\hat{R}$ is the vector connecting the origins of the two charge distributions, $\hat{u}_{ij}$ is the direction of the vector $\vec{u}_{ij} = \vec{r}_i - \vec{r}_j$, $K_{\ell_A,\ell_B}^{m_\ell}$ is a function determined by the physical orientation of the charge distributions, $\ell_{A(B)}$ represents the ℓ-th electric pole of charge distribution $A(B)$, and $\ell_<$ represents the smaller value of ℓ_A and ℓ_B.

The "long-range" scenario that we focus on in this dissertation refers to the case

Table 2.3: Asymptotic 0_g^+ molecular states included in the Rb $70p$+$70p$ basis set, which diagonalize the interaction Hamiltonian (see text). The basis states have been symmetrized with respect to the reflection operator (Eq. (2.2.2)) and each $\lvert a_1; a_2; 0_g\rangle$ state is defined by Equation (2.2.1).

$\frac{1}{\sqrt{2}}\left\{\lvert 70s\frac{1}{2},\frac{1}{2},71s\frac{1}{2},-\frac{1}{2},0_g\rangle - \lvert 70s\frac{1}{2},-\frac{1}{2},71s\frac{1}{2}\ \frac{1}{2},0_g\rangle\right\}$	$\frac{1}{\sqrt{2}}\left\{\lvert 68d\frac{3}{2},\frac{1}{2},71s\frac{1}{2},-\frac{1}{2},0_g\rangle + \lvert 68d\frac{3}{2},-\frac{1}{2},71s\frac{1}{2},\frac{1}{2}\ 0_g\rangle\right\}$
$\lvert 70p\frac{3}{2},\frac{3}{2},70p\frac{3}{2},-\frac{3}{2},0_g\rangle$	$\frac{1}{\sqrt{2}}\left\{\lvert 68d\frac{5}{2},\frac{1}{2},71s\frac{1}{2},-\frac{1}{2},0_g\rangle - \lvert 68d\frac{5}{2},-\frac{1}{2},71s\frac{1}{2},\frac{1}{2},0_g\rangle\right\}$
$\lvert 70p\frac{3}{2},\frac{1}{2},70p\frac{3}{2},-\frac{1}{2},0_g\rangle$	$\frac{1}{\sqrt{2}}\left\{\lvert 67d\frac{3}{2},\frac{1}{2},72s\frac{1}{2},-\frac{1}{2},0_g\rangle + \lvert 67d\frac{3}{2},-\frac{1}{2},72s\frac{1}{2},\frac{1}{2},0_g\rangle\right\}$
$\frac{1}{\sqrt{2}}\left\{\lvert 70p\frac{3}{2},\frac{1}{2},70p\frac{1}{2},-\frac{1}{2},0_g\rangle + \lvert 70p\frac{3}{2},-\frac{1}{2},70p\frac{1}{2},\frac{1}{2},0_g\rangle\right\}$	$\frac{1}{\sqrt{2}}\left\{\lvert 67d\frac{5}{2},\frac{1}{2},72s\frac{1}{2},-\frac{1}{2},0_g\rangle - \lvert 67d\frac{5}{2},-\frac{1}{2},72s\frac{1}{2},\frac{1}{2},0_g\rangle\right\}$
$\lvert 70p\frac{1}{2},\frac{1}{2},70p\frac{1}{2},-\frac{1}{2},0_g\rangle$	$\frac{1}{\sqrt{2}}\left\{\lvert 70d\frac{3}{2},\frac{1}{2},69s\frac{1}{2},-\frac{1}{2},0_g\rangle + \lvert 70d\frac{3}{2},-\frac{1}{2},69s\frac{1}{2},\frac{1}{2},0_g\rangle\right\}$
$\frac{1}{\sqrt{2}}\left\{\lvert 69p\frac{3}{2},\frac{3}{2},71p\frac{3}{2},-\frac{3}{2},0_g\rangle - \lvert 69p\frac{3}{2},-\frac{3}{2},71p\frac{3}{2},\frac{3}{2},0_g\rangle\right\}$	$\frac{1}{\sqrt{2}}\left\{\lvert 70d\frac{5}{2},\frac{1}{2},69s\frac{1}{2},-\frac{1}{2},0_g\rangle - \lvert 70d\frac{5}{2},-\frac{1}{2},69s\frac{1}{2},\frac{1}{2},0_g\rangle\right\}$
$\frac{1}{\sqrt{2}}\left\{\lvert 69p\frac{3}{2},\frac{1}{2},71p\frac{3}{2},-\frac{1}{2},0_g\rangle - \lvert 69p\frac{3}{2},-\frac{1}{2},71p\frac{3}{2},\frac{1}{2},0_g\rangle\right\}$	$\frac{1}{\sqrt{2}}\left\{\lvert 68s\frac{1}{2},\frac{1}{2},73s\frac{1}{2},-\frac{1}{2},0_g\rangle - \lvert 68s\frac{1}{2},-\frac{1}{2},73s\frac{1}{2},\frac{1}{2},0_g\rangle\right\}$
$\frac{1}{\sqrt{2}}\left\{\lvert 69p\frac{3}{2},\frac{1}{2},71p\frac{1}{2},-\frac{1}{2},0_g\rangle + \lvert 69p\frac{3}{2},-\frac{1}{2},71p\frac{1}{2},\frac{1}{2},0_g\rangle\right\}$	$\frac{1}{\sqrt{2}}\left\{\lvert 67f\frac{5}{2},\frac{1}{2},70p\frac{1}{2},-\frac{1}{2},0_g\rangle - \lvert 67f\frac{5}{2},-\frac{1}{2},70p\frac{1}{2},\frac{1}{2},0_g\rangle\right\}$
$\frac{1}{\sqrt{2}}\left\{\lvert 69p\frac{1}{2},\frac{1}{2},71p\frac{3}{2},-\frac{1}{2},0_g\rangle + \lvert 69p\frac{1}{2},-\frac{1}{2},71p\frac{3}{2},\frac{1}{2},0_g\rangle\right\}$	$\frac{1}{\sqrt{2}}\left\{\lvert 67f\frac{5}{2},\frac{1}{2},70p\frac{3}{2},-\frac{1}{2},0_g\rangle + \lvert 67f\frac{5}{2},-\frac{1}{2},70p\frac{3}{2},\frac{1}{2},0_g\rangle\right\}$
$\frac{1}{\sqrt{2}}\left\{\lvert 69p\frac{1}{2},\frac{1}{2},71p\frac{1}{2},-\frac{1}{2},0_g\rangle - \lvert 69p\frac{1}{2},-\frac{1}{2},71p\frac{1}{2},\frac{1}{2},0_g\rangle\right\}$	$\frac{1}{\sqrt{2}}\left\{\lvert 67f\frac{5}{2},\frac{3}{2},70p\frac{3}{2},-\frac{3}{2},0_g\rangle + \lvert 67f\frac{5}{2},-\frac{3}{2},70p\frac{3}{2},\frac{3}{2},0_g\rangle\right\}$
$\frac{1}{\sqrt{2}}\left\{\lvert 69s\frac{1}{2},\frac{1}{2},72s\frac{1}{2},-\frac{1}{2},0_g\rangle - \lvert 69s\frac{1}{2},-\frac{1}{2},72s\frac{1}{2},\frac{1}{2},0_g\rangle\right\}$	$\frac{1}{\sqrt{2}}\left\{\lvert 67f\frac{7}{2},\frac{1}{2},70p\frac{1}{2},-\frac{1}{2},0_g\rangle + \lvert 67f\frac{7}{2},-\frac{1}{2},70p\frac{1}{2},\frac{1}{2},0_g\rangle\right\}$
$\frac{1}{\sqrt{2}}\left\{\lvert 68p\frac{3}{2},\frac{3}{2},72p\frac{3}{2},-\frac{3}{2},0_g\rangle - \lvert 68p\frac{3}{2},-\frac{3}{2},72p\frac{3}{2},\frac{3}{2},0_g\rangle\right\}$	$\frac{1}{\sqrt{2}}\left\{\lvert 67f\frac{7}{2},\frac{1}{2},70p\frac{3}{2},-\frac{1}{2},0_g\rangle - \lvert 67f\frac{7}{2},-\frac{1}{2},70p\frac{3}{2},\frac{1}{2},0_g\rangle\right\}$
$\frac{1}{\sqrt{2}}\left\{\lvert 68p\frac{3}{2},\frac{1}{2},72p\frac{3}{2},-\frac{1}{2},0_g\rangle - \lvert 68p\frac{3}{2},-\frac{1}{2},72p\frac{3}{2},\frac{1}{2},0_g\rangle\right\}$	$\frac{1}{\sqrt{2}}\left\{\lvert 67f\frac{7}{2},\frac{3}{2},70p\frac{3}{2},-\frac{3}{2},0_g\rangle - \lvert 67f\frac{7}{2},-\frac{3}{2},70p\frac{3}{2},\frac{3}{2},0_g\rangle\right\}$
$\frac{1}{\sqrt{2}}\left\{\lvert 68p\frac{3}{2},\frac{1}{2},72p\frac{1}{2},-\frac{1}{2},0_g\rangle + \lvert 68p\frac{3}{2},-\frac{1}{2},72p\frac{1}{2},\frac{1}{2},0_g\rangle\right\}$	$\frac{1}{\sqrt{2}}\left\{\lvert 68f\frac{5}{2},\frac{1}{2},69p\frac{1}{2},-\frac{1}{2},0_g\rangle - \lvert 68f\frac{5}{2},-\frac{1}{2},69p\frac{1}{2},\frac{1}{2},0_g\rangle\right\}$
$\frac{1}{\sqrt{2}}\left\{\lvert 68p\frac{1}{2},\frac{1}{2},72p\frac{3}{2},-\frac{1}{2},0_g\rangle + \lvert 68p\frac{1}{2},-\frac{1}{2},72p\frac{3}{2},\frac{1}{2},0_g\rangle\right\}$	$\frac{1}{\sqrt{2}}\left\{\lvert 68f\frac{5}{2},\frac{1}{2},69p\frac{3}{2},-\frac{1}{2},0_g\rangle + \lvert 68f\frac{5}{2},-\frac{1}{2},69p\frac{3}{2},\frac{1}{2},0_g\rangle\right\}$
$\frac{1}{\sqrt{2}}\left\{\lvert 68p\frac{1}{2},\frac{1}{2},72p\frac{1}{2},-\frac{1}{2},0_g\rangle - \lvert 68p\frac{1}{2},-\frac{1}{2},72p\frac{1}{2},\frac{1}{2},0_g\rangle\right\}$	$\frac{1}{\sqrt{2}}\left\{\lvert 68f\frac{5}{2},\frac{3}{2},69p\frac{3}{2},-\frac{3}{2},0_g\rangle + \lvert 68f\frac{5}{2},-\frac{3}{2},69p\frac{3}{2},\frac{3}{2},0_g\rangle\right\}$
$\frac{1}{\sqrt{2}}\left\{\lvert 69d\frac{3}{2},\frac{1}{2},70s\frac{1}{2},-\frac{1}{2},0_g\rangle + \lvert 69d\frac{3}{2},-\frac{1}{2},70s\frac{1}{2},\frac{1}{2},0_g\rangle\right\}$	$\frac{1}{\sqrt{2}}\left\{\lvert 68f\frac{7}{2},\frac{1}{2},69p\frac{1}{2},-\frac{1}{2},0_g\rangle + \lvert 68f\frac{7}{2},-\frac{1}{2},69p\frac{1}{2},\frac{1}{2},0_g\rangle\right\}$
$\frac{1}{\sqrt{2}}\left\{\lvert 69d\frac{5}{2},\frac{1}{2},70s\frac{1}{2},-\frac{1}{2},0_g\rangle - \lvert 69d\frac{5}{2},-\frac{1}{2},70s\frac{1}{2},\frac{1}{2},0_g\rangle\right\}$	$\frac{1}{\sqrt{2}}\left\{\lvert 68f\frac{7}{2},\frac{1}{2},69p\frac{3}{2},-\frac{1}{2},0_g\rangle - \lvert 68f\frac{7}{2},-\frac{1}{2},69p\frac{3}{2},\frac{1}{2},0_g\rangle\right\}$
	$\frac{1}{\sqrt{2}}\left\{\lvert 68f\frac{7}{2},\frac{3}{2},69p\frac{3}{2},-\frac{3}{2},0_g\rangle - \lvert 68f\frac{7}{2},-\frac{3}{2},69p\frac{3}{2},\frac{3}{2},0_g\rangle\right\}$

where no electron exchange takes place between the atoms. This occurs when the distance between the two nuclei is greater than the LeRoy Radius [41]:

$$R_{LR} = 2\left[\langle n_1\ell_1|r^2|n_1\ell_1\rangle^{1/2} + \langle n_2\ell_2|r^2|n_2\ell_2\rangle^{1/2}\right] \ , \tag{2.3.2}$$

where $\langle n_\imath\ell_\imath|r^2|n_\imath\ell_\imath\rangle$ is the radial matrix element of r^2 belonging to valence electron $\imath$ of an alkali atom. When the nuclear distance between two atoms is larger than R_{LR}, their electron distributions do not overlap and the K function in Equation (2.3.1) is shown to be [42]:

$$K^{m_\ell}_{\ell_A,\ell_B} = (-1)^{\ell_B} \frac{4\pi}{R^{\ell_A+\ell_B+1}} \left(\frac{B^{\ell_A+m_\ell}_{\ell_A+\ell_B}\, B^{\ell_B+m_\ell}_{\ell_A+\ell_B}}{(2\ell_A+1)(2\ell_B+1)} \right)^{1/2} r_\imath^{\ell_A} r_\jmath^{\ell_B} , \tag{2.3.3}$$

where $B^k_n \equiv \frac{n!}{k!(n-k)!}$ is the binomial coefficient. In the case of two Rydberg atoms, we assume that the nucleus of each atom is located at A and B, respectively and we eliminate the sums over $\imath$ and $\jmath$ in Equation (2.3.1). Thus, we consider just the interactions of the two Rydberg electrons, labeled 1 and 2. If we further assume that the internuclear axis lies in the z-direction, *i.e.* $\vec{R} = R\hat{z}$, Equation (2.3.1) becomes:

$$V = \sum_{\ell_A=0}^{\infty} \sum_{\ell_B=0}^{\infty} \frac{4\pi}{R^{\ell_A+\ell_B+1}} \sum_{m_\ell=-\ell_A}^{\ell_A} (-1)^{\ell_B} \left(\frac{B^{\ell_A+m_\ell}_{\ell_A+\ell_B}\, B^{\ell_B+m_\ell}_{\ell_A+\ell_B}}{(2\ell_A+1)\,(2\ell_B+1)} \right)^{1/2}$$
$$\times\, r_1^{\ell_A} r_2^{\ell_B}\; Y^{m_\ell}_{\ell_A}(\hat{r}_1)\; Y^{-m_\ell}_{\ell_B}(\hat{r}_2) \; . \tag{2.3.4}$$

(Note: A full derivation of this expression is given in Appendix B). We examine the first few terms of Equation (2.3.4) and find that the dipole-dipole ($\ell_A = \ell_B = 1$) and quadrupole-quadrupole ($\ell_A = \ell_B = 2$) terms are the most dominant. Higher order terms ($\ell_{A(B)} \geq 3$) and "cross-terms" (*e.g.* $\ell_A = 1$, $\ell_B = 2$) are not significant and not included in our calculations. We thus define the Rydberg-Rydberg interaction energy as:

$$V_L(R) = \frac{(-1)^L 4\pi\; r_1^L r_2^L}{(2L+1)R^{2L+1}} \sum_m B^{L+m}_{2L} Y^m_L(\hat{r}_1) Y^{-m}_L(\hat{r}_2) \, , \tag{2.3.5}$$

where $L = 1(2)$ for dipole-dipole (quadrupole-quadrupole) interactions and the limits of m are $-L$ to L.

The Hund's case (c) basis sets we built in the previous section are used to diagonalize interaction Hamiltonians consisting of these long-range Rydberg interactions and atomic fine structure, i e

$$H(R) = V_L(R) + H_{fs} \tag{2 3 6}$$

Because the molecular basis states are linear combinations of the atomic states determined through symmetry considerations (see Eq (2 2 1)), each matrix element will actually be a sum of multiple interactions

$$\begin{aligned}\langle a, a', \Omega_{g/u}|V_L|b, b', \Omega_{g/u}\rangle &= \langle a, a'|V_L|b, b'\rangle - p_a(-1)^{\ell_a+\ell'_a}\langle a', a|V_L|b, b'\rangle \\ &\quad -p_b(-1)^{\ell_b+\ell'_b}\langle a, a'|V_L|b', b\rangle \\ &\quad +p_a p_b(-1)^{\ell_a+\ell'_a+\ell_b+\ell'_b}\langle a', a|V_L|b', b\rangle\ ,\end{aligned} \tag{2 3 7}$$

where $|a, a'\rangle \equiv |a\rangle_1|a'\rangle_2$ and so on An analytical expression for the long-range interactions is obtained using angular momentum algebra in terms of 3-j and 6-j symbols

$$\begin{aligned}\langle 1, 2|V_L(R)|3, 4\rangle &= (-1)^{L-1-\Omega+j_{\mathrm{tot}}}\sqrt{\hat{\ell}_1\hat{\ell}_2\hat{\ell}_3\hat{\ell}_4\hat{j}_1\hat{j}_2\hat{j}_3\hat{j}_4}\ \frac{\mathcal{R}_{13}^L\mathcal{R}_{24}^L}{R^{2L+1}} \\ &\times \begin{pmatrix} \ell_1 & L & \ell_3 \\ 0 & 0 & 0 \end{pmatrix}\begin{pmatrix} \ell_2 & L & \ell_4 \\ 0 & 0 & 0 \end{pmatrix}\begin{Bmatrix} j_1 & L & j_3 \\ \ell_3 & \frac{1}{2} & \ell_1 \end{Bmatrix}\begin{Bmatrix} j_2 & L & j_4 \\ \ell_4 & \frac{1}{2} & \ell_2 \end{Bmatrix} \\ &\times \sum_{m=-L}^{L} B_{2L}^{L+m}\begin{pmatrix} j_1 & L & j_3 \\ -m_{j_1} & m & m_{j_3} \end{pmatrix}\begin{pmatrix} j_2 & L & j_4 \\ -\Omega+m_{j_1} & -m & \Omega-m_{j_3} \end{pmatrix},\end{aligned} \tag{2 3 8}$$

where $\jmath_{\text{tot}} \equiv \sum_{\imath=1}^{4} \jmath_\imath$, $\hat{\ell}_\imath = 2\ell_\imath + 1, \hat{\jmath}_\imath = 2\jmath_\imath + 1$, and $\mathcal{R}^L_{\imath\jmath} = \langle \imath | r^L | \jmath \rangle$ is the radial matrix element calculated as before. This expression is derived in Appendix B.

The diagonal matrix elements are given by Equation (2.3.8) with $|1;2\rangle = |3;4\rangle$ plus the sum of the two Rydberg atoms' asymptotic energy values. That is:

$$\langle 1;2;\Omega_{g/u}|H(R)|1;2;\Omega_{g/u}\rangle = \langle 1;2;\Omega_{g/u}|V_L|1;2;\Omega_{g/u}\rangle + E_1 + E_2 \ , \qquad (2.3.9)$$

with $E_\imath$ given by Equation (2.2.8). Due to the Wigner symbols in Equation (2.3.8), $\Delta\ell = 0$ dipole transitions are forbidden and so only quadrupole-quadrupole interactions are present along the diagonal of the Hamiltonian.

Although we only consider long-range interactions here, the case where $R < R_{LR}$ could be analyzed by using the appropriate $K^{m_\ell}_{\ell_\imath,\ell_\jmath}$ coefficient (see [40]) to construct the proper "short-range" Rydberg potential. The interaction Hamiltonian describing this situation would also need to be diagonalized using a more general form of the basis states, *ı.e.* a form that does not assume non-overlapping charge distributions (see Appendix B).

2.4 Interaction Potentials and Symmetries

Equation (2.3.8) illustrates how the long-range interactions depend on the molecular symmetry Ω. Thus, each value of Ω will result in a different interaction matrix (Eq. (2.3.6)) and a new set of interaction potential curves. The value of Ω is of course determined by the quantum state of the Rydberg atoms. For example, two interacting $np_{3/2}$ atoms can yield Ω values of $0^{\pm}_{g/u}$, $1_{g/u}$, $2_{g/u}$, or $3_{g/u}$. However, only some of these symmetries lead to strongly attractive potentials. The relevance of the molecular symmetries is determined by whether or not the proposed symmetry allows for strong mixing between the asymptotic Rydberg level being considered and the other nearby molecular asymptotes. Since coupling strength does not depend on spin, we can temporarily neglect spin effects and examine the molecular symmetries in the Hund's case (a) notation. In the Hund's case (a) coupling scheme, the spin component of each electron's angular momentum is separable and can either be excluded from the analysis or added retroactively if needed [34]. The good quantum numbers in this scheme are the projection Λ of the total orbital angular momentum $\vec{L} = \vec{\ell}_1 + \vec{\ell}_2$ along the internuclear axis, the total spin angular momentum $\vec{S} = \vec{s}_1 + \vec{s}_2$, and its projection Σ along the internuclear axis (see Fig. 2.1).

When ignoring spin effects, Rydberg-Rydberg interactions do not mix states with different $\Lambda = m_{\ell_1} + m_{\ell_2}$, nor do they mix states with different eigenvalues of $\hat{\imath}$ and $\hat{\sigma}_\nu$ [34]. Therefore, only configurations of the *same symmetry* can be coupled together. This means that only common symmetries between the asymptotic Rydberg state and the molecular state to which it is most strongly coupled will be relevant. As an example, we consider the case of Rb $np + np$.

Using the relation defined in Equation (2.2.6), it can be shown that the rubidium $np + np$ asymptote couples the most strongly to $ns + (n + 1)s$. Upon comparing the molecular symmetries of these two states (see [26] or [43] for example), we note that the only common symmetry between $np + np$ and $ns + (n + 1)s$ is ${}^1\Sigma_g^+ - {}^3\Sigma_u^+$. The relevant molecular symmetries in the Hund's case (c) are then determined by adding in the effects of spin via $\Omega = |\Lambda + \Sigma|$, where Λ and Σ are as defined before. For a two-electron system, Σ can be -1, 0, or $+1$. Adding these to the common $\Lambda = 0$ symmetries described above yields $\Omega = 0_g^+$, 0_u^- and 1_u as the common molecular symmetries in the Hund's case (c) coupling scheme; thus, these are the only relevant symmetries. Although we only consider the $np + np$ case an an example here, we identify the significant symmetries for $ns + ns$ and $nd + nd$ in an identical manner. The results are given in Table 2.4. Of course, all of these symmetries have their own unique interaction matrices that must be diagonalized.

Table 2.4: Doubly excited ns, np, and nd Rydberg states, the nearby asymptotes to which each is most strongly coupled (see text) and the relevant molecular symmetries in both the Hund's case (a) and (c) coupling schemes.

Rydberg state	Coupling asymptote	Common symmetries (Hund's case (a))	Common symmetries (Hund's case (c))
$ns + ns$	$np + (n-1)p$	${}^1\Sigma_g^+ - {}^3\Sigma_u^+$	0_g^+, 0_u^-, 1_u
$np + np$	$ns + (n+1)s$	${}^1\Sigma_g^+ - {}^3\Sigma_u^+$	0_g^+, 0_u^-, 1_u
$nd + nd$	$(n+1)p + (n-1)f$	${}^1\Sigma_g^+ - {}^3\Sigma_u^+$ ${}^3\Sigma_g^- - {}^1\Sigma_u^-$ ${}^3\Pi_g - {}^1\Pi_u$ ${}^1\Pi_g - {}^3\Pi_u$ ${}^3\Delta_g - {}^1\Delta_u$ ${}^1\Delta_g - {}^3\Delta_u$ ${}^3\Phi_g - {}^1\Phi_u$ ${}^1\Phi_g - {}^3\Phi_u$ ${}^1\Gamma_g - {}^3\Gamma_u$	0_g^+, 0_u^-, $1_{g/u}$, $2_{g/u}$, $3_{g/u}$, $4_{g/u}$, 5_u

The numerical diagonalization of the interaction matrix defined by Equation (2.3.6) was carried out using the Jacobi algorithm given in [44], which relies on a successive sequence of similarity transformations (plane rotations) to remove the off-diagonal matrix elements. The algorithm diagonalizes the input matrix (to machine precision) and yields an array of eigenvalues and a matrix of their associated eigenvectors. Although this diagonalization scheme is slower than other routines, it preserves the original input order of the basis states and does not numerically sort the eigenenergies/eigenvectors during the diagonalization process. This allows us to more easily extract important information about the curves, such as which electronic states most strongly contribute to the creation of the potential wells (see Section 3.2).

The procedures outlined in this chapter were applied to doubly excited[1] ns, np and nd Rydberg atoms for all *relevant* symmetries of the first five alkali elements. At shorter range, the significant amount of avoided crossings due to the ℓ-mixing results in potential curves that are very complex. In Figure 2.3, we show the 0_u^- symmetry curves resulting from the interactions between $ns + ns$ (top row), $np+np$ (middle row), and $nd+nd$ (bottom row) Rydberg atoms for the first three alkali elements (lithium, sodium, and potassium). Larger versions of these curves are also shown in Appendix A. These curves exemplify the complex nature of the interaction systems that we study, and analyzing them can help explain physical behaviors of the systems. For example, molecular resonances observed in [24] were explained by the mixing of a set of rubidium curves [27, 28].

---

[1] Throughout the dissertation we use the term "doubly excited" to describe the scenario where both atoms are excited to the same Rydberg state and not the scenario where one atom has been excited twice.

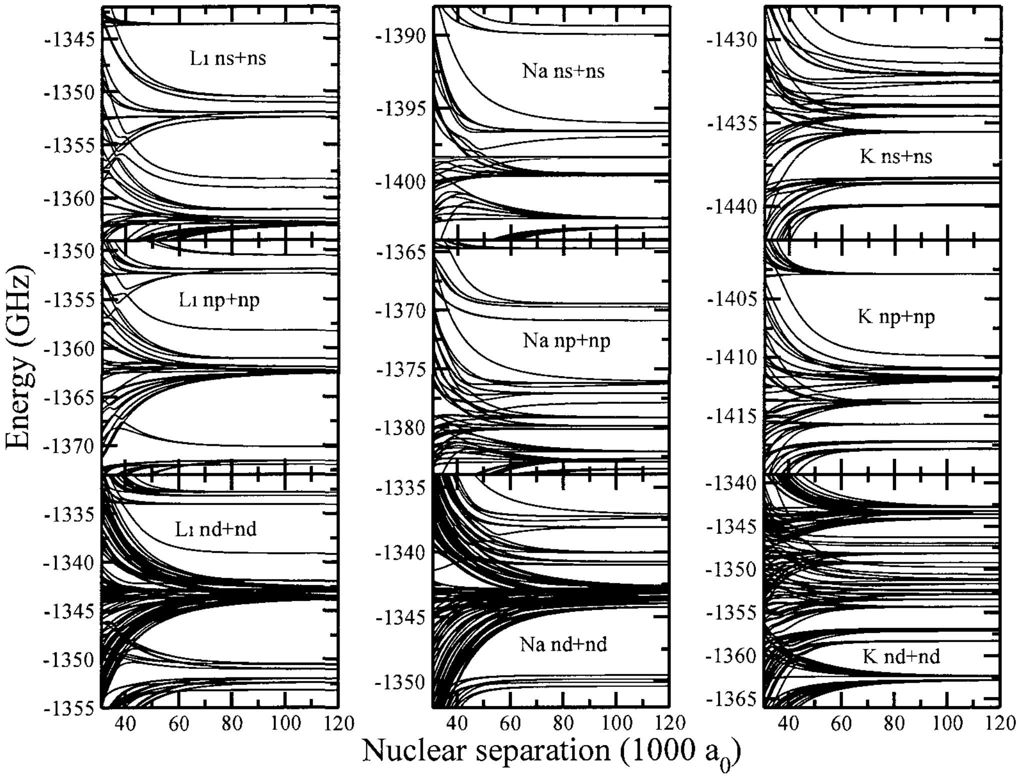

Fig. 2.3: Long-range interaction curves for the 0_u^- symmetry of doubly excited *ns* (top row), *np* (middle row) and *nd* (bottom row) Rydberg atoms for lithium (left), sodium (middle), and potassium (right). We point out the complex nature of the curves resulting from the ℓ-mixing (see text).

In this dissertation, however, we choose to focus our attention on interaction curves that exhibit deep potential wells, capable of supporting bound vibrational states. After analyzing all of the interaction curves that we calculated, we find that deep ($\sim 1-2$ GHz) potential wells exist for doubly excited *ns* and *np* rubidium atoms (see Fig. 2.4) and doubly excited *np* cesium atoms (see Fig. 2.5). In Appendix A, we display the remainder of our calculated potential curves that do not exhibit such deep wells. We note that in the case of doubly excited *nd* states,

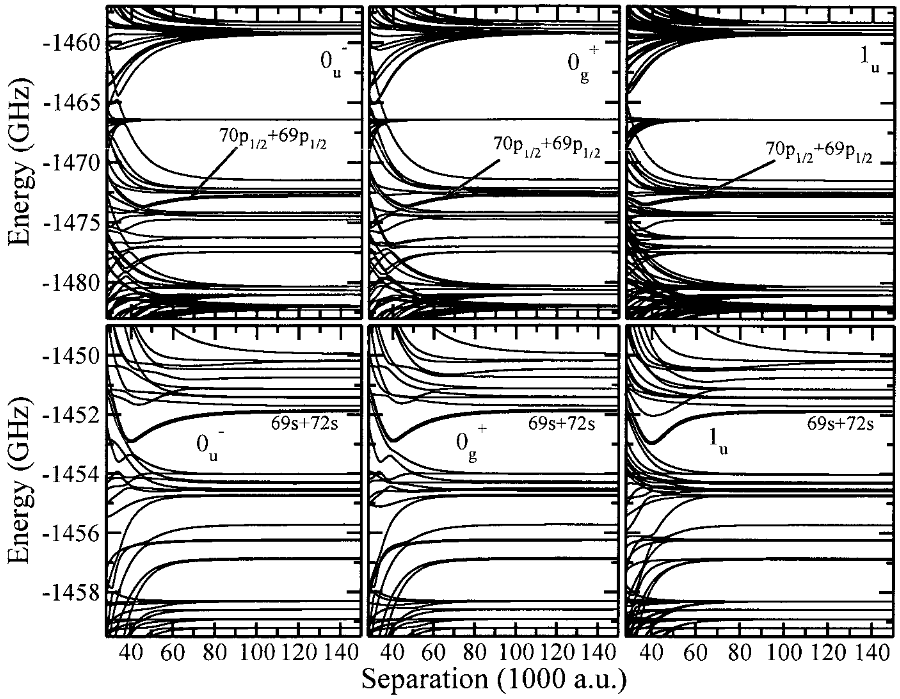

Fig. 2.4: Long-range interaction curves for the 0_u^- (left), 0_g^+ (middle) and 1_u (right) symmetries of doubly excited *ns* (top row) and *np* (bottom row) Rb Rydberg atoms near $n = 70$. We highlight each potential well and label its corresponding asymptotic level.

the relevant asymptotes comprising the basis sets include states with larger angular momenta values, *i.e.* f and g states. These higher angular momenta quickly lead to significantly more asymptotically degenerate states, which seem to prohibit the formation of deep potential wells in these $nd + nd$ curves.

2.5 Conclusions

In this chapter, we have presented the theoretical framework from which we calculate long-range molecular potentials for various symmetries of doubly excited Rydberg states of different alkali elements. We calculate these wells by directly diagonalizing interaction Hamiltonians in the Hund's case (c) basis. We use prop-

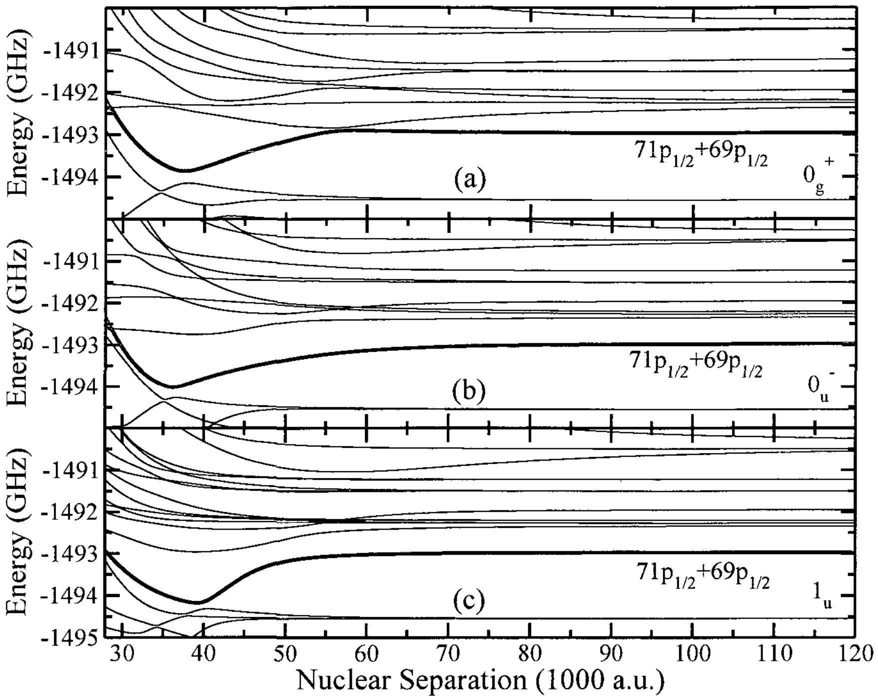

Fig. 2.5: Long-range interaction curves for the 0_g^+ (a), 0_u^- (b), and 1_u (c) symmetries of doubly excited *np* Cs Rydberg atoms near $n = 70$. We highlight each potential well and label its corresponding asymptotic level.

erly symmetrized asymptotic basis states derived from molecular group theory, and a Rydberg-Rydberg interaction energy derived from a long-range Coulombic expansion. This yields a convenient analytical result for homonuclear dimers. We have found that of the five alkali elements we studied, only potential curves associated with rubidium and cesium feature large potential wells. Such potential wells are important because they indicate extended molecular states, which we study in detail in the subsequent chapters.

It is important to point out that the procedure given in this chapter is only valid in the long-range case, *i.e.* when the distance R between the two atomic nuclei is greater than the Le-Roy radius R_{LR}, although we have outlined how to investigate interactions at distances shorter than this value. We also note that this method assumes the Born-Oppenheimer approximation, which ignores the motion of the two nuclei. Since the motion of the electrons is much faster than that of the heavy nuclei, the two cores are treated as stationary with respect to the valence electrons and to each other. Due to the particularly large masses of rubidium and cesium, any contributions from their respective nuclei should be negligible to our interaction picture.

Chapter 3

Macrodimers

In this chapter, we study features found in potential energy surfaces. For example, Figures 2.4 and 2.5 highlighted at the end of chapter 2 are intriguing to us because the exhibited wells are deep enough ($\sim$ 1 GHz) to support many bound vibrational states. As we will show, the equilibrium positions of these bound states are extremely large, on the order of $1-2$ μm. Hence, we use the term *macrodimers* to describe them. This size of molecular dimer could facilitate research in a wide variety of areas, provided they exist for a long enough period of time.

Of other interest to us is how the macrodimers would respond to an electric field. Any experiment that is performed to produce and/or detect these macrodimers will require equipment that produces electric fields. Since even the best experimental techniques cannot completely shield the atoms from undesired fields, it is important to predict ahead of time how the theoretical curves calculated in Chapter 2 will be affected by such fields. Our motivation here is strictly to ensure that small, stray electric fields do not inhibit the formation of the macrodimers before we commit ourselves to a detailed exploration of other bound state properties. We note that the work we do here with the electric field is in contrast to the work done in [22] and [23], which relied on an applied electric field to physically create the potential wells they were to study. In our treatment, the electric field is considered a perturbative effect to the pre-existing potential wells.

In this chapter, we first show that the macrodimers we predict are indeed stable with respect to a small applied electric field. We then go on to examine and explore several properties of the bound states, including their energies, equilibrium separations, scaling relations, and lifetimes.

3.1 Electric Fields

Strictly speaking, applying an external electric field $\vec{F}$ breaks the $D_{\infty h}$ symmetry of homonuclear dimers and consequently, the basis states defined by Eq. (2.2.1) are no longer valid. In principle, one then needs to diagonalize the interaction matrix in a basis set containing every possible Stark state, as was done in [22]. However, since the effects of an electric field should be adiabatic, we assume that the $D_{\infty h}$ symmetry is still approximately valid for small electric fields, and apply the framework discussed in Chapter 2.

Due to the large size of Rydberg atoms and their high sensitivity to electric fields, we can use a semi-classical model for our discussion. In this section, we adopt methods taken from [38] and describe in detail how we obtain the molecular Stark states. By diagonalizing the new interaction matrix in the Stark basis, we produce potential curves similar to those in Chapter 2. The theoretical framework we present here is applicable to any two identical interacting Rydberg atoms, but our results detail the interactions between two $70p$ rubidium Rydberg atoms.

In the semi-classical treatment, the electric field's energy is considered a perturbation to the original Hamiltonian. For Rydberg atoms, this perturbation lifts the energy degeneracy of eigenstates corresponding to the same n and ℓ values and separates the energy levels. The shifted energies correspond to the eigenvalues of the perturbed Hamiltonian matrix, which are calculated by diagonalizing the matrix in a new set of basis states called Stark states.

In general, the applied electric field defines a quantization axis in the lab-fixed frame (LF), while the quantum states of the macrodimers are defined in the body-fixed frame (BF). One then needs to project Ω onto the field axis, typically via Wigner-D rotation matrices, *i.e.*

$$\Psi(\vec{r}_1, \vec{r}_2) = \sum_{m'_{j1}=-j1}^{j1} \sum_{m'_{j2}=-j2}^{j2} D^{j1}_{m'_{j1},m_{j1}}(\hat{r'}_1)\, D^{j2}_{m'_{j2},m_{j2}}(\hat{r'}_2)\, \Psi(\vec{r'}_1, \vec{r'}_2) \ , \qquad (3.1.1)$$

where primed variables indicate the lab-fixed frame, unprimed variables indicate the body-fixed frame, $\hat{r'}_i \equiv (\theta'_i, \varphi'_i)$ are the rotated angular coordinates of the wave function $\Psi(\vec{r}_1, \vec{r}_2)$ (defined in ket form by Equation (2.2.1)), and $D^k_{p,q}(\hat{r})$ are the Wigner-D functions. Details of performing such rotations are given in [45–48]. Since such mathematical exercises are not particularly instructive to the physical problem we wish to study, we do not explicitly carry out the rotations here. Rather, we simplify the calculations by assuming that the two Rydberg atoms are first confined in an optical lattice, such that the quantization axes of the macrodimer and the electric field align. This could be accomplished by trapping the Rydberg atoms wthin different sites of the lattice and aligning the electric field parallel to the lattice (see Figure 3.1). Such one-dimensional optical lattices have already been used to experimentally excite Rydberg atoms from small Bose-Einstein condensates located at individual sites [49]. We envision a similar scheme, with the distance between adjacent (or subsequent) sites adjusted to coincide with the equilibrium length R_e, while containing only a single atom per site. The optical lattice could be switched off during the Rydberg excitation to allow a cleaner signal.

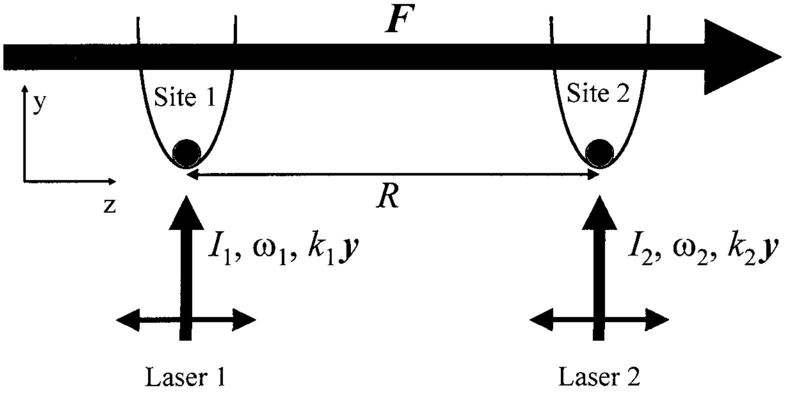

Fig. 3.1: Two Rydberg atoms confined within a harmonic optical lattice. The electric field $\vec{F}$ is directed along the z-axis, coinciding with the molecular axis of the dimer. We also indicate in this cartoon that the two excitation lasers (see Chapter 4) propagate in the y-direction, but the polarization directions of both lasers are along the z-axis.

For an electric field directed along the z-axis, the perturbation Hamiltonian is given by $Fr\cos\theta$, where F is the magnitude of the field, r is the distance of the valence electron from its nucleus and θ is the angle between F and r. The eigenvalue equation is of course written as:

$$\hat{H}|\Psi\rangle = E|\Psi\rangle \ , \tag{3.1.2}$$

where $\hat{H}$ is the perturbed Hamiltonian, E is the corresponding perturbative energy and $|\Psi\rangle = \sum_a c_a|a\rangle$, with $|a\rangle \equiv |n_a\ell_a m_{\ell_a}\rangle$ being the atomic basis states that diagonalize the unperturbed Hamiltonian. For convenience, we write Eq. (3.1.2) in matrix form:

$$\mathsf{H_{ba}c_a} = \mathsf{Ec_b} \, , \tag{3.1.3}$$

where

$$\begin{aligned}\mathsf{H_{ba}} &= \langle b|Fr\cos\theta|a\rangle \\ &= \langle b|Fr\sqrt{\frac{4\pi}{3}}Y_1^0(\theta,\phi)|a\rangle \\ &= F\sqrt{\frac{4\pi}{3}}\langle n_b\ell_b|r|n_a\ell_a\rangle\langle \ell_b m_{\ell_b}|Y_1^0(\theta,\phi)|\ell_a m_{\ell_a}\rangle \ .\end{aligned} \tag{3.1.4}$$

Here, the dipole matrix element $\langle n_b\ell_b|r|n_a\ell_a\rangle$ is calculated as in Chapter 2 and the angular matrix element $\langle \ell_b m_{\ell_b}|Y_1^0(\theta,\phi)|\ell_a m_{\ell_a}\rangle$ is carried out using basic Spherical Harmonic algebra.

Multiplying both sides of Equation (3.1.3) from the left by a rotation matrix R^{-1} and inserting the identity matrix $\mathsf{I} = \mathsf{RR}^{-1}$, we can write:

$$\mathsf{R^{-1}H_{ba}(RR^{-1})c_a} = \mathsf{ER^{-1}c_b} \, . \tag{3.1.5}$$

From Equation (3.1.5), we make the following observations:

1. A rotation matrix R that is composed of the eigenvectors of H_{ba} will diagonalize H_{ba},

2. The eigenvalues resulting from diagonalization will be the Stark-shifted energies of the atomic states, and

3. The eigenstates of the diagonalized Stark Hamiltonian (Stark states) will be a series expansion of the "undressed" states:

$$|\tilde{a}\rangle_k = \sum_{\imath} b_{k,\imath}(F)|a_\imath\rangle_k, \tag{3.1.6}$$

where $|a_\imath\rangle_k \equiv |n_\imath, \ell_\imath, \jmath_\imath, m_\jmath^{(\imath)}\rangle_k$ are the undressed atomic states and $b_{\imath,k}(F)$ are the field-dependent eigenvectors of atom k. For the small field values that we consider, each Stark state $|\tilde{a}\rangle_k$ can be expressed as $|\tilde{a}\rangle_k = b_{k,1}(F)|a_1\rangle_k + \sum_{\imath=2} b_{k,\imath}(F)|a_\imath\rangle_k$, where $b_{k,1}(F) \sim (1 - c_1 F)$ and $b_{k,\imath}(F) \sim c_\imath F$, with each c coefficient being very small. The summation index $\imath$ runs over the quantum numbers $n_\imath$, $\ell_\imath$, and $\jmath_\imath$. Although the limits of this summation are technically $n_\imath \to n_{\max}$ (where $n_{\max}$ is the highest n value in the basis) and $\ell_\imath \to (n_\imath - 1)$, we restrict the summation to $(n-2) < n_\imath < (n+2)$ and $\ell_\imath \leq 3$; the $b_\imath(F)$ coefficients are insignificant (three to four orders of magnitude smaller) for states lying outside these bounds (see Figure 3.2).

We diagonalize the Stark Hamiltonian for varying F and calculate the Stark-shifted energies and the Stark states as was done in [38]. Figure 3.3 shows an example of a "Stark map," which illustrates how the asymptotic energies of Rydberg atoms vary with an applied electric field. In particular, this plot shows a

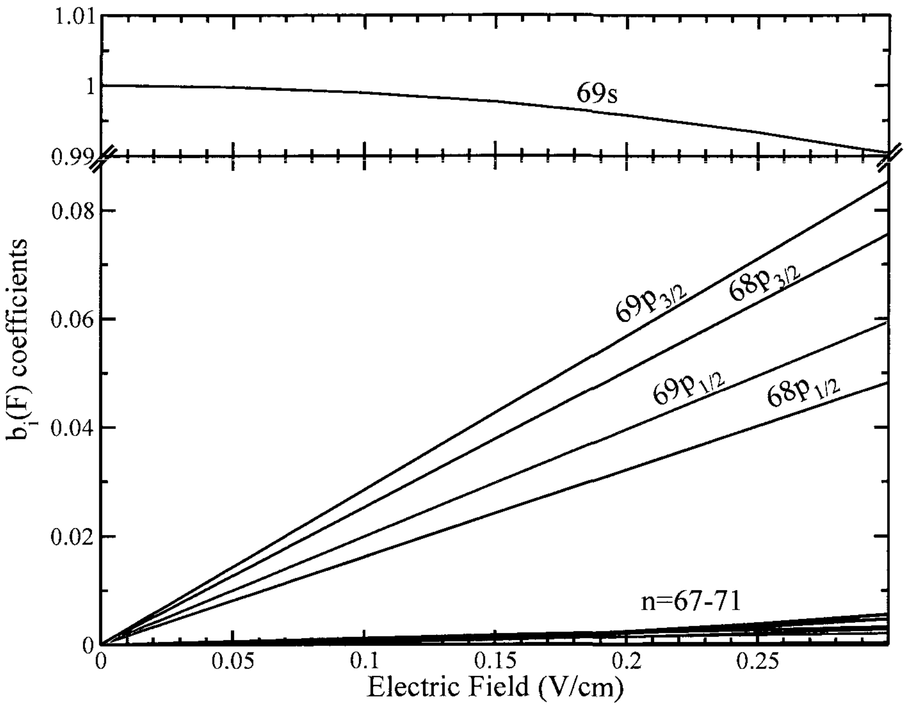

Fig. 3.2: Eigenvector coefficients for the $69s$ Stark state. In this range of electric field values, the $|\widetilde{69s}\rangle$ Stark state is mostly composed of the undressed $|69s\rangle$ atomic state shown in the top panel. The bottom panel shows the next highest contributing undressed states in the Stark state expansion (see Equation (3.1.6)). The collection of states labeled 67-71 include the remaining s, p, d and f states for these n values not highlighted in the figure.

collection of states for $|m_\ell| = 0$ rubidium near the $n = 69$ manifold.

In Figure 3.2, we plot some of the eigenvector coefficients $b_{k,i}(F)$ against the electric field F for the $|\widetilde{69s}\rangle$ Stark state. As would be expected for a small electric field, $|\widetilde{69s}\rangle$ is composed mainly of the undressed $|69s\rangle$ state, although other states do contribute as well. We use Fig. 3.2 to illustrate two major points: (1) our argument for truncating the summation in Equation (3.1.6) is justified and (2) by comparing this figure with Figure 3.3, it is clear that the electric field has a

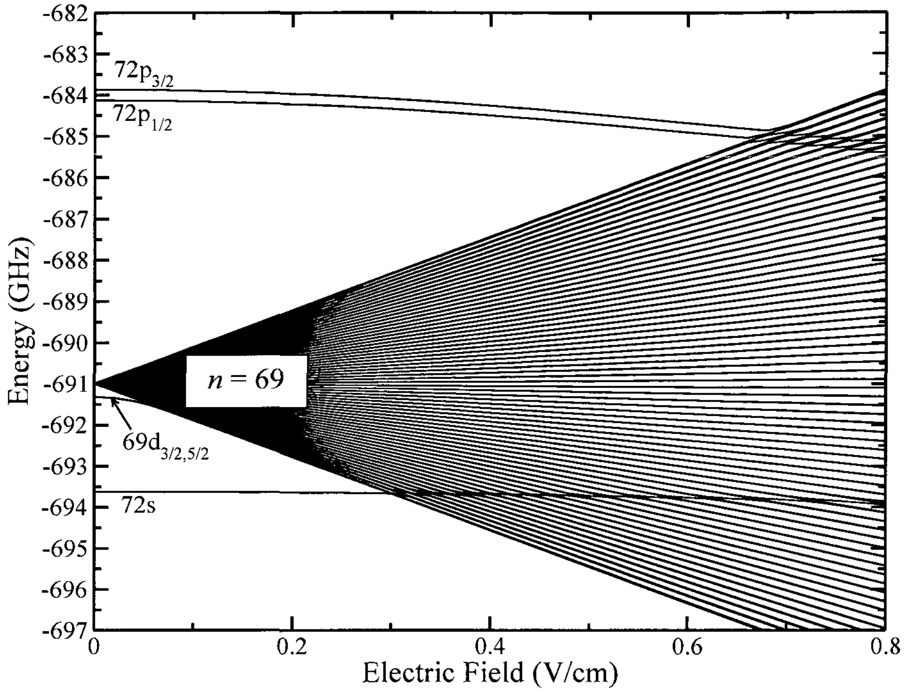

Fig. 3.3: Atomic Rydberg energies vs. the electric field for Rb with $|m_\ell| = 0$ near the $n = 69$ manifold: the curves labeled as $n = 69$ include all states with $\ell \geq 3$.

much more noticable effect on the asymptotic energies than it does on the Stark states. Thus, for future considerations, diagonalizing a Hamiltonian containing the Stark-shifted energies in the *undressed* basis should be sufficient for small electric fields.

We replace the atomic states defined in Eq. (2.2.1) with the dressed states in Eq. (3.1.6) and define the dressed molecular basis states as:

$$|\tilde{a}\rangle_1 |\tilde{a}\rangle_2 = \sum_{ij} b_{1,i}(F) b_{2,j}(F) |a_i\rangle_1 |a_j\rangle_2 \,. \tag{3.1.7}$$

We then use this definition to express the properly symmetrized dressed molecular basis, given in Table 2.3 and to diagonalize the Rydberg-Rydberg interaction matrix. In Fig. 3.4, we illustrate the effect of $\vec{F}$ on the curves near $70p + 70p$ of the 0_g^+ symmetry for rubidium in a side-by-side comparison of the curves for (a) $F = 0$ and (b) $F = 0.3$ V/cm. This value of F is chosen so that the ns states are still mostly ns with only small amounts of higher ℓ-values (see Fig. 3.3), *i.e.* below the "crossing" of the $72s$ state with the higher ℓ states. We note that the Stark effect is most notable in the shifting of the potential curves, especially the asymptotic energies. However, the relative shapes of the curves are mostly unchanged and most importantly, the large potential well we wish to focus on is robust against small electric fields. Since the effects of the electric field are relatively small, our discussion will proceed assuming zero-field conditions.

3.2 Bound States

We describe the wave function of a bound level v inside a given potential well λ by the tensor product:

$$|\Psi_v^{(\lambda)}(R)\rangle = |\phi_v(R)\rangle \otimes |\chi_\lambda(R)\rangle \ , \tag{3.2.1}$$

where $|\phi_v(R)\rangle$ is the radial portion of the bound level v and $|\chi_\lambda(R)\rangle$ is the electronic quantum state associated with the potential curve λ.

We calculate the radial wave functions $|\phi_v(R)\rangle$ using the mapped Fourier Grid Method, developed in [50]. In Figure 3.5, we show an example of such a wave function for the $v = 500$ eigenstate of the well corresponding to the 0_g^+ symmetry

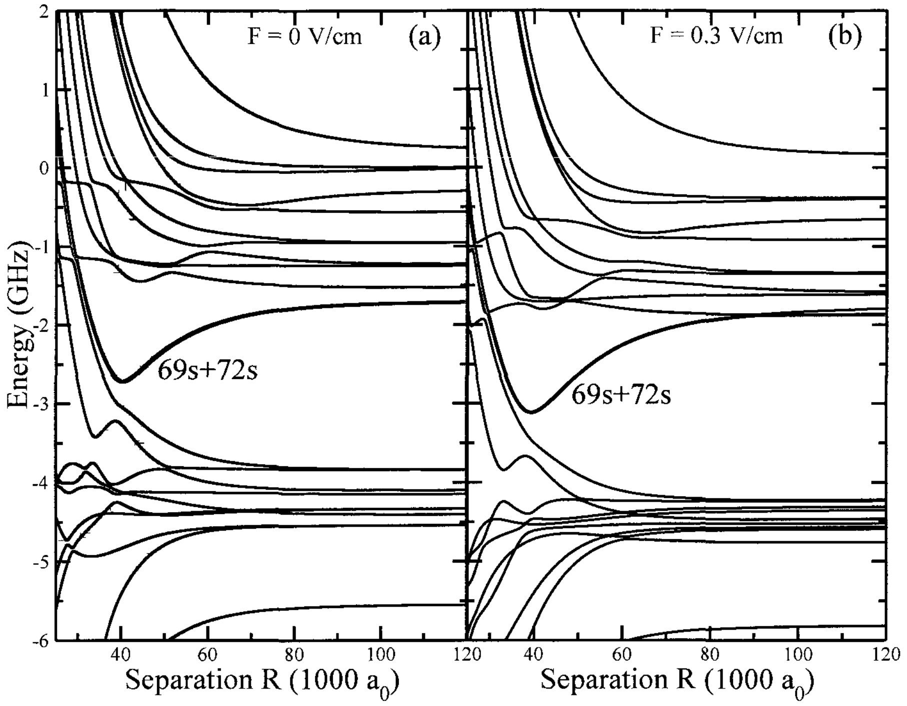

Fig. 3.4: 0_g^+ molecular curves for Rb $70p + 70p$: (a) $F = 0$, and (b) $F = 0.3$ V/cm. We highlight the large potential well correlated to the $69s + 72s$ asymptotic curve and zero the energy scale at the unperturbed $70p_{3/2} + 70p_{3/2}$ asymptote. We acknowledge the significant shifting of the asymptotic levels due to the Stark effect (see text), but note that the well remains relatively unaffected by the applied electric field.

of Rb $70p + 70p$. The figure is not to scale, but we note the oscillatory nature of the wave function inside the well: this behavior will be important later in our photoassociation discussion (see Chapter 4).

Using the mapped Fourier Grid Method, we also calculate the energy levels of all bound states within the wells. In Tables 3.1 and 3.2, we list the first few vibrational levels bound within the potential wells highlighted in Figures 2.4 and 2.5. We also illustrate the first few bound levels for the Rb $70p + 70p$ well (0_g^+ symmetry) in the inset of Figure 3.5. The MHz energy levels correspond to oscillation

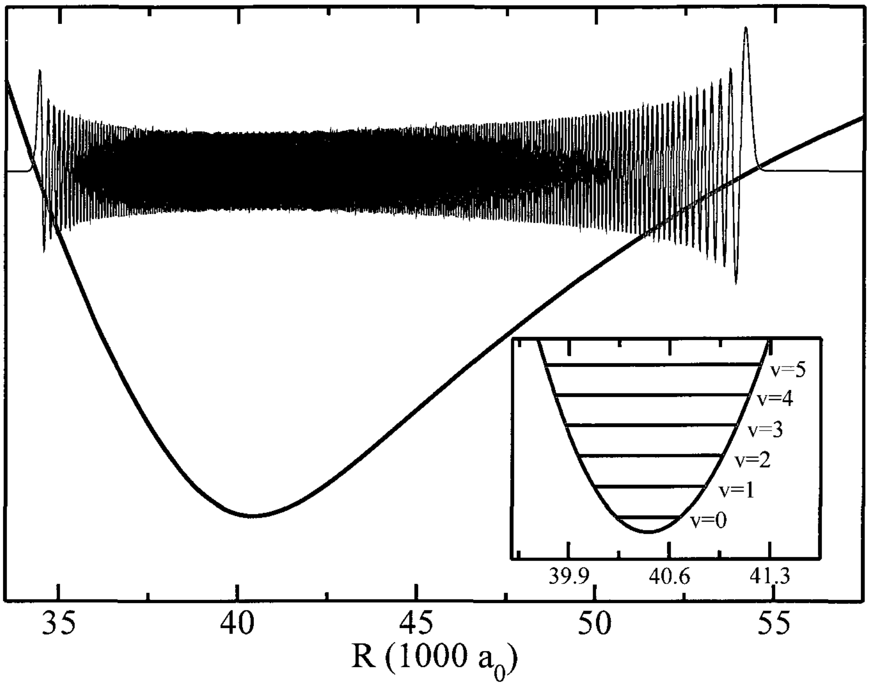

Fig. 3.5: Radial wave function for the $v = 500$ bound state in the Rb $70p + 70p$ 0_g^+ potential well (not to scale). We note the sinusoidal behavior inside the well. Inset: Energy levels for the first six bound states.

periods between 1 and 10 μs, which are rapid enough to be detected during the lifetime of these Rydberg atoms (roughly a few hundred μs for $n = 70$ at ultracold temperatures) [51]. We also note that since the energy levels are separated by about 1.5 MHz, they should provide favorable resolution in spectroscopy experiments. Tables 3.1 and 3.2 also list the classical turning points of each level, confirming that these are very extended bound states.

As mentioned throughout this dissertation, the potential wells that we predict

Table 3.1: Energies of the six deepest bound levels (measured from the bottom of the well) and corresponding classical turning points for the 0_g^+, 0_u^- and 1_u symmetries near doubly excited $70s$ and $70p$ Rb Rydberg atoms

Asymptote	Symmetry	v	Energy (MHz)	R_1 (a u)	R_2 (a u)
$70s + 70s$	0_g^+	0	1 035	46,137	46,538
		1	3 122	45,985	46,688
		2	5 353	45,870	46,800
		3	7 478	45,780	46,888
		4	9 567	45,702	46,963
		5	11 645	45,630	47,032
$70s + 70s$	0_u^-	0	1 034	45,072	45,488
		1	3 161	44,913	45,650
		2	5 263	44,803	45,761
		3	7 332	44,716	45,854
		4	9 369	44,639	45,934
		5	11 392	44,569	46,008
$70s + 70s$	1_u	0	0 918	36,181	36,600
		1	2 699	36,038	36,755
		2	4 468	35,938	36,868
		3	6 241	35,859	36,963
		4	7 988	35,789	37,046
		5	9 748	35,730	37,121
$70p + 70p$	0_g^+	0	0 831	40,228	40,679
		1	2 499	40,068	40,849
		2	4 167	39,959	40,970
		3	5 825	39,870	41,068
		4	7 477	39,795	41,154
		5	9 125	39,728	41,233
$70p + 70p$	0_u^-	0	0 801	39,753	40,212
		1	2 415	39,590	40,381
		2	4 023	39,479	40,509
		3	5 632	38,390	40,610
		4	7 235	39,312	40,699
		5	8 833	39,244	40,778
$70p + 70p$	1_u	0	0 709	36,907	37,361
		1	2 212	36,752	37,535
		2	3 722	36,632	37,635
		3	5 220	36,545	37,780
		4	6 735	36,467	37,870
		5	8 239	36,399	37,954

Table 3.2: Energies of the six deepest bound levels (measured from the bottom of the well) and corresponding classical turning points for the 0_g^+, 0_u^- and 1_u symmetries near doubly excited 70*p* Cs Rydberg atoms.

Asymptote	Symmetry	v	Energy (MHz)	R_1 (a.u.)	R_2 (a.u.)
$70p + 70p$	0_g^+	0	0.819	37,457	37,821
		1	2.458	37,326	37,956
		2	4.092	37,236	38,052
		3	5.720	37,162	38,197
		4	7.344	37,099	38,197
		5	8.961	37,042	38,257
$70p + 70p$	0_u^-	0	0.948	36,110	36,451
		1	2.838	35,987	36,577
		2	4.717	35,901	36,665
		3	6.591	35,833	36,739
		4	8.458	35,773	36,802
		5	10.315	35,720	36,859
$70p + 70p$	1_u	0	0.900	39,062	39,408
		1	2.667	38,920	39,526
		2	4.422	38,819	39,604
		3	6.164	38,733	39,667
		4	7.882	38,659	39,720
		5	9.608	38,591	39,768

are a direct result of the ℓ-mixing that occurs between the electronic states. This means that each electronic $|\chi_\lambda(R)\rangle$ state is actually a composition of every electronic molecular state in the basis set (see Section 2.2). The exact amount of mixing varies with R and is given by an expansion of the asymptotic basis states:

$$|\chi_\lambda(R)\rangle = \sum_j c_j^{(\lambda)}(R)|j\rangle \ , \tag{3.2.2}$$

where $c_j^{(\lambda)}(R)$ are the eigenvectors after diagonalization and $|j\rangle \equiv |a_j; a'_j\rangle$ are the asymptotic electronic molecular basis states defined in Eq. (2.2.1). In general, j spans the entire basis set, but we can truncate the sum on a case-by-case basis, keeping only the states that significantly contribute to the formation of the potential wells. As an example, we consider the large potential wells highlighted in the 0_g^+ symmetry curves for Rb $70p + 70p$ and Rb $70s + 70s$ shown in Figure 2.4. In Figure 3.6(a), we replot these two sets of curves near the respective wells and highlight the asymptotic states that contribute the most to each well. In part (b) of the plots, we show the corresponding probabilities $|c_j(R)|^2$ of the highlighted states against the nuclear separation R.

As we would expect from Fig. 3.6(a), Figure 3.6(b) illustrates that the right sides of each well (near the $69s + 72s$ asymptote for $70p + 70p$ and the $70p_{1/2} + 69p_{1/2}$ asymptote for $70s + 70s$) are composed mostly of the $|69s72s\rangle$ and $|70p_{1/2}69p_{1/2}\rangle$ states, respectively. In the $70p + 70p$ case, this trend continues smoothly towards the $|c_{j=69s72s}|^2 = 1$ asymptote. However, in the $70s+70s$ plot, we note that there is some abrupt "spiking" behavior in the curves around $R \sim 78\ 000\ a_0$, corresponding to the avoided crossing between the $|70p_{1/2}69p_{1/2}\rangle$ state and the $|70p_{3/2}69p_{1/2}\rangle$

state above it We point out that as the $|70p_{1/2}69p_{1/2}\rangle$ contribution decreases in this region, the largest increasing contribution is from the $|69s71s\rangle$ state and *not* the $|70p_{3/2}69p_{1/2}\rangle$ state, as could be expected for an "avoided crossing" This illustrates that the crossing is not simply due to quadrupole interactions as would normally be the case between two pp' molecular states, but rather via a complicated dipole-mixing of the ℓ-states

From the shapes of the curves in Fig 3 6(a), we would expect the left side of each well to be mostly composed of a state whose asymptote is below that of the wells, *i e* $|68p72p\rangle$ ($|68p71p\rangle$) for $np+np$ ($ns+ns$) However, we note for the left sides of both wells that the contributing states all correspond to asymptotes that lie *above* each well In the case of $70p+70p$, the $69s+72s$ molecular level couples strongly to both the $69p+71p$ states (above) and the $68p+72p$ states (below) However, the relative energy differences between the asymptotes results in a much stronger interaction between $69s+72s$ and the $69p+71p$ states than with the $68p+72p$ states This is why there is little contribution from the $68p+72p$ states in the formation of the well In the case of $ns+ns$, the states directly below the well correlated to the $69p_{1/2}+71p_{1/2}$ asymptote are $68p+71p$ states In general, the strength of the quadrupole coupling between np states and $n'p$ states is very weak Combining this with the large spacing between the asymptotic energy levels results in minimal contributions from the $68p+71p$ states in the formation of the well

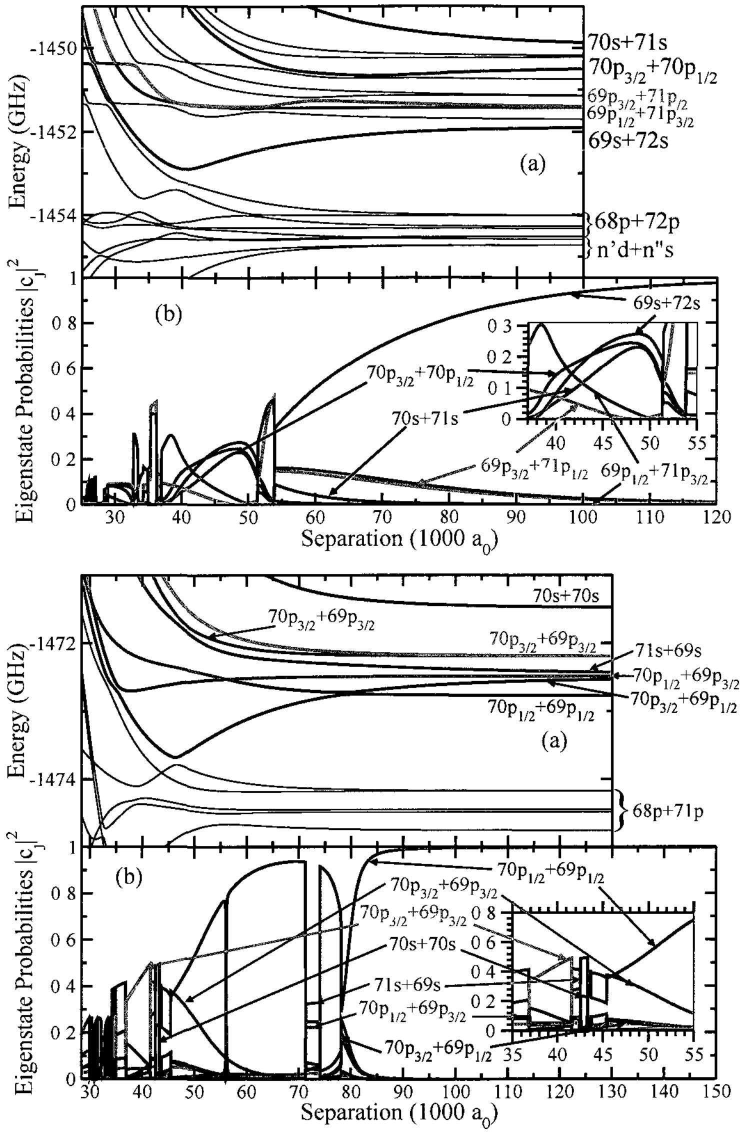

Fig. 3.6: (a) 0_g^+ symmetry curves of the rubidium $70p + 70p$ molecular asymptote localized near the $70p_{3/2}+70p_{3/2}$ asymptote (top panel), and of the $70s + 70s$ molecular asymptote localized near the $70s + 70s$ asymptote (bottom panel). For both panels, we highlight the molecular curves corresponding to the electronic states contributing the most to the formation of the well (see text). (b) Composition of the $69s$+$72s$ well (top panel) and of the $69p_{1/2} + 70p_{1/2}$ well (bottom panel): probabilities $|c_j(R)|^2$ of the electronic states that contribute the most to the formation of the well vs. the nuclear distance R. Inset: zoom of the inner region near the minimum of the potential well.

3.3 Scaling

For asymptotic coupling that is dominantly dipolar in nature, the interactions between the electronic states depend on the spacing between each state's asymptotic energy level and the strength of the dipole-dipole coupling between the asymptotes (see Equation (2.2.6)). Although our calculations include both dipole-dipole and quadrupole-quadrupole interaction terms, the dipolar term dominates the interaction picture and thus we assume pure dipole coupling in this discussion. To derive a simple n-scaling behavior for both the well depth D_e and the equilibrium separation R_e, we also assume that the potential wells are formed as the result of an avoided crossing between two curves (see Figure 3.7(a)). Although the real situation is much more complex, these assumptions allow for a simple treatment.

The energy difference $\Delta E_{\alpha\beta} = E_\alpha - E_\beta$ is defined by the difference between the asymptotes of the two crossing states α and β. Here, $\alpha = n_{\alpha_1}\ell_1 + n_{\alpha_2}\ell_2$ and $\beta = n_{\beta_1}\ell'_1 + n_{\beta_2}\ell'_2$, with energies (in a.u.)

$$E_\alpha = -\frac{1}{2}\left(\frac{1}{(n_{\alpha_1} - \delta_{\ell_1})^2} + \frac{1}{(n_{\alpha_2} - \delta_{\ell_2})^2}\right) \tag{3.3.1a}$$

and

$$E_\beta = -\frac{1}{2}\left(\frac{1}{(n_{\beta_1} - \delta_{\ell'_1})^2} + \frac{1}{(n_{\beta_2} - \delta_{\ell'_2})^2}\right) , \tag{3.3.1b}$$

respectively. To derive a simple n-scaling relation, it will be convenient to describe the principal quantum number of each asymptotic atomic state n_{γ_i} in terms of the principal quantum number n of the doubly-excited Rydberg state; *i.e.* $n_{\gamma_i} = n \pm \Delta n_{\gamma_i}$. For example, the $69s + 72s$ asymptote corresponding to the potential well for the Rb $70p + 70p$ asymptote can be written as $(n-1)s + (n+2)s$,

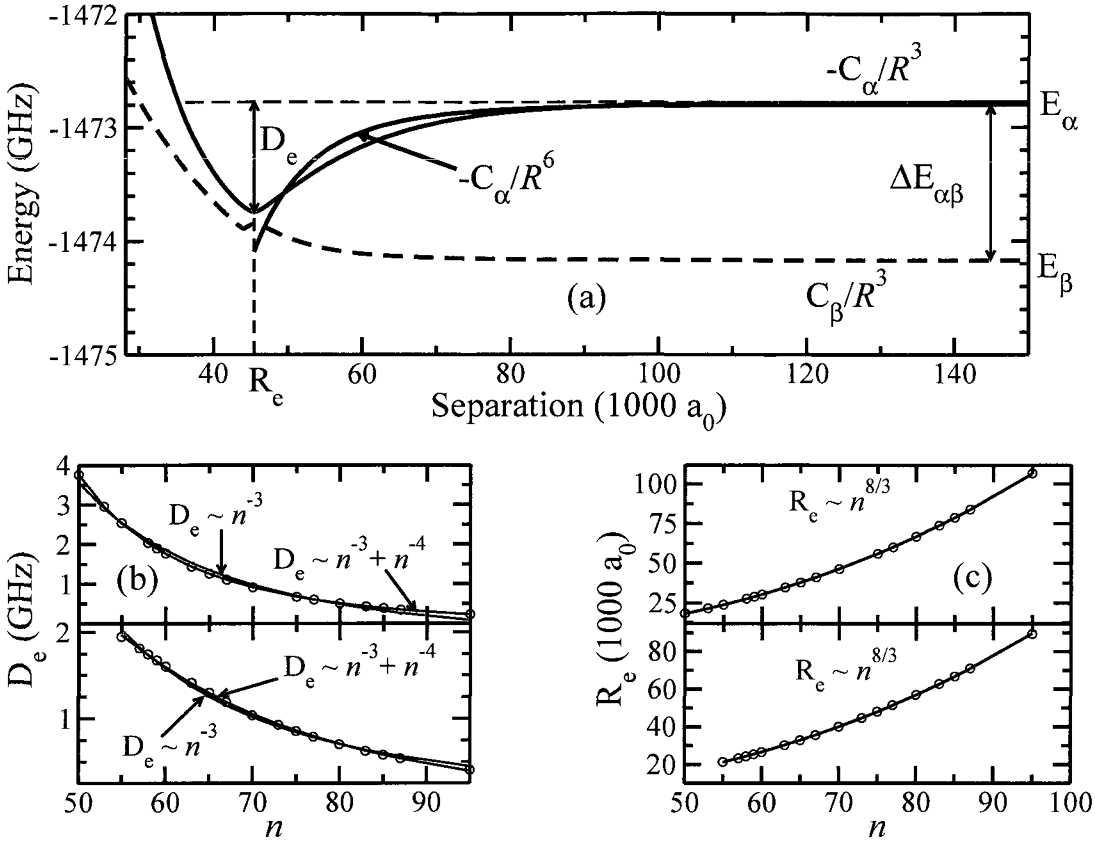

Fig. 3.7: (a) Isolated avoided crossing in the 0_u^- symmetry curves of double excited $70s$ rubidium atoms, which result in the potential well correlated to the $69p_{1/2} + 70p_{1/2}$ asymptote. We assume the interactions at the crossing are mostly dipolar in nature (see text) and label the depth D_e and the equilibrium separation R_e at the "avoided crossing". We also demonstrate that at long-range the curves behave as $\sim 1/R^6$, but in the R-range of the well, the $1/R^3$ description is appropriate. (b) Scaling relations for the well depth D_e vs n for the 0_u^- symmetry of $ns+ns$ (top) and $np+np$ (bottom) rubidium. (c) Scaling relations for the equilibrium separation R_e vs n for the same curves as in (b).

where $n = 70$. When we additionally account for the quantum defects, we find that each n_{γ_i} can be expressed as $n_{\gamma_i} = n - \Delta_{\gamma_i}$, where Δ_{γ_i} contains the differences in the principal quantum numbers and the quantum defects.

The energy difference between the asymptotes of the crossing states is then given by:

$$\Delta E_{\alpha\beta} = -\frac{1}{2}\left[\frac{1}{(n-\Delta_{\beta_1})^2} + \frac{1}{(n-\Delta_{\beta_2})^2} - \frac{1}{(n-\Delta_{\alpha_1})^2} - \frac{1}{(n-\Delta_{\alpha_2})^2}\right] , \quad (3.3.2)$$

where we then factor out the common n from each energy term:

$$\Delta E_{\alpha\beta} = -\frac{1}{2n^2}\left[\left(1-\frac{\Delta_{\beta_1}}{n}\right)^{-2} + \left(1-\frac{\Delta_{\beta_2}}{n}\right)^{-2} - \left(1-\frac{\Delta_{\alpha_1}}{n}\right)^{-2} - \left(1-\frac{\Delta_{\alpha_2}}{n}\right)^{-2}\right] . \quad (3.3.3)$$

Since all Δ_{γ_i} are of order unity and thus $n \gg \Delta_{\gamma_i}$, we Taylor expand each term in Equation (3.3.3) as:

$$\left(1-\frac{\Delta_{\gamma_i}}{n}\right)^{-2} = 1 + 2\,\frac{\Delta_{\gamma_i}}{n} - 6\left(\frac{\Delta_{\gamma_i}}{n}\right)^2 , \quad (3.3.4)$$

and express $\Delta E_{\alpha\beta}$ as:

$$\Delta E_{\alpha\beta} = -\frac{\Delta_{\beta_1} + \Delta_{\beta_2} - \Delta_{\alpha_1} - \Delta_{\alpha_2}}{n^3} + 3\,\frac{\Delta_{\alpha_1}^2 + \Delta_{\alpha_2}^2 - \Delta_{\beta_1}^2 - \Delta_{\beta_2}^2}{n^4} . \quad (3.3.5)$$

In the cases leading to our wells, we find that $\Delta_{\alpha_1} + \Delta_{\alpha_2} \simeq \Delta_{\beta_1} + \Delta_{\beta_2}$, so that the leading dependence in Eq. (3.3.5) is $\Delta E_{\alpha\beta} \propto n^{-4}$. We point out that this is in contrast to the normal n-scaling law for Rydberg atoms: expanding to the n^{-3} term is sufficient for atomic Rydbergs [2].

From the sketch depicted in Fig. 3.7(a), assuming leading dipole-dipole interactions, the equilibrium separation R_e occurs at the "intersection" of two curves: one attractive and one repulsive, separated by $\Delta E_{\alpha\beta}$, *i.e.* $-C_\alpha/R_e^3 \sim \Delta E_{\alpha\beta} - C_\beta/R_e^3$. Rearranging this expression gives $R_e \sim \{(C_\beta - C_\alpha)/\Delta E_{\alpha\beta}\}^{1/3}$, where $(C_\beta - C_\alpha)$ scales as n^4 [2] and $\Delta E_{\alpha\beta}$ scales as n^{-4} from above; this yields $R_e \sim n^{8/3}$. Our assumption that the two crossing curves behave as $\sim 1/R^3$ is valid in the region of the intersection; at larger values of R, however ($R \gtrsim 80\ 000\ a_0$), the curves behave more like $\sim 1/R^6$ (see Figure 3.7(a)). We also see from this figure that the dissociation energy D_e is given simply by $D_e \simeq \Delta E_{\alpha\beta} - C_\alpha/R_e^3$, where $\Delta E_{\alpha\beta}$ and C_α/R_e^3 both scale as n^{-4}. Therefore, we conclude that $D_e \propto n^{-4}$.

Figure 3.7(b) shows a plot of D_e vs n for the 0_u^- symmetry of the ns+ns and np+np asymptotes for rubidium and indicates that D_e indeed scales more like $\sim n^{-3}+n^{-4}$ (blue curve) than purely n^{-3} (red curve). For the same wells, Fig. 3.7(c) shows that R_e follows the predicted $n^{8/3}$ scaling.

Although the analytical derivations give good agreements with numerically determined values of D_e and R_e, slight discrepencies reflect the more complex nature of the interactions. For example, quadrupole coupling is present in our calculations (although its effect is generally small). We also point out that in the three Rb $np + np$ cases, the formation of each well is not clearly given by an avoided crossing of two curves, but rather by three interacting curves. Nonetheless, the good agreement depicted in Figs. 3.7(b) and (c) for the Rb $np + np$ case indicates that these more complicated interactions act only as small corrections.

3.4 Lifetimes

In the previous section, we showed that assuming the potential wells are formed as a result of an avoided crossing between two curves yields accurate results; we therefore continue with this assumption in the following discussion. In general, avoided crossings can lead to predissociation of bound energy levels if the metastable state has strong coupling to a repulsive (unstable) state below it. The result of such predissociation would be two free Rydberg atoms with additional kinetic energy, which could heat the ultracold sample through collisions and ionization, an undesirable situation. In addition, experimental detection would be difficult or impossible if the predissociation rate is too rapid. However, as we demonstrated in Section 3.2, there is very little coupling between the wells that we calculate and the asymptotes that lie below them. Therefore, we should expect very small predissociation rates from the bound levels and consequently long-lived macrodimers.

For the potential wells that are clearly formed from an avoided crossing of two curves (*i.e.*, the wells associated with Rb $ns+ns$ and Cs $np+np$), we can adopt a simple Landau-Zener treatment [33, 52–54], in which we calculate the probability P_{LZ} to make a transition from the electronic state $|\chi_1\rangle$ to the electronic state $|\chi_2\rangle$ (see Figure 3.8):

$$P_{LZ} = \exp\left(-2\pi\frac{|H_{12}|^2}{\hbar v|\frac{d\varepsilon_1}{dR} - \frac{d\varepsilon_2}{dR}|}\right). \tag{3.4.1}$$

Here, H_{12} is the matrix element connecting the two crossing states, ε_i are the nonadiabatic energy levels (assumed to be linear in R), and v is the relative velocity of the two nuclei, determined by the energy of the molecule at some bound level inside the well. Figure 3.8 shows a close-up of the avoided crossing of the

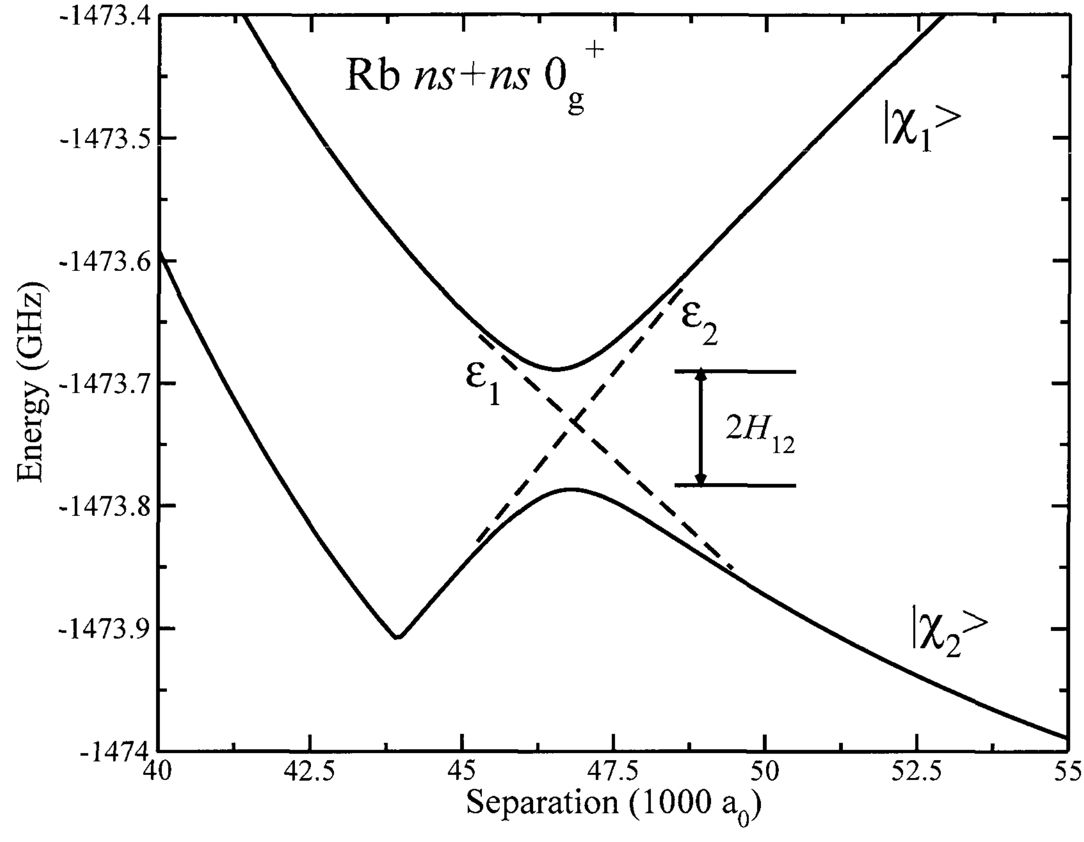

Fig. 3.8: Isolated close up of the avoided crossing between the $|70p_{1/2}69p_{1/2}\rangle$ state ($|\chi_1\rangle$) and the $|68p_{3/2}71p_{3/2}\rangle$ state ($|\chi_2\rangle$) for the 0_g^+ symmetry of rubidium. ε_1, ε_2, and H_{12} are defined as in [52] and [53].

$|70p_{1/2}69p_{1/2}\rangle$ and $|68p_{3/2}71p_{3/2}\rangle$ electronic states for the 0_g^+ symmetry of doubly-excited *ns* rubidium atoms. In this figure, $|\chi_1\rangle$ represents the $|70p_{1/2}69p_{1/2}\rangle$ state and $|\chi_2\rangle$ represents the $|68p_{3/2}71p_{3/2}\rangle$ state; we also label the other relevant features from Equation (3.4.1). By equating the energy level of the bound state (see Tables 3.1 and 3.2) to the molecule's kinetic energy at the equilibrium position R_e, we calculate the relative velocity v, which is treated as a constant in the Landau-Zener approximation. Of course, in reality, the relative velocity varies periodically as the macrodimer vibrates, so the velocity we calculate is actually the maximum velocity, but [53] and [52] show that treating this velocity as constant is valid in the region of the avoided crossing.

Since the result of expression (3.4.1) represents the probability that the macrodimer will predissociate into two free atoms, then $1 - P_{LZ}$ is the probability that the macrodimer will *not* predissociate. We match this probability to remain in $|\chi_1\rangle$ to an exponential decay over the time t for a full oscillation inside the well, *i.e.* $1 - P_{LZ} = e^{-t/\tau}$, and find τ, which is the "predissociation lifetime" of the state. Ultimately, the τ values need to be larger than the lifetimes of the individual Rydberg atoms ($t_{\text{Ryd}} \sim 100\ \mu\text{s}$) [51]. In Tables 3.3 and 3.4, we list the relative velocities v, the Landau-Zener transition probabilities P_{LZ}, and the predissociation lifetimes τ for bound levels corresponding to the six wells that we analyzed using the Landau-Zener method. Our calculations show that the vast majority of the bound levels have very small P_{LZ} values, leading to extremely long ($\sim \infty$) predissociation lifetimes. The three exceptions are for the upper bound levels of the 0_g^+ and 0_u^- symmetries for the rubidium $ns + ns$ asymptote and the 1_u symmetry for the cesium $np + np$ asymptote. Although we note that the lifetimes of the states for all three of these cases get very short ($<$ 1s) as the vibrational levels of the bound states increase, only the lifetimes of the Rb 0_g^+ states ever get smaller than the lifetime of the Rydberg atom t_{Ryd}.

At the end of Section 3.3, we noted that the potential wells associated with the doubly excited np atoms for rubidium are not obviously formed from an avoided crossing of two asymptotic curves. Therefore, using the Landau-Zener treatment on these curves would be neither straightforward nor necessarily accurate. In [55],

Table 3.3: Vibrational energies, relative velocities v, Landau-Zener transition probabilities P_{LZ}, and predissociation lifetimes τ for the bound levels of the 0_g^+, 0_u^- and 1_u symmetries near doubly excited 70s Rb Rydberg atoms. We note that most of the bound levels have near-infinite predissociation lifetimes, but we indicate the cases that do not (see text).

Element	Asymptote	Symmetry	Level	Energy (MHz)	$v_{\max}$ (m/s)	P_{LZ}	τ (s)
rubidium	$70s + 70s$	0_g^+	0	1.035	0.138	4.377×10^{-126}	∞
			1	3.122	0.239	9.841×10^{-73}	∞
			2	5.353	0.314	1.030×10^{-55}	∞
			3	7.478	0.371	2.981×10^{-47}	∞
			4	9.567	0.419	7.378×10^{-42}	∞
			5	11.645	0.462	5.226×10^{-38}	∞
			100	157.771	1.702	7.433×10^{-11}	84.91
			150	218.088	2.001	2.426×10^{-9}	1.8817
			500	538.566	3.145	3.295×10^{-6}	5.611×10^{-4}
			$\gtrsim$500				$\lesssim t_{\text{Ryd}}$
	$70s + 70s$	0_u^-	0	1.034	0.138	2.179×10^{-181}	∞
			1	3.161	0.241	4.545×10^{-104}	∞
			2	5.263	0.311	8.030×10^{-81}	∞
			3	7.332	0.367	1.384×10^{-68}	∞
			4	9.369	0.415	9.310×10^{-61}	∞
			5	11.392	0.457	3.645×10^{-55}	∞
			300	315.641	2.408	4.547×10^{-11}	69.368
			430	426.744	2.800	1.275×10^{-9}	1.8305
			1200	912.485	4.094	8.266×10^{-7}	1.32×10^{-3}
	$70s + 70s$	1_u	0	0.918	0.130	5.709×10^{-571}	∞
			1	2.699	0.222	3.269×10^{-333}	∞
			2	4.468	0.286	3.724×10^{-259}	∞
			3	6.241	0.339	2.186×10^{-219}	∞
			4	7.989	0.383	5.315×10^{-194}	∞
			5	9.748	0.423	1.100×10^{-175}	∞

Table 3.4: Vibrational energies, relative velocities v, Landau-Zener transition probabilities P_{LZ}, and predissociation lifetimes τ for the bound levels of the 0_g^+, 0_u^- and 1_u symmetries near doubly excited $70p$ Cs Rydberg atoms We note that most of the bound levels have near-infinite predissociation lifetimes, but we indicate the cases that do not (see text)

Element	Asymptote	Symmetry	Level	Energy (MHz)	$v_{\max}$ (m/s)	P_{LZ}	τ (s)
cesium	$70p+70p$	0_g^+	0	0 819	0 123	$2\ 81\times10^{\ 746}$	∞
			1	2 458	0 212	$3\ 72\times10^{\ 431}$	∞
			2	4 092	0 274	$2\ 39\times10^{-334}$	∞
			3	5 720	0 324	$6\ 77\times10^{-283}$	∞
			4	7 343	0 367	$9\ 09\times10^{-250}$	∞
			5	8 961	0 405	$3\ 60\times10^{\ 226}$	∞
	$70p+70p$	0_u^-	0	0 948	0 131	$6\ 39\times10^{\ 694}$	∞
			1	2 838	0 228	$2\ 53\times10^{\ 401}$	∞
			2	4 717	0 294	$1\ 86\times10^{\ 311}$	∞
			3	6 591	0 347	$1\ 31\times10^{\ 263}$	∞
			4	8 458	0 394	$8\ 93\times10^{\ 233}$	∞
			5	10 32	0 435	$7\ 39\times10^{-211}$	∞
	$70p+70p$	1_u	0	0 900	0 129	$9\ 78\times10^{-212}$	∞
			1	2 667	0 221	$2\ 79\times10^{\ 123}$	∞
			2	4 422	0 285	$6\ 55\times10^{\ 96}$	∞
			3	6 164	0 336	$2\ 39\times10^{\ 81}$	∞
			4	7 882	0 380	$5\ 04\times10^{-72}$	∞
			5	9 608	0 420	$2\ 67\times10^{\ 65}$	∞
			275	376 019	2 628	$4\ 762\times10^{-11}$	55 61
			375	493 829	3 012	$9\ 835\times10^{\ 10}$	2 050
			1250	1182 95	4 661	$1\ 515\times10^{-6}$	$5\ 56\times10^{\ 4}$
			$\gtrsim$1250				$\sim t_{\mathrm{Ryd}}$

we employed a different method in which we assume that the total probability of nonadiabatic transitions is just a sum of transition probabilities to individual adiabatic curves (a reasonable assumption for the low transition probabilities that we expect). Calculating the nonadiabatic transition probability to a single potential curve is mathematically equivalent to the two-channel problem in the treatment of Feshbach resonances, where the adiabatic potential that supports bound states is the closed channel (labeled as channel 1) and the other potential is the open channel (labeled as channel 2).

The nonadiabatic coupling V_{12} between the two channels originates from the kinetic term of the nuclei

$$T_N = -\frac{m_e}{2\mu}\frac{\partial^2}{\partial R^2}\,, \tag{3.4.2}$$

but since V_{12} is small in our problem, we can keep only the linear term

$$V_{12}(R) = -\frac{m_e}{\mu}\left\langle \chi_1(R)\middle|\frac{\partial}{\partial R}\middle|\chi_2(R)\right\rangle\frac{\partial}{\partial R}\,. \tag{3.4.3}$$

Here, $|\chi_{1,2}(R)\rangle$ are the electronic basis states corresponding to the closed and open channel respectively.

The resonance width of the bound vibrational state $\phi_v(R)$ due to the coupling V_{12} is derived using a Green's function method [56]:

$$\Gamma_{12} = 2\pi\left|\langle\phi_v|\,V_{12}\,|\phi_{\mathrm{reg}}\rangle\right|^2\,, \tag{3.4.4}$$

where $\phi_{\mathrm{reg}}(R)$ is the regular, energy normalized solution of the open channel (in the absence of channel coupling). In our approximation, the total resonance width Γ_1

is just $\Gamma_1 = \sum_i \Gamma_{1i}$, where the sum is over all relevant adiabatic states. The width Γ_{1i} vanishes very fast as the separation between the potentials of the channels increases. In part, this happens because the nonadiabatic coupling is negligible for well-separated potential curves, but also because $\phi_{\text{reg}}(R)$ becomes a highly oscillating function and hence the integral in Eq. (3.4.4) quickly diminishes.

For the three Rb $np + np$ symmetries, the $69s72s$ curve is well separated from other potentials, so again we expect the related nonadiabatic effects to be very small. We calculate lifetimes due to nonadiabatic coupling for the lowest $v = 0, 1, 2$ vibrational levels (see Table 3.1) to the two potential curves immediately below $69s72s$. For the potential curve closest to the well, we find lifetimes in the range of $10^2 - 10^3$ years, while the probability of transitioning to the second curve below $69s72s$ is even more reduced, corresponding to lifetimes of about 10^6 years.

With the exception of the upper levels of the wells associated with the 0_g^+ symmetry of doubly excited ns rubidium atoms, our calculations show that the bound levels are stable with respect to predissociation. These calculations verify our initial assertion that the lack of coupling between the wells and the asymptotes below them should result in stable states. Since the predissociation lifetimes are so high, we safely conclude that the lifetimes of our macrodimers are limited only by the lifetimes of the Rydberg atoms themselves.

3.5 Conclusions

In this chapter, we established that the potential wells we predict are stable with respect to small electric fields. We have identified and described key aspects of the bound molecular levels of the potential wells, including their vibrational energies, their radial wave functions, n-scaling relations, and predissociation lifetimes. The fact that the probability of the excited states predissociating is almost zero is very encouraging. The long-lifetimes of Rydberg atoms means that there should be adequate time to experimentally probe the macrodimers before the atoms decay or ionize. We also described in detail how the ℓ-mixing manifests itself in the potential energy curves corresponding to the potential well. As we will see in the next chapter, the different electronic characters contained in the wells will lead to very interesting results.

As indicated by Tables 3.1 and 3.2, the equilibrium separations of the bound levels are very large compared to traditional molecular states. As the vibrational level inside the well increases, so does the equilibrium separation, ranging from 1-2 μm. Over the years, there have been various proposals for observing quantum mechanical behaviors in macroscopic systems, such as the diffraction of large molecules [57] and using a small mirror to study superpositions as it interacts with a photon [58]. These proposals have been an attempt to find a regime or boundary where quantum mechanics transitions into classical mechanics. In light of their macroscopic sizes, it would be interesting to see if the macrodimers we predict could be used in these efforts.

Chapter 4

Formation Properties

In the previous chapters, we reviewed the theory behind the long-range interactions of two Rydberg atoms and showed that stable bound vibrational levels can exist between identical rubidium and cesium atoms. We also showed that these energy levels are separated enough ($\sim 1-2$ MHz) to give favorable resolution in spectroscopy experiments. In this chapter, we propose a formation scheme similar to the molecular resonance experiment described in Chapter 1 [24], which could produce the predicted macrodimers. Since this formation mechanism is based on a photoassociative process, we first review photoassociation and photoassociation spectroscopy and then use these physical principles to develop our formation scheme.

4.1 Photoassociation

Photoassociation is the process whereby laser light is incident upon two ground level atoms approaching each other. One of the atoms absorbs a photon and forms an excited molecule with the second (ground level) atom. In general, these excited molecular states are not long-lived and can spontaneously decay into either an unbound free state or a bound ground-state molecule; however, because the vibrational period of the formed molecule is much less than the decay time τ_{decay}, one can experimentally probe these bound levels. As we described in Section 3.4, the same is true for macrodimers.

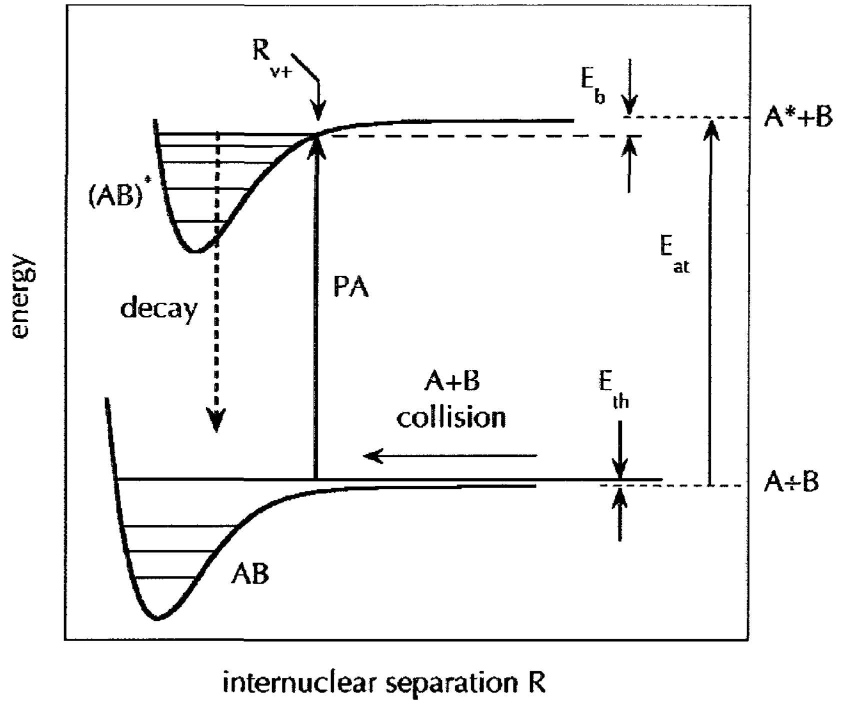

Fig. 4.1: Schematic of a PA scheme taken from [59], describing the process $A + B + \gamma \rightarrow (AB)^*$. The upward arrow labeled 'PA' is the photoassociation transition, while the downward dashed arrow labeled 'decay' indicates radiative decay from the excited molecular state. E_{at} represents the energy to excite atom A at infinite separation (from atom B), E_b is the binding energy of the vibrational level, and E_{th} is the incident thermal collision energy of the ground state atom pair (greatly exaggerated in the figure).

First proposed in [60], photoassociation (PA) spectroscopy has become an invaluable tool in the understanding of long-range molecular potentials for ultracold atoms (see [59, 61, 62], for example). Currently, the two most common experimental detection techniques are radiative trap loss and ion detection. As mentioned above, an excited molecular state formed through photoassociation is not long-lived and quickly fluoresces (see Fig. 4.1). The two decaying atoms are then either too fast to be contained in the trap or they form ground level molecules that are not trapped. Either way, the experiment results in a loss of trapped atoms. By measuring the fluorescence level emitted by the atoms within the trap, the number of trapped atoms can be monitored. For a large sample of atoms, the incident PA laser light is swept through the resonant frequencies of different bound levels, resulting in a spectrum of trap losses. Figure 4.2(a) shows such a spectrum for the 0_g^-, 0_u^+, and 1_g symmetries of $^{39}K_2$, as an example case. The sharp decreases in the fluorescence signal correspond to the bound vibrational levels within the excited molecule; in this instance, the levels immediately below the $4p_{3/2} + 4s_{1/2}$ asymptote.

Ionization detection, on the other hand, relies on a second excitation laser to ionize the molecule before it decays through fluorescence. The resulting molecular ions are counted using a microchannel plate or some other ion detector. This method is often used for the deeper levels of potential wells that are unobservable by trap loss [62]. The main advantages of the ionization method are that there is no background signal and the scan rates are very high because of the production rate of the ionization process. The disadvantage, however, is that there can be difficulties relating the detected ion signals to a PA rate due to the unknown ionization probability [59]. As an example, Figure 4.2(b) shows the ion detection signal of the rotational states corresponding to the $v' = 0$ vibrational level of the $4p_{3/2} + 4s_{1/2}$ molecular state (0_g^- symmetry) for the same trapped potassium atoms as in Fig. 4.2(a).

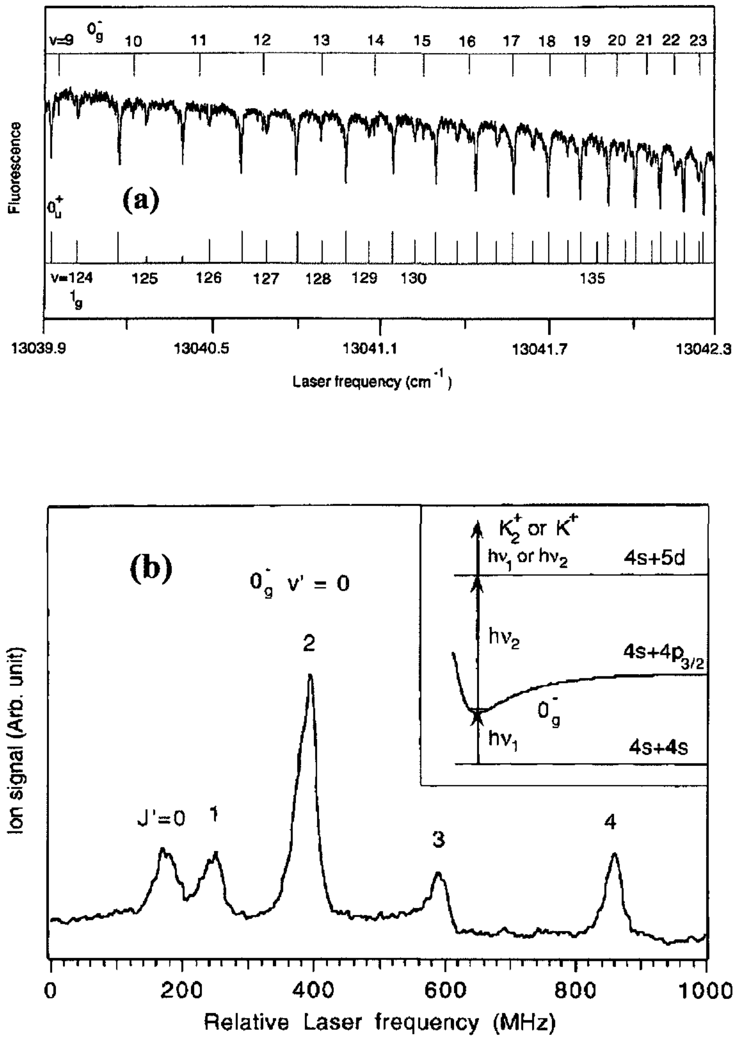

Fig. 4.2: Examples of photoassociation spectra for (a) radiative trap loss and (b) ion detection, both taken from [62]. Figure (a) shows a high-resolution trap-loss spectrum for the bound levels immediately below the $4p_{3/2}+4s_{1/2}$ asymptote of $^{39}\mathrm{K}_2$. The y-axis corresponds to three different molecular symmetries. Figure (b) shows a direct ionization spectrum of the rotational structure of the $0_g^-(4p_{3/2}+4s_{1/2})v'=0$ level for the potassium atoms. The inset shows the photoassociation/ionization scheme.

4.2 Excitation Scheme

Traditional photoassociation is a one-photon process in which one of the ground state atoms becomes excited, but the second atom remains in the ground state. The formation scheme that we propose, however, is a two-photon process whereby both ground state atoms each absorb a photon to become Rydberg atoms, as was done in [24]. In our discussion, we consider excitations to the $70p_{3/2}$ Rydberg state. The second major difference between our proposal and most PA schemes is that we assume the ground state atoms are essentially at rest with respect to each other. Typical PA experiments rely on the relative velocities of the two ground state atoms to give the system some initial energy. The excitation is then from some continuum level of the ground state (see Fig. 4.1). Since the bound states that we predict correspond to extremely large equilibrium positions, we seek to exercise some control over the relative distance between the atoms. As such, we assume that the atoms are initially confined to a harmonic trap. This means that the initial energies of the ground state atoms are given by the discrete bound levels within the trap, rather than by a level of the ground state continuum.

To facilitate our PA process, the ground state atoms are initially excited to intermediate ns, np, or nd Rydberg states. We choose electronic states that have strong dipole coupling with the electronic states composing the well and whose curves have good overlap with the potential well. Since these intermediate states are Rydberg states, we can expect interaction curves similar to those in Chapter 2 and Appendix A to result from this initial excitation (see left panel of Fig. 4.3). It is therefore important to consider the behavior of the molecular curves when choosing appropriate intermediate states. To make the calculations easier, we seek electronic curves that are asymptotically flat in the overlapping R region of the potential well that we consider. As we will see, the PA rate depends on an integral over the separation R. Therefore, choosing electronic curves that are independent of R considerably simplifies the numerical analysis.

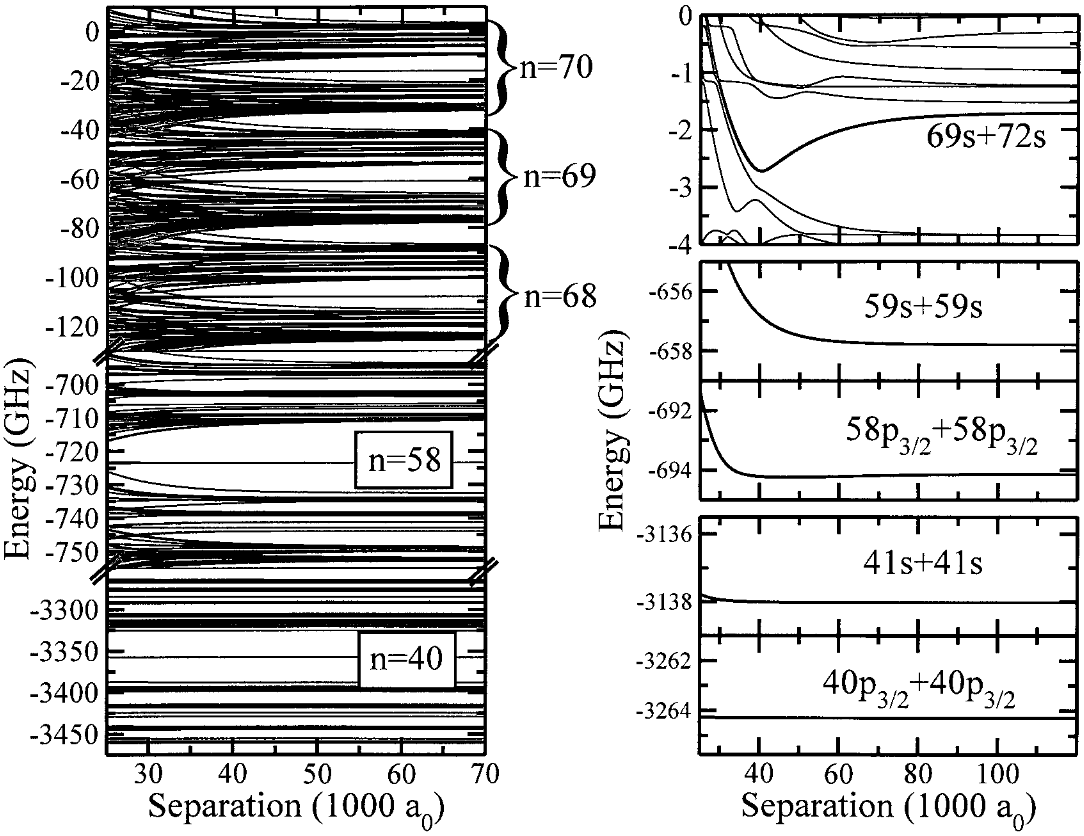

Fig. 4.3: Left column: Asymptotic curves associated with the interactions of two np (black) and two ns (red) rubidium Rydberg atoms (0_g^+ symmetry) for various values of n. As we decrease in energy, the interaction picture shifts to lower values of R (see Section 3.3). Right column: We isolate two $ns+ns$ and $np_{3/2}+np_{3/2}$ curves to show their specific behaviors in the R region of our potential well in the top panel. We choose the $n=40$ curves for our intermediate states because they are asymptotically flat in the region we are concerned with. In both panels, the energy is zeroed at the $70p_{3/2}+70p_{3/2}$ asymptote.

The left panel of Figure 4.3 shows curves for several 0_g^+ rubidium states located around the $np_{3/2} + np_{3/2}$ (black) and $ns + ns$ (red) asymptotes near $n = 70$, 69, 68, as well as near the lower asymptotes $n \sim 58$ and 40. These plots depict the strong mixing of the different ℓ-characters, as well as the R-dependence on the n value. We note that as n decreases, the R range over which the significant ℓ-mixing occurs also decreases, corresponding to a downward shift on the R axis. The result is that the curves correlated to lower n values are asymptotically flat in the R region of the potential well (for the same energy scale). In the right panel of Figure 4.3, we focus in on and enlarge some of the key features of the plots in the left panel. Specifically, we highlight the potential well correlated to the $69s + 72s$ asymptote as well as lower asymptotes that we consider for the intermediate states.

In Section 3.2, we discussed in detail how the potential wells are composed of several molecular electronic states, resulting from the mixing of their respective ℓ-characters. In general, these different electronic characters can be probed and explored by exciting different intermediate Rydberg states. From Figure 3.6, we see that the well highlighted in Fig. 4.3 is mainly composed of $|np; n'p\rangle$ and $|ns; n's\rangle$ electronic states. To probe the $|ns; n's\rangle$ character of the well, we assume transitions from a lower $|n''p; n''p\rangle$ state; likewise, to probe the $|np; n'p\rangle$ character, we assume transitions from a lower $|n''s; n''s\rangle$ state. Using the results of Figure 4.3, we choose $40p_{3/2} + 40p_{3/2}$ and $41s + 41s$ to be the intermediate Rydberg states in our PA scheme. We note that these energy curves are asymptotically flat in the overlapping R region of the potential well and that the dipole couplings between these states and the desired pp' and ss' components are strong enough to facilitate a transition. In the following discussion, we consider these intermediate Rydberg states to be the "ground states" of our PA scheme (see Fig. 4.4).

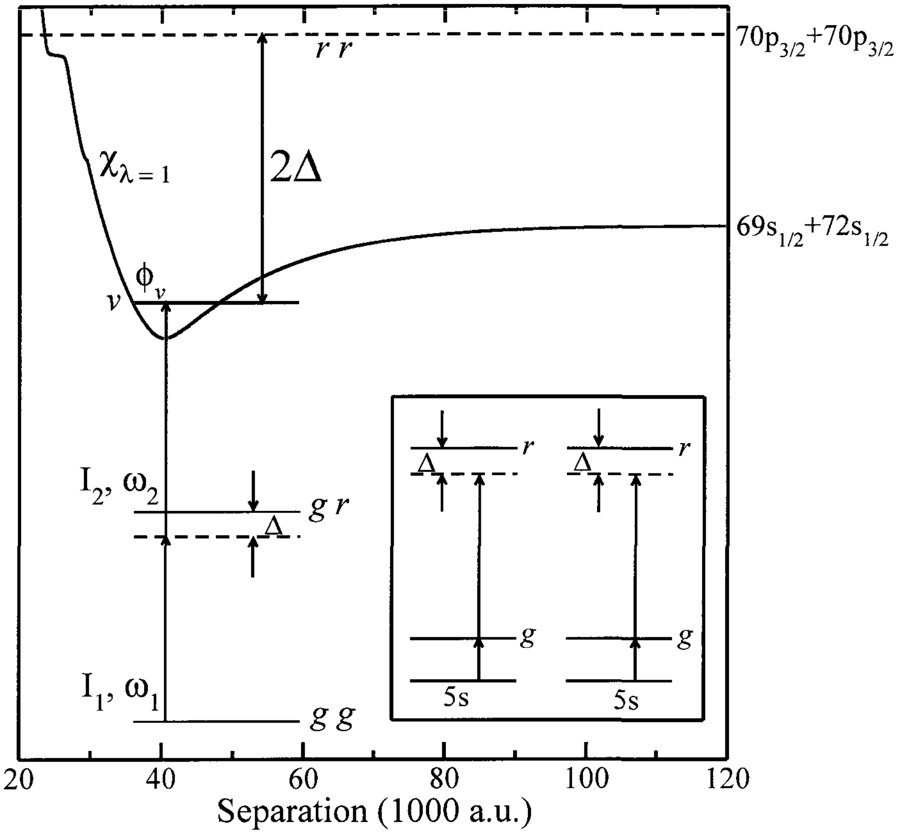

Fig. 4.4: Our proposed two-photon photoassociation scheme for the formation of rubidium Rydberg macrodimers. The ground state atoms are populated to a bound level v inside the well by dual lasers, each of which is red-detuned from the resonance signal of the $70p_{3/2} + 70p_{3/2}$ molecular Rydberg state. Inset: Each rubidium atom is initially excited to an intermediate Rydberg state, considered to be the "ground" state in our discussion (see text). We note that the atomic single detuning levels are not to scale.

In Figure 4.4, we show a schematic diagram for our two-photon PA process. Depending on which electronic character is to be probed, the two interacting atoms would begin in either the $|41s; 41s\rangle$ or the $|40p_{3/2}; 40p_{3/2}\rangle$ electronic state (see above). Each excitation laser should be red-detuned from the resonant frequency with the $70p_{3/2} + 70p_{3/2}$ asymptote. As the total detuning 2Δ is swept through the resonant frequencies of the bound levels ϕ_v, these bound levels will be populated. In Section 3.4, we showed that the deepest bound levels of the potential wells have the longest lifetimes. It is therefore desirable to populate these levels to ensure maximum probing time: thus, we envision an ionization method for experimental detection. Due to the high excitations of Rydberg atoms, they are easily ionized and so we do not anticipate the usual problems associated with ionization detection in traditional PA experiments.

4.3 Calculations and Results

4.3.1 Single photon photoassociation rate

For two ground state atoms approaching along a ground state molecular potential curve with relative velocity v_{rel} and asymptotic kinetic energy ε, the PA rate coefficient describing the transition into a bound level v is given by [63]:

$$\mathsf{K}_v = \left\langle \frac{\pi v_{\text{rel}}}{\kappa^2} \sum_{\ell=0}^{\infty} (2\ell+1) \left| S_{\ell,v}(\varepsilon, I, \Delta) \right|^2 \right\rangle , \tag{4.3.1}$$

where the sum is over all partial waves ℓ. In this expression, κ obeys the dispersion relation $\frac{\hbar^2\kappa^2}{2\mu} = \frac{1}{2}\mu v_{\text{rel}}^2$, with μ being the reduced mass, and $|S_{\ell,v}(\varepsilon, I, \Delta)|$ being the scattering matrix that depends on ε, the laser intensity I, and the laser detuning from resonance Δ. The $\langle \cdots \rangle$ indicates the thermal average over the velocities, which are assumed to obey a Maxwellian distribution. Assuming ultracold conditions (s-wave scattering only), it is readily shown that the PA rate is expressed as an integral over the kinetic energies:

$$\mathsf{K}_v = \frac{1}{hQ_T}\int_0^\infty d\varepsilon \; e^{-\beta\varepsilon}\left|S_{\ell=0,v}(\varepsilon, I, \Delta)\right|^2 , \tag{4.3.2}$$

where $\beta = k_B T$ is the standard constant and $Q_T = \left(2\pi\mu\beta/h^2\right)^{3/2}$ is the partition function.

At MOT temperatures, the scattering matrix $\left|S_v\right|^2$ is well approximated by [63]:

$$\left|S_v(\varepsilon, I, \Delta)\right|^2 = \frac{\gamma_v\gamma_s}{[(\varepsilon-\Delta)^2 + (\gamma/2)^2]} , \tag{4.3.3}$$

where $\gamma = \gamma_v + \gamma_s$ is the total decay rate of the process, with γ_v being the detection rate of product v and γ_s being the stimulated rate between the ground level and the bound level.

4.3.2 Two-photon photoassociation rate

Two-photon photoassociation schemes have been described in great detail [61, 64, 65]. Figure 4.5 (taken from [64]) illustrates the two main formation mechanisms utilized in two-photon photoassociation. We note that both treatments consider a single ground state atom absorbing two incident photons and that a bound level is achieved with each photon absorption. That is to say, these processes all involve photoassociating *twice*.

The two-photon scheme that we propose varies from these processes in the following respects: (a) we assume that *each* ground state atom absorbs one photon to become a Rydberg state and (b) we assume that the excitation of the first

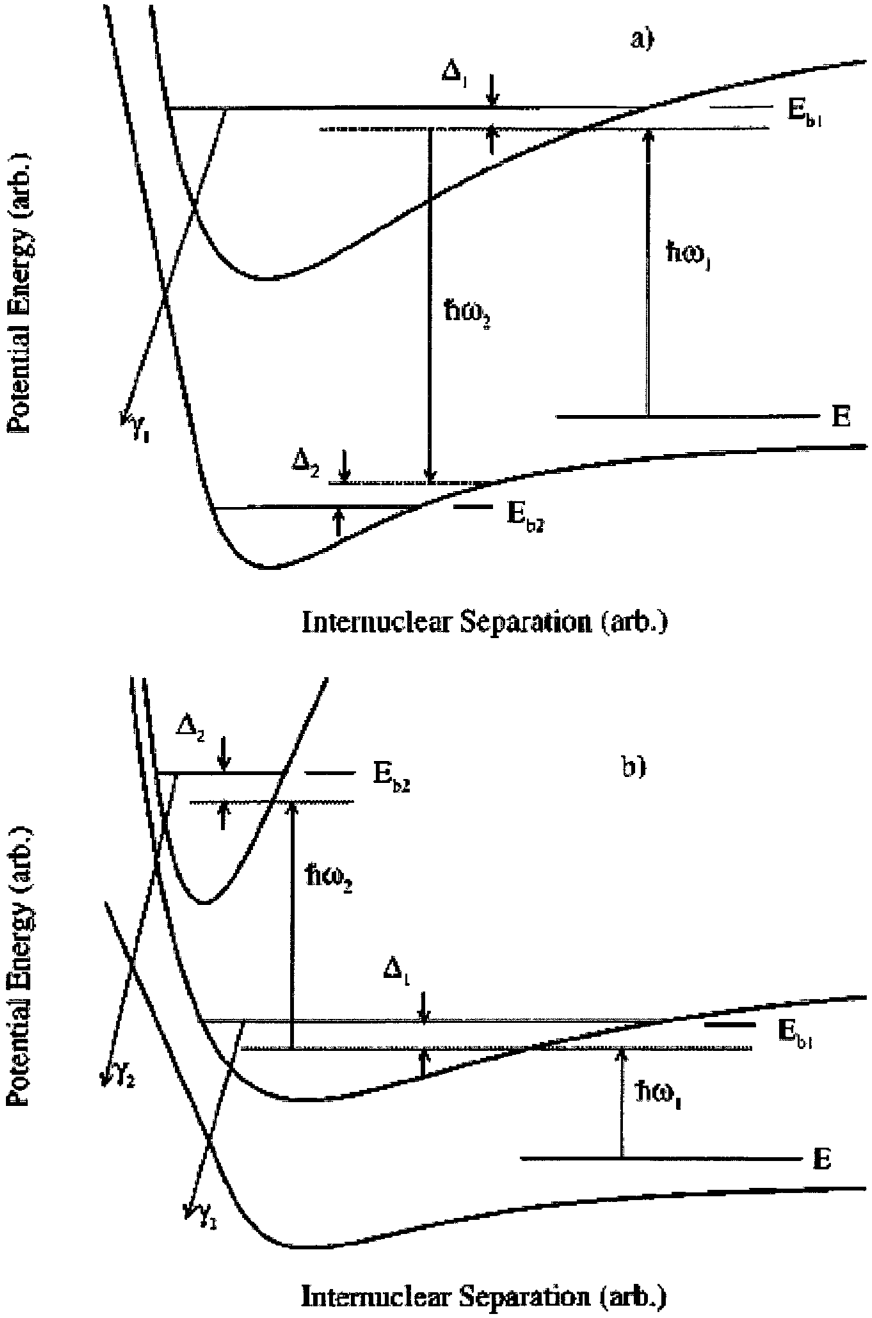

Fig. 4.5: Two photon PA schematic, including energy levels and laser properties, taken from [64]. (a) One ground state atom absorbs a photon to form bound level b_1 with the ground state atom. The excited atom is then de-excited *via* the second photon and the two atoms form a ground state molecule described by level b_2. (b) One ground state atom absorbs a photon to form bound level b_1 with the ground state atom. The excited atom is then further excited *via* the second photon to form bound level b_2 with the ground state atom. In this scenario, b_2 is more energetic than b_1.

atom does not result in a bound state. Since the distance between the atoms is significant, there will be no bonding between the first excited atom and the ground state atom. A bound level v will only be achieved once *both* atoms have been excited. In other words, despite being a two-photon process, we are only photoassociating *once*. We therefore treat our PA scheme as a "modified" single photon PA process, with scattering matrix $|S_v|^2$ given by:

$$|S_v|^2 = \frac{\gamma_v \gamma_s}{\left[(\varepsilon - \Delta_v)^2 + (\gamma/2)^2\right]} \ , \tag{4.3.4}$$

where $\Delta_v \equiv 2\Delta - h\nu_v$ is the detuning from resonance with bound level v *via* laser frequency ν_v and $\gamma = \gamma_1 + \gamma_2 + \gamma_v + \gamma_s$ is the total decay rate during the two photon process. Here, 2Δ is the total atomic detuning defined in Figure 4.4, γ_i represents the spontaneous decay rate of Rydberg atom i, γ_v is the detection rate of product v as before, γ_s is the stimulated rate between the molecular ground level and the molecular bound level. For this scheme, the stimulated rate is given by an "effective" two-Rabi product,

$$\gamma_s = 2\pi \left(\frac{2\pi I_1}{c}\right) \left(\frac{2\pi I_2}{c}\right) \left|\langle \Psi_v^{(\lambda)}(R) | D(R) | \Psi_g(R) \rangle\right|^2 \ , \tag{4.3.5}$$

where $|\Psi_v^{(\lambda)}(R)\rangle = |\phi_v(R)\rangle \otimes |\chi_v(R)\rangle$ is the bound state wave function, $|\Psi_g(R)\rangle = |\phi_g(R)\rangle \otimes |\chi_g(R)\rangle$ is the ground state wave function, I_i is the intensity of laser i and $D(R)$ is the molecular dipole moment connecting the ground and excited electronic states. From our earlier discussion, the electronic state of the ground level will either be $|41s; 41s\rangle$ or $|40p_{3/2}; 40p_{3/2}\rangle$. Therefore, we represent the electronic ground state wave function as $|\chi_v(R)\rangle \equiv |a_g; a_g\rangle$, where $a_g \equiv n_g \ell_g j_g m_{j_g}$.

Applying Equation (3.2.2) for $|\chi_v(R)\rangle$, we write:

$$\gamma_s = 2\pi \left(\frac{4\pi^2 I_1 I_2}{c^2}\right) \sum_{\jmath} |\langle \jmath | D(R) | a_g; a_g\rangle|^2 \left|\langle \phi_v(R) | c_\jmath^*(R) | \phi_g(R)\rangle\right|^2 . \tag{4.3.6}$$

Given the large separation between the atoms, we treat the "molecular" dipole transition as a product of the two atomic transitions, *i.e.*

$$\begin{aligned} \langle \jmath | D(R) | a_g; a_g\rangle &\equiv \langle n_\jmath \ell_\jmath | e r_1 | n_g \ell_g\rangle \langle n'_\jmath \ell'_\jmath | e r_2 | n_g \ell_g\rangle \\ &= d_{1,\jmath} d_{2,\jmath} , \end{aligned} \tag{4.3.7}$$

where $e = 1$ in atomic units. The stimulated rate then takes the final form:

$$\gamma_s = 2\pi \left(\frac{4\pi^2 I_1 I_2}{c^2}\right) \sum_{\jmath} |d_{1,\jmath} d_{2,\jmath}|^2 \left| \int dR \; \phi_v^*(R) c_\jmath^*(R) \phi_g(R) \right|^2 . \tag{4.3.8}$$

Here, the integral is calculated *via* a simple trapezoidal numerical integration scheme. Due to the sinusoidal nature of $\phi_v(R)$ (see Section 3.2), the trapezoid method converges very quickly and so the error is minimal [66]. The radial ground state wave functions are determined by the experimental parameters; we give an example in the next section.

As we showed in Section 3.4, the macrodimer lifetime is dictated by the lifetimes of the two Rydberg atoms that compose it. We can thus assume that the rate of detection γ_v is on the same order as the spontaneous decay rates γ_1 and γ_2, *i.e.* $\gamma_1 + \gamma_2 + \gamma_v \sim 3\gamma_v$. Under the weak field limit, we can also assume that $\gamma_v \gg \gamma_s$, since $\gamma_s \propto I_1 I_2$ and the lifetimes of Rydberg atoms are very long. This means that the total decay rate in the denominator of Equation (4.3.4), is given by $\gamma \approx 3\gamma_v$. Letting $(\varepsilon - \Delta_v) = x$ and $2/(3\gamma_v) = n$ in Eq. (4.3.4), it is trivial to show that the scattering matrix takes the form

$$|S_v|^2 = \frac{2\pi}{3}\gamma_s \left[\left(\frac{n}{\pi}\right)\frac{1}{1+n^2x^2}\right] , \tag{4.3.9}$$

where the term inside the square brackets approximates a dirac delta function $\delta(x) = \delta(\varepsilon - \Delta_v)$. Therefore, we define the PA rate for our two photon process as

$$\mathsf{K}_v = \left\langle \frac{2\pi}{3}\gamma_s\,\delta(\varepsilon - \Delta_v) \right\rangle , \tag{4.3.10}$$

where the $\langle\cdots\rangle$ indicate a thermal average over the kinetic energies, as in Eq. (4.3.2).

4.3.3 Harmonic trap

Typical photoassociation experiments excite free atoms from a continuum level of the ground state into a bound molecular level v. However, to exercise better control over the Rydberg atoms, we envision confining the atoms to a one-dimensional harmonic trap and exciting them from bound levels within this trap. Such trapping could be achieved *via* optical tweezers [67], a 1-D optical lattice, or a 1-D MOT. The thermal average in Equation (4.3.10), is then defined by a *summation* over the energies, not an integral:

$$\begin{aligned}\mathsf{K}_v &= \frac{2\pi}{3Z}\sum_n \gamma_s^{(n)}\, e^{-\beta E_n}\delta_{E_n,\Delta_{v,n}} \\ &= \frac{A}{Z}\sum_n \left[\sum_j |d_{1,j}d_{2,j}|^2 \left|\int dR\ \phi_v^*(R)c_j^*(R)\phi_g^{(n)}(R)\right|^2 e^{-\beta E_n}\delta_{E_n,\Delta_{v,n}}\right] ,\end{aligned} \tag{4.3.11}$$

where $Z = \sum_n \exp\left(-\beta E_n\right)$ is the partition function, we have let $A \equiv \frac{\left(4\pi^2\right)^2 I_1 I_2}{3\,c^2}$, and we have changed the dirac delta function to the kronecker delta function, consistent with the discrete case. We have also rewritten the detuning Δ_v as $\Delta_{v,n}$ to explicitly denote the dependence of the detuning on the ground level n. For a one dimensional harmonic trap, the energies are given by $E_n = \hbar\omega(n + 1/2)$ and the ground state wave functions are the solutions to the harmonic oscillator, *i.e.*

$$\phi_g^{(n)}(R) = \sqrt{\frac{1}{2^n n!}} \left(\frac{m\omega}{\pi\hbar}\right)^{1/4} H_n\left(\sqrt{\frac{m\omega}{\hbar}}R\right) e^{-\frac{m\omega}{2\hbar}R^2} \,. \tag{4.3.12}$$

In this expression, m is the mass of a single rubidium atom and ω is the trap frequency. In the following analysis, we have assumed a trap frequency $\omega \sim 60$ kHz, leading to a trap width roughly equivalent to that of the potential well, and a temperature of 100 μK. Both values are within experimental parameters but can be adjusted as needed. In Figure 4.6, we show PA signals for thermally averaged transition rates from the $41s + 41s$ electronic curves (turquoise) and the $40p_{3/2} + 40p_{3/2}$ electronic curves (red) for the $0 \leq n \leq 50$ harmonic levels on a linear scale in (a) and a logarithmic scale in (b) plotted against the atomic detuning Δ. Inset (c) focuses on the rate signals between $\Delta = -1.15$ GHz and $\Delta = -0.93$ GHz.

From Figure 4.6, we note that the strengths of both rate signals are strongest in the deepest part of the well, where the atomic detuning is largest. As the detuning decreases, the relative signal strengths also decrease. Although the $40p_{3/2} + 40p_{3/2}$ signal is stronger overall (corresponding to the larger ss' character inside the well), we point out that there are regions where the $41s + 41s$ signal is stronger. In particular, we zoom in on the detuning range between -1.15 GHz and -0.93 GHz.

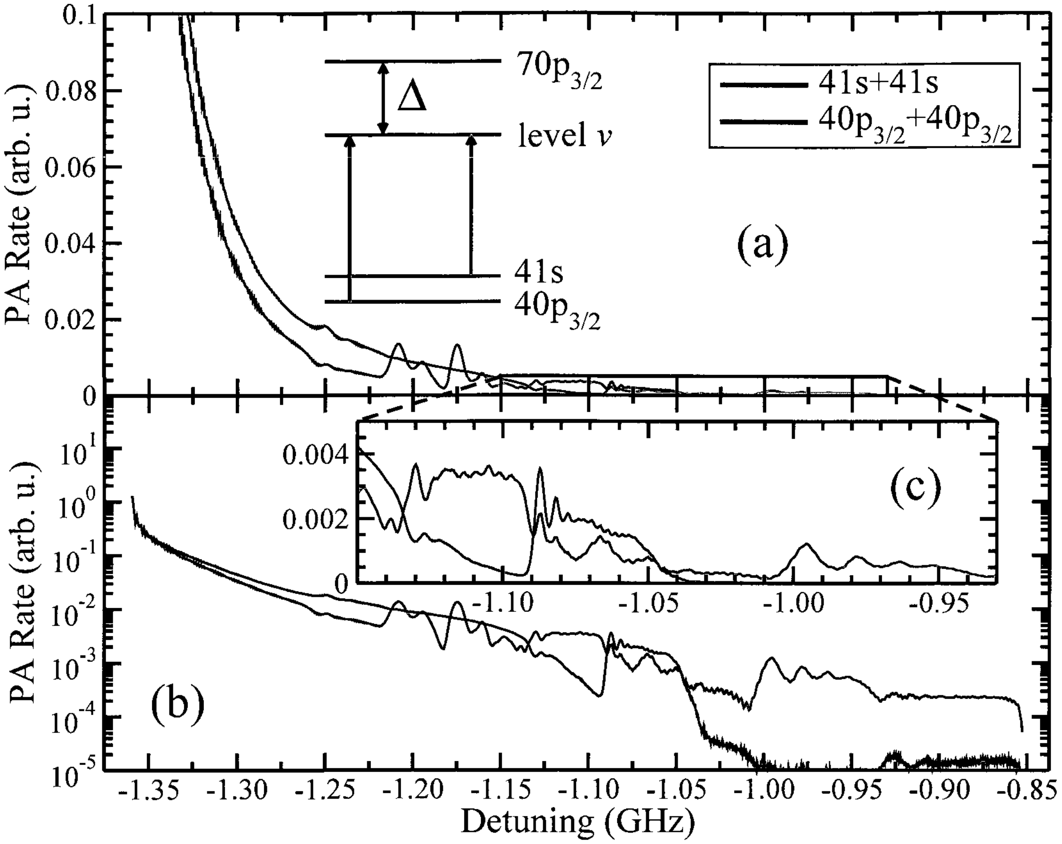

Fig. 4.6: PA rate vs. the detuning Δ from the $70p_{3/2}$ atomic state on (a) a linear scale and (b) a logarithmic scale for thermally averaged transitions from harmonic oscillator bound states. We assume transitions from the $41s + 41s$ electronic state (turquoise) to access the pp' character inside the well and the $40p_{3/2} + 40p_{3/2}$ electronic state (red) to access the ss' character (see text). The signals are strongest in the deepest part of the well and gradually decrease as the detuning decreases. In (c), we zoom in on the portion between $\Delta = -1.15$ GHz and $\Delta = -0.93$ GHz, highlighting the behavior of the two signals.

In this region of the well, the two signals essentially flip back and forth based on the relative pp' and ss' characters of the well. This indicates a possibility of controlling the formation of macrodimers based on the equilibrium separation of the two nuclei and the electronic character of the ground state. Such control could be useful in developing a "switch" for quantum information processes and quantum computing.

Finally, we point out that that at $\Delta \sim -1.05$ GHz, the two rate signals (but particularly the $40p_{3/2}$ signal) decay towards zero, even though there are still a significant number of bound states left to populate. The sharp decreases in the strengths of the signals are due to the assumed width of the harmonic trap. Although we used a harmonic trap of width roughly equal to that of the well for our calculations, the potential well clearly widens anharmonically towards the top, leading to equilibrium separations beyond the range of the trap. The higher bound levels could be more easily accessed by widening the trap width. For example, the isolated $69s + 72s$ character at $R \geq 55\ 000\ a_0$ could be probed in this manner.

4.4 Conclusions

In this chapter, we have presented a theoretical formation scheme that, in principle, could realize the macrodimers we predict in Chapter 2. Our formation mechanism consists of a two-photon excitation procedure, where each ground state atom is excited to a Rydberg state. Unlike most photoassociation experiments, we assume that the ground state atoms are initially confined to a harmonic trap and are thus excited from discrete energy levels and not from continuum levels. By red-detuning the excitation lasers off of the resonance signal of the $n\ell$ Rydberg state, we should be able to populate the bound energy levels calculated in Tables 3.1 and 3.2.

One of the key aspects of our formation scheme is that we are able to consider excitations from multiple "ground states" to populate the same bound levels within the well. Due to the electronic mixing described in Chapter 3, the potential well takes on various ℓ-characters, which support transitions from any state having good dipole transitions to any of the electronic states composing the well. The flexibility to use different ground states is encouraging from an experimental standpoint.

We have presented photoassociation rates for transitions from $41s + 41s$ states to populate the pp' character inside the well and from $40p_{3/2} + 40p_{3/2}$ to populate the ss' character, based on a harmonic trapping potential. We find that the behaviors of the rate signals reveal details of the well's electronic composition. What is particularly interesting is the decay of the $40p_{3/2}$ signal around $\Delta \sim -1.15$ GHz, where the $41s$ signal increases. Being able to control the excitations of bound molecules indicates the possibility of a quantum mechanical "switch." Combining this effect with the Rydberg blockade phenomena [9] could have consequences in quantum information and quantum computing.

Chapter 5

Three-body Interactions

With the discoveries of laser cooling and trapping [68] and then evaporative cooling [69, 70], the study of new physical systems at ultracold temperatures has exploded. The realizations of Bose-Einstein Condensation [71–73] and photoassociation spectroscopy [61, 62] led to great strides in the understanding of the interactions between atoms and many-body physics in degenerate quantum systems with strongly interacting particles.

However, over the past five years or so, the focus of study has moved away from binary interactions and toward few-body interactions, such as between atom-diatom interactions [74–76] and diatom-diatom interactions [77, 78]. Extending our two-body calculations to a three-body interaction picture is a logical next step. Although there have been proposals for such ultra-long-range Rydberg atom interactions [79–81], these works focus on the interactions between one Rydberg atom and multiple ground state atoms. Here, we describe the long-range interactions between three Rydberg atoms.

5.1 Formulation

5.1.1 The Basis

In general, adding a third atom to the interaction picture will change the symmetry of the system. However, to simplify the calculations, we assume three identical Rydberg atoms along a common (z-) axis, which preserves the $D_{\infty h}$ symmetry. This also permits the use of much of the two-body physics from Chapter 2 for the three-body system. Obtaining properly symmetrized basis functions for the three-atom case is very similar to that of the two-atom case, but much more technically demanding. In Appendix B, we show that the symmetrized three-atom wave functions for long-range Rydberg atoms with non-overlapping electronic clouds (no exchange) have the form:

$$\begin{aligned} |a_1;a_2;a_3\rangle = \frac{1}{\sqrt{6}} & \left[\left(|a_1\rangle_1 |a_2\rangle_2 |a_3\rangle_3 + |a_2\rangle_1 |a_3\rangle_2 |a_1\rangle_3 + |a_3\rangle_1 |a_1\rangle_2 |a_2\rangle_3 \right) \right. \\ & \left. - p(-1)^{\ell_1+\ell_2+\ell_3} \left(|a_1\rangle_1 |a_3\rangle_2 |a_2\rangle_3 + |a_2\rangle_1 |a_1\rangle_2 |a_3\rangle_3 + |a_3\rangle_1 |a_2\rangle_2 |a_1\rangle_3 \right) \right] . \qquad (5.1.1) \end{aligned}$$

Here $|a_\imath\rangle_k \equiv |n_\imath, \ell_\imath, j_\imath, m_{j_\imath}\rangle_k$ represent the quantum states of the free Rydberg atom k (as in Chapter 2) with principal quantum number $n_\imath$, orbital angular momentum quantum number $\ell_\imath$, and the projection $m_{j_\imath}$ of the total angular momentum $\vec{j}_\imath = \vec{\ell}_\imath + \vec{s}_\imath$ onto the internuclear axis. As defined previously, $p = +1(-1)$ for gerade (ungerade) molecular states. We note the similarity between Equation (5.1.1) and its two-body counterpart (Equation (2.2.1)). Both expressions show that the total wave function is a superposition of the cyclic and non-cyclic permutations of the individual atomic states, and that the non-cyclic states are (anti-)symmetrized via $-p(-1)^{\sum_\imath \ell_\imath}$.

To construct the interaction picture for the three-atom system, we build basis sets with which to diagonalize the interaction Hamiltonian. As in the two-atom case, each basis set consists of the excited Rydberg molecular level and nearby asymptotes with significant coupling to this level and to each other. However, due to the number of three-atom combinations, there are many more local asymptotes to consider than in the two-body case. This results in basis sets that are significantly larger than their two-atom counterparts. In this chapter, we consider the case of triply excited $58p$ rubidium atoms as an example.

5.1.2 Long-range Interactions

Following the methodology of the two-body case, we assume that the Rydberg atoms interact via long-range dipole-dipole and quadrupole-quadrupole couplings, resulting in the mixing of different electronic states. As before, we diagonalize an interaction Hamiltonian consisting of long-range Rydberg interactions and atomic fine structure, *i.e.* $H_{\text{int}} = V_{3-\text{body}} + H_{fs}$. Using the wave functions defined by Equation (5.1.1), we write the matrix elements of the Hamiltonian as the sums of multiple interactions. We define the matrix elements of the interaction Hamiltonian as:

$$\begin{aligned}\langle a_1; a_2; a_3 | V_{3-\text{body}} | b_1; b_2; b_3 \rangle = \\ \frac{1}{6} \sum_{\substack{i,j,k \\ i',j',k'}} \langle a_i^{(1)} a_j^{(2)} a_k^{(3)} | V_{3-\text{body}} | b_{i'}^{(1)} b_{j'}^{(2)} b_{k'}^{(3)} \rangle \qquad (5.1.2) \\ \times \left(\Theta_C + p_a (-1)^{\ell_i + \ell_j + \ell_k} \Theta_A \right) \left(\Theta_C + p_b (-1)^{\ell_{i'} + \ell_{j'} + \ell_{k'}} \Theta_A \right) \ ,\end{aligned}$$

where each summation index is over the total number of atoms, *i.e.* from 1 to 3 and we have defined

$$\Theta_C = \begin{cases} -1 & \text{for cyclic permutations} \\ 0 & \text{for anti-cyclic permutations} \end{cases} \quad \text{and} \quad \Theta_A = \begin{cases} 0 & \text{for cyclic permutations} \\ -1 & \text{for anti-cyclic permutations} \end{cases}$$

and $|a_i^{(1)} a_j^{(2)} a_k^{(3)}\rangle \equiv |a_i\rangle_1 |a_j\rangle_2 |a_k\rangle_3$, etc. In the case that $|a_1; a_2; a_3\rangle = |b_1; b_2; b_3\rangle$ (*i.e.* along the diagonal of the matrix), the matrix element is given by:

$$\langle a_1; a_2; a_3 | H_{\text{int}} | a_1; a_2; a_3\rangle = \langle a_1; a_2; a_3 | V_{3-\text{body}} | a_1; a_2; a_3\rangle + E_{123} \ , \tag{5.1.3}$$

with $E_{123} = E_1 + E_2 + E_3$, where $E_k = -\dfrac{1}{2(n_k - \delta_{\ell_k})^2}$ are the atomic Rydberg energies.

The long-range assumption that the distance R between any two atoms is greater than the LeRoy Radius R_{LR} assures that these are three free atoms interacting *via* the long-range two-body potentials defined by Eq. (2.3.5). Thus, the transition element $\langle a_i^{(1)} a_j^{(2)} a_k^{(3)} | V_{3-\text{body}} | b_{i'}^{(1)} b_{j'}^{(2)} b_{k'}^{(3)}\rangle$ from Equation (5.1.2) is defined as a sum of two body interactions, *i.e.*

$$\begin{aligned} \langle a_i^{(1)} a_j^{(2)} a_k^{(3)} | V_{3-\text{body}} | b_{i'}^{(1)} b_{j'}^{(2)} b_{k'}^{(3)}\rangle &= \langle a_i^{(1)} a_j^{(2)} | V_L(R_{12}) | b_{i'}^{(1)} b_{j'}^{(2)}\rangle \\ &+ \langle a_j^{(2)} a_k^{(3)} | V_L(R_{23}) | b_{j'}^{(2)} b_{k'}^{(3)}\rangle \\ &+ \langle a_i^{(1)} a_k^{(3)} | V_L(R_{13}) | b_{i'}^{(1)} b_{k'}^{(3)}\rangle \ . \end{aligned} \tag{5.1.4}$$

Since we are assuming that the three atoms lie along a common axis, each interaction term $\langle a_i^{(\alpha)} a_j^{(\beta)} | V_L(R_{\alpha\beta}) | b_{i'}^{(\alpha)} b_{j'}^{(\beta)}\rangle$ is the long-range Rydberg-Rydberg transition element, as defined previously in Equation (2.3.8), with $L = 1(2)$ for dipole (quadrupole) interactions, and $R_{\alpha\beta}$ being the distance between atoms α and β.

5.2 Results

In this section, we provide preliminary results on triply excited $58p$ rubidium Rydberg atoms. We include a few examples of potential energy surfaces (PES), each of which coresponds to a different asymptotic level with a different physical "topography." Although we ultimately seek surfaces that illustrate potential wells (indicating bound three-atom systems), much can be learned about the long-range interactions from other types of surfaces. In what follows, R_1 represents the distance between atom 1 and atom 2 in a_0, R_2 represents the distance between atom 2 and atom 3 in a_0, and the z-axis measures the energy in GHz. The respective color schemes for each plot are also given in the scale to the right of each surface plot.

Figures 5.1 and 5.2 illustrate potential surfaces analogous to two-dimensional attractive and repulsive potential curves, respectively. The attractive PES shown in Fig. 5.1 corresponds to the $|57s_{1/2}; 57d_{5/2}; 58d_{3/2}\rangle$ state, while the repulsive PES shown in Fig. 5.2 corresponds to the $|58p_{3/2}; 56p_{3/2}; 60p_{3/2}\rangle$ state. We see that in both cases, the distance of the third atom has very little effect on the other two atoms: as either R_1 or R_2 is increased (while keeping the other distance fixed), the two stationary atoms consistently demonstrate an attractive/repulsive behavior.

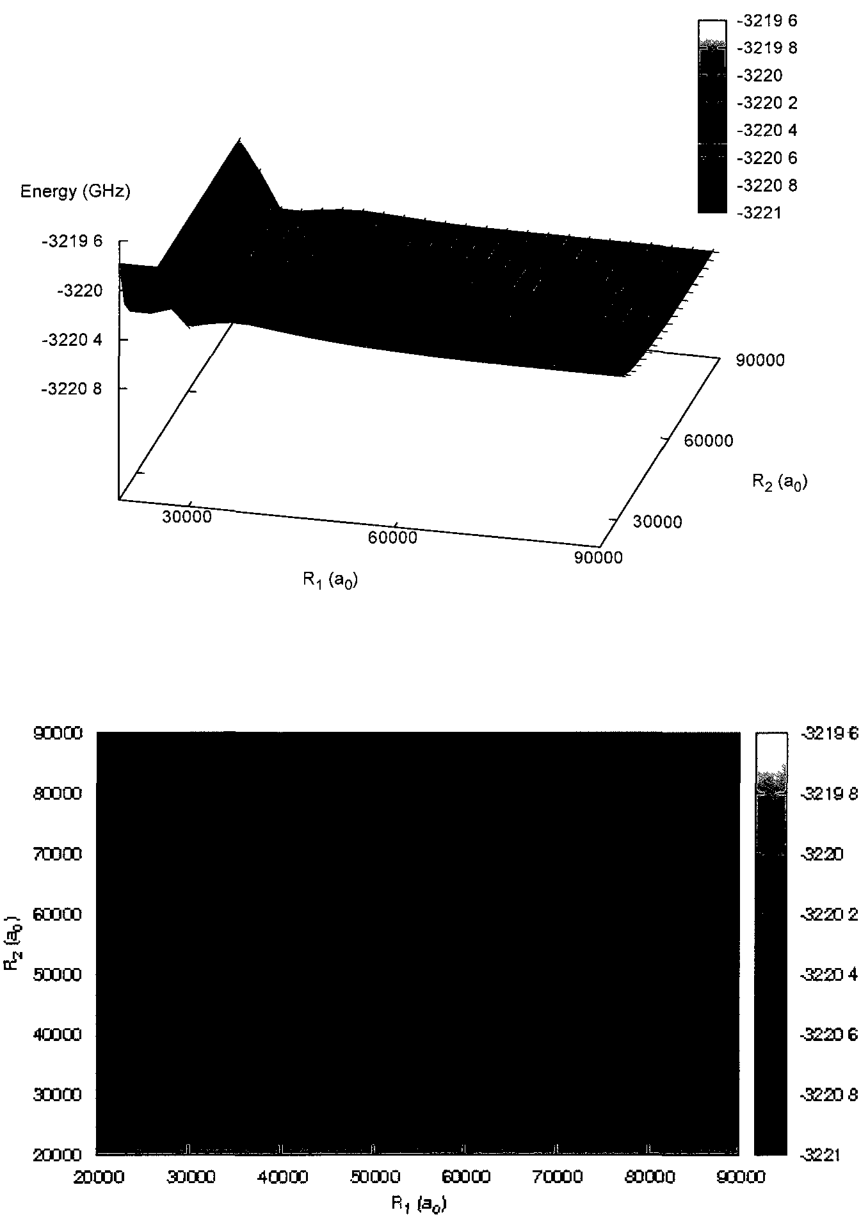

Fig. 5.1: (top) Potential energy surface (PES) and (bottom) two-dimensional projection correlated to the $|57s_{1/2}; 57d_{5/2}; 58d_{3/2}\rangle$ asymptotic state. This surface is analogous to an attractive potential curve for the two-body case: As the distance of either the first (R_1) or last (R_2) atom in the linear chain is increased, the two local atoms are attracted.

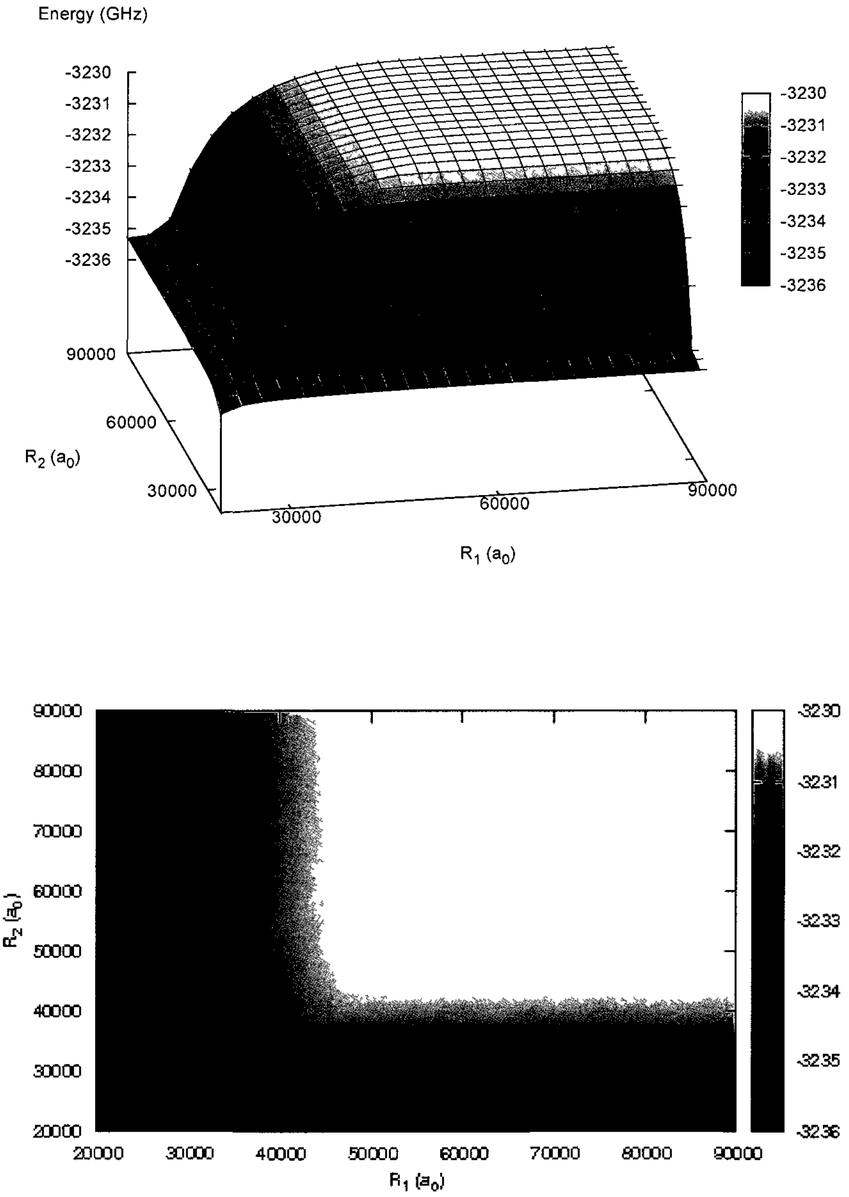

Fig. 5.2: PES (top) and projection (bottom) correlated to the $|58p_{3/2}; 56p_{3/2}, 60p_{3/2}\rangle$ asymptotic state This surface is analogous to a repulsive potential curve for the two-body case: As the distance of either the first (R_1) or last (R_2) atom in the linear chain is increased, the two local atoms are repulsed.

Figure 5.3 shows the PES for the triply excited $58p_{3/2}$ state, *i.e.* $|58p_{3/2}; 58p_{3/2}; 58p_{3/2}\rangle$. This surface illustrates the obvious symmetry along the $R_2 = R_1$ axis that we would expect for three identical atoms. The interesting feature of this plot is the two "ridges" that run along either axis. These ridges indicate that the two local atoms form a bonded pair, existing even as the third atom is moved away. However, as the third atom is moved sufficiently far from these two bound atoms, all three atoms dissociate. It would seem that the bond between the two local atoms is contingent upon the presence of the third atom.

In figure 5.4, we depict the PES correlated with the $|58d_{3/2}; 57d_{5/2}; 55d_{3/2}\rangle$ asymptotic state. The highlight of this particular plot is the (3-D) potential well indicated by the black area centered at approximately $R_1 = 37\,000\ a_0$, $R_2 = 31\,000\ a_0$. Such a well indicates that all the three Rydberg atoms form a long-range linear *macrotrimer*. Based on the energy scale, this particular well is approximately 30 MHz deep; significantly shallower than the wells we highlighted in the two-atom case, but we suspect that this is deep enough to support at least a few bound vibrational levels. We believe that we should also be able to calculate the different vibrational modes based on a classical system, *i.e.* treating the atoms as masses connected by springs.

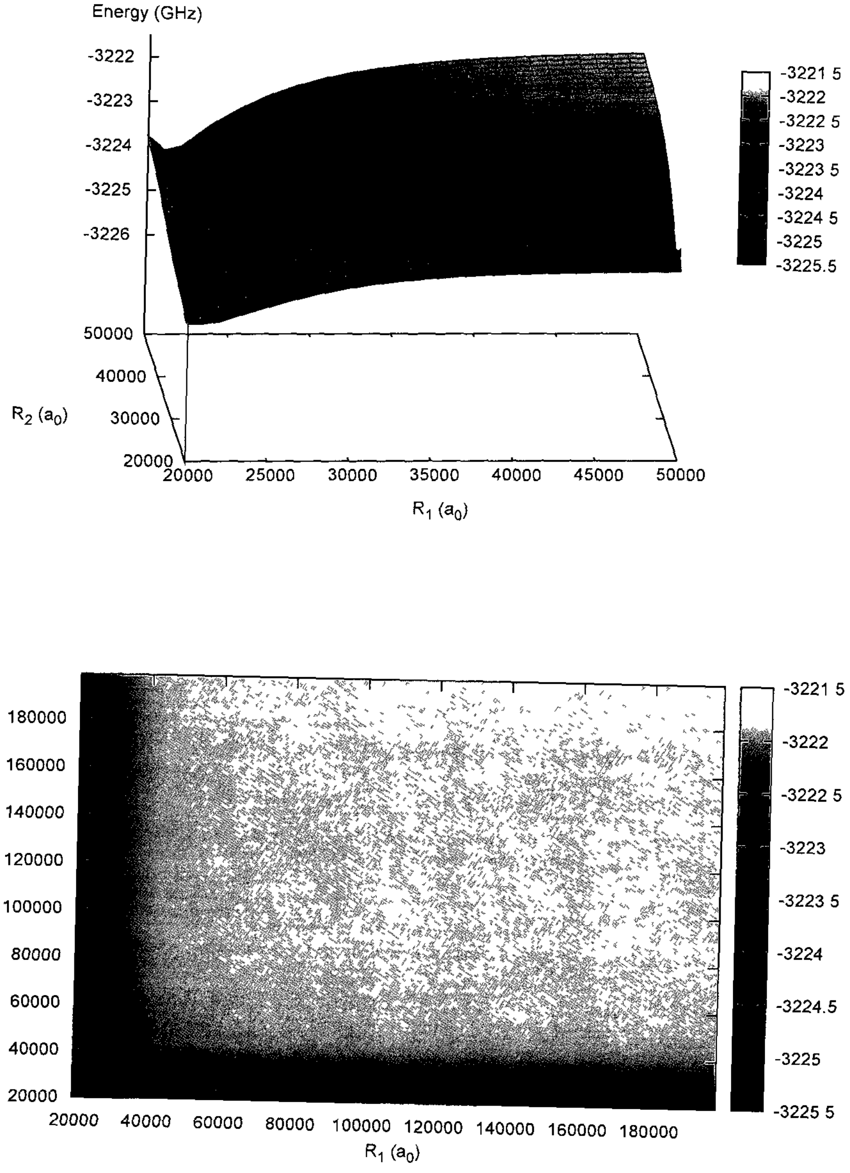

Fig. 5.3: PES (top) and projection (bottom) correlated to the $|58p_{3/2}; 58p_{3/2}; 58p_{3/2}\rangle$ asymptotic state. We note the "ridges" lying along both the R_1 and R_2 axes, which indicate that the two local atoms are bound (see text). To better show the energy gradient and the "ridges," the surface plot (top) needed to be plotted over a shorter range than the projection (bottom).

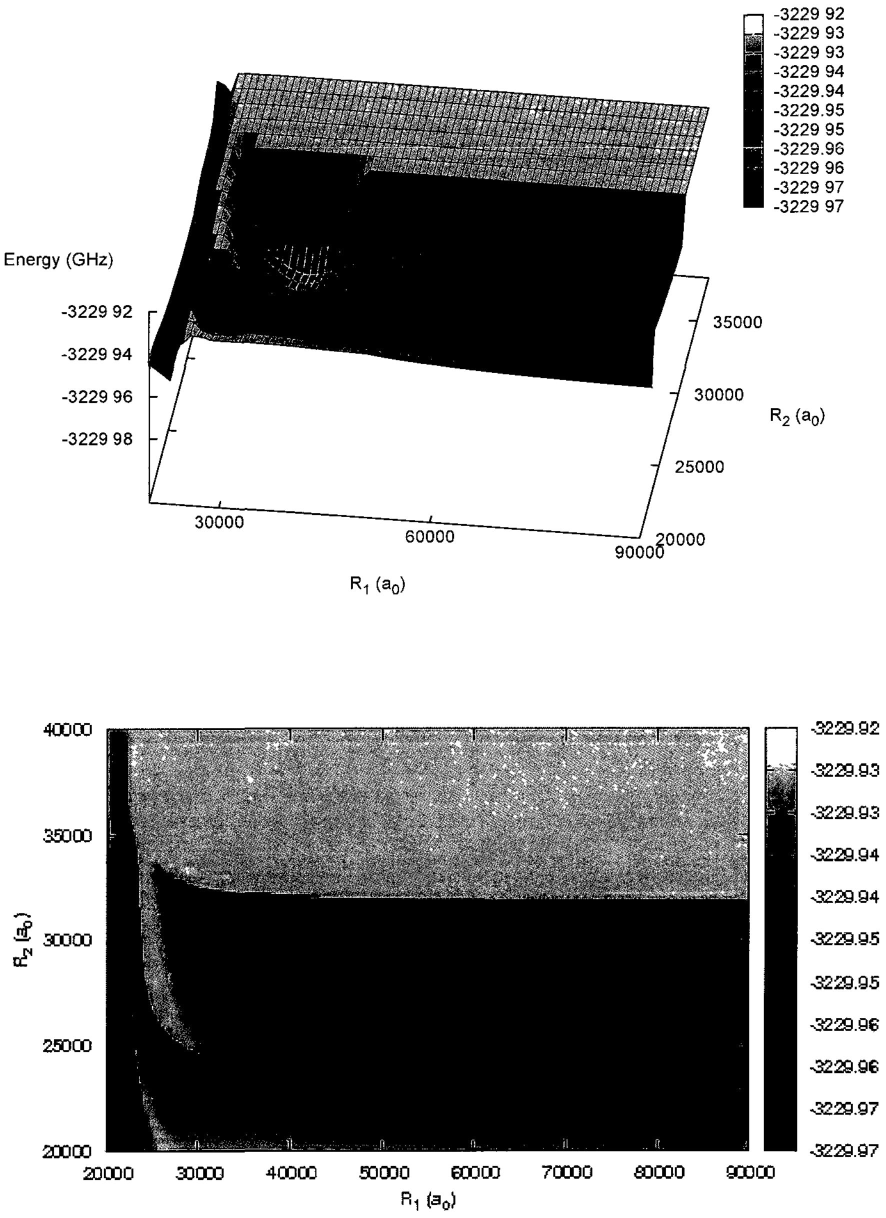

Fig. 5.4: PES (top) and projection (bottom) correlated to the $|58d_{5/2}; 57d_{3/2}; 55d_{3/2}\rangle$ asymptotic state. The main feature of this surface plot is the 3-D well, centered at about R_1 = 37 000 a_0, R_2 =31 000 a_0, indicating that the three atoms are bound together in a linear chain (see text).

The final PES that we present here is for the $|58d_{5/2}; 57d_{5/2}; 55d_{3/2}\rangle$ state. This is a particularly intriguing surface because of the complexity of the interaction picture as indicated by the richness of features in the surface. For example, along the R_1-axis between 20 000 $a_0 \leq R_2 \lesssim$ 35 000 a_0, we note a series of "ripples" in the PES. Also of note is a large "ridge" lying along the R_2-axis (beginning at about $R_2 \sim$ 55 000 a_0 and centered at about $R_1 =$ 30 000 a_0), indicating that the two local atoms could be in a bound state provided that the third atom is sufficiently far away.

Although all of the figures illustrate different surfaces with different features, we note that they all have one feature in common. As the distances R_1 and R_2 between the atoms become large enough, the surfaces become flat, indicating that the atoms have completely dissociated into free atoms (as should be expected in the asymptotic limit).

5.3 Outlook

Although there is still work to be done regarding the calculations that we have presented in this chapter, we are encouraged by the preliminary results. As stated in the introduction of this chapter, the current literature regarding ultracold multi-body Rydberg physics involves one Rydberg atom interacting with multiple ground state atoms. To our knowledge there have been no published results regarding multiply-bound Rydberg atoms, which makes our initial results promising.

In addition to completing this work on the linear trimers, we are also interested in

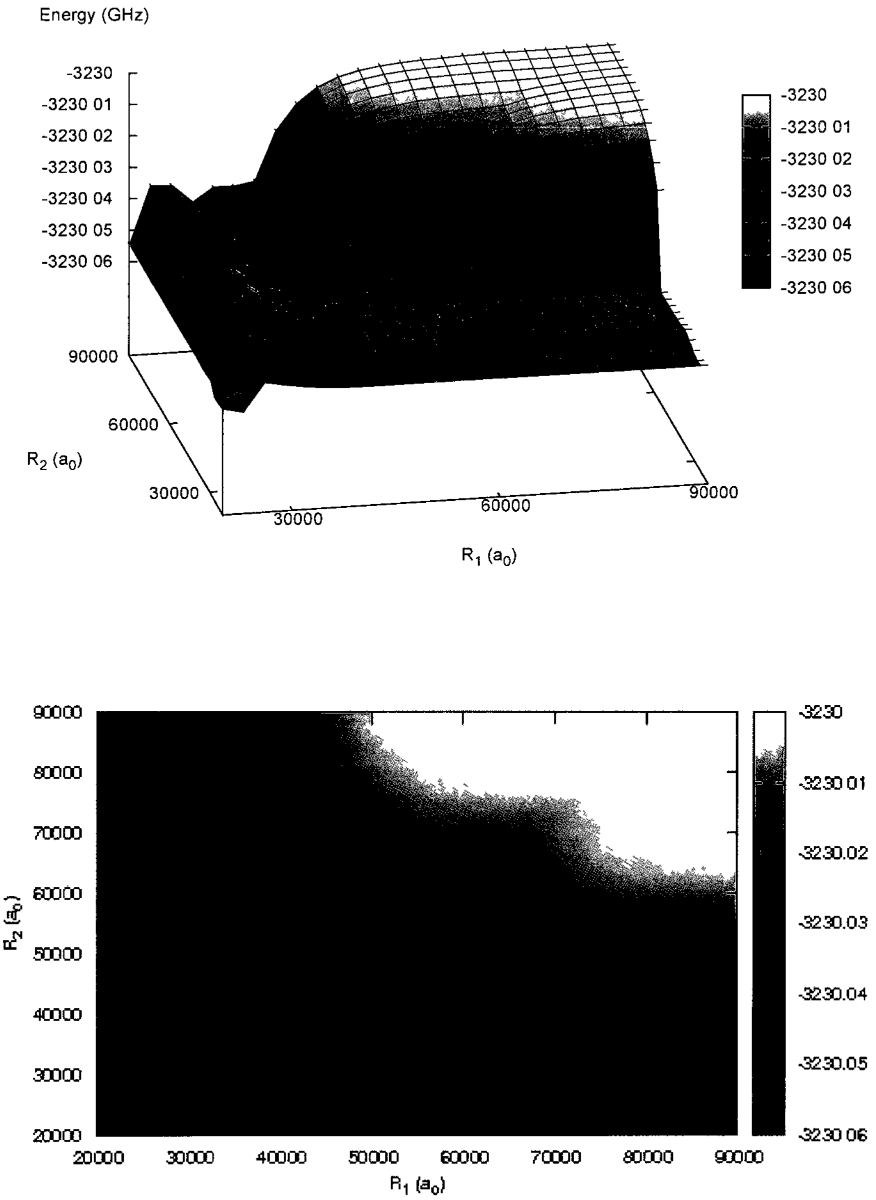

Fig. 5.5: PES (top) and projection (bottom) correlated to the $|58d_{5/2}; 57d_{5/2}; 55d_{3/2}\rangle$ asymptotic state. The surface exhibits many interesting features, including small ripples lying parallel to the R_1-axis and a large ridge lying parallel to the R_2 axis.

analyzing differently symmetrized three-body systems, *i.e.* triangular systems. It will be convenient to consider the case where the third atom lies along the axis that bisects the axis connecting the other two atoms; such a configuration belongs to the C_{2h} point group. To analyze this new physical picture, new asymptotic basis states based on the new symmetry will have to be derived and a new three-body potential will need to be determined. Although the general form of the long-range potential [42] is still true, expressing the potential at a point not along the z-axis (*i.e.* the axis connecting the two base atoms) becomes more complex [39]. It will be interesting to see if an analytical expression similar to Equation (2.3.8) can be found for this off-axis interaction potential. We look forward to pursuing these challenges and believe that the results will prove useful in the progression of ultracold physics and quantum chemistry.

Appendix A

Molecular Curves

In this appendix, we present the potential curves that we calculated which do not exhibit deep, isolated potential wells. The curves correspond to the relevant symmetries of the $70s + 70s$, $70p + 70p$, and $70d + 70d$ asymptotes of the first five alkali elements. Note: The Rb $70s + 70s$, $70p + 70p$ and Cs $70p + 70p$ curves that we focus on throughout this dissertation are not included here.

A.1 Lithium

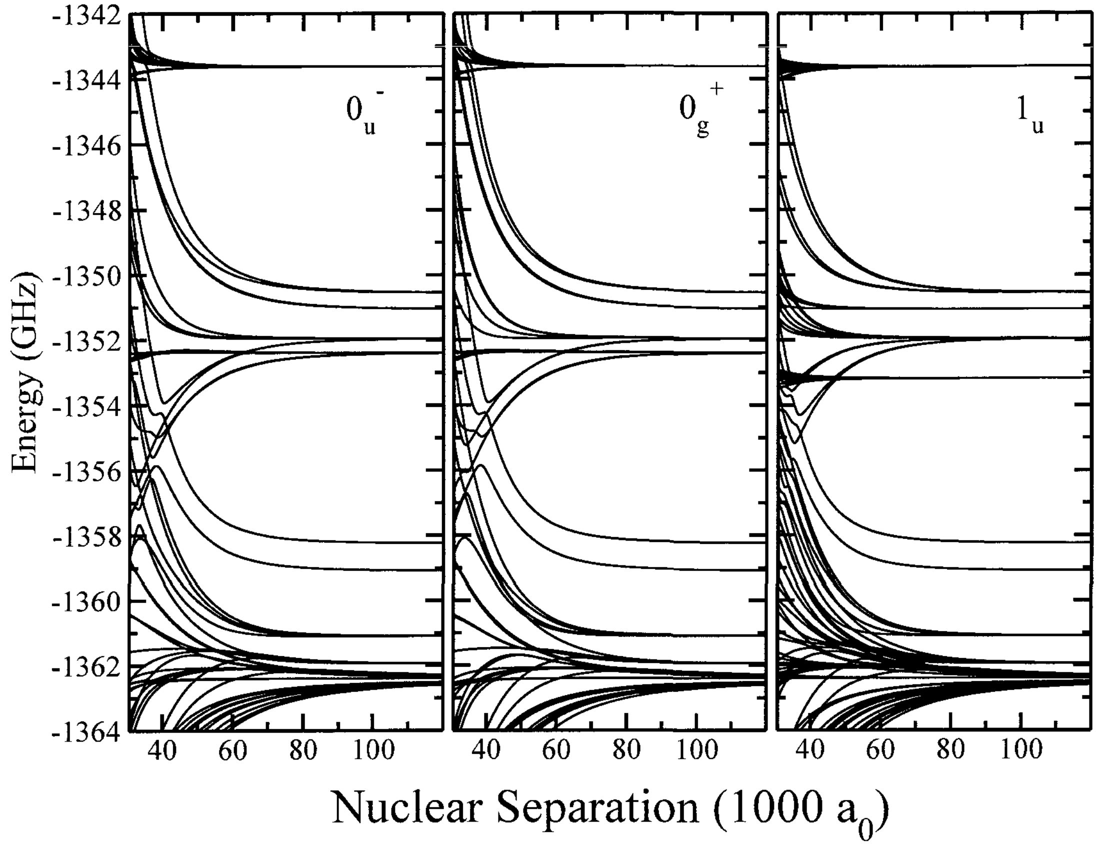

Fig. A.1: Potential energy curves for the 0_u^- (left panel), 0_g^+ (center panel), and 1_u (right panel) symmetries for the doubly-excited *ns* Rydberg state of lithium.

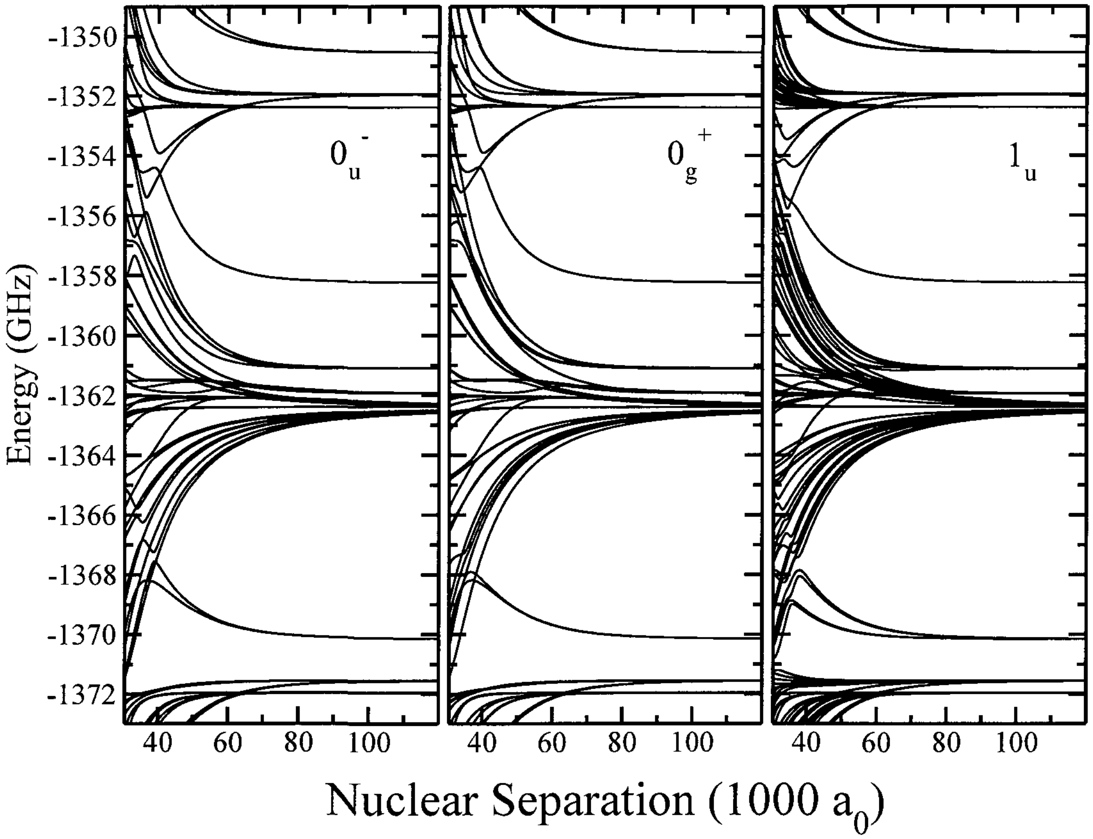

Fig. A.2: Same as Fig. A.1 for the doubly excited *np* Rydberg state of Li.

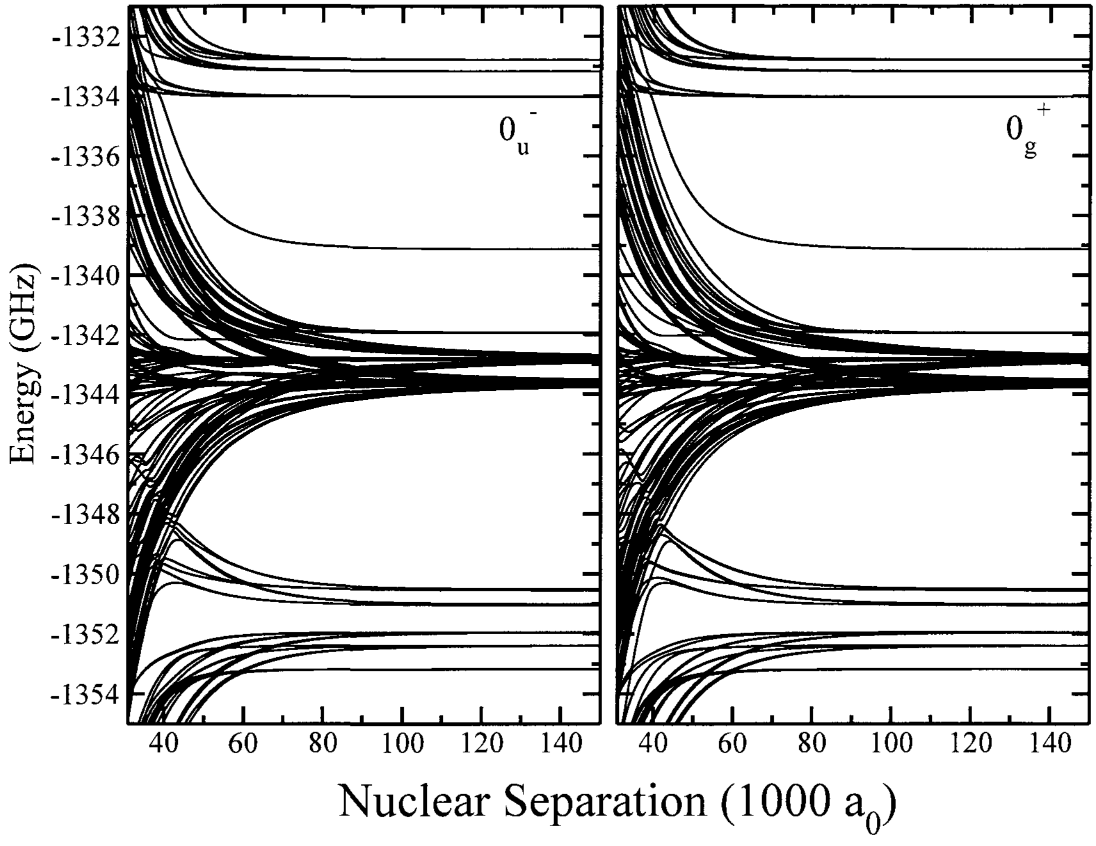

Fig. A.3: Potential energy curves for the 0_u^- (left panel) and 0_g^+ (right panel) symmetries for the doubly-excited *nd* Rydberg state of lithium.

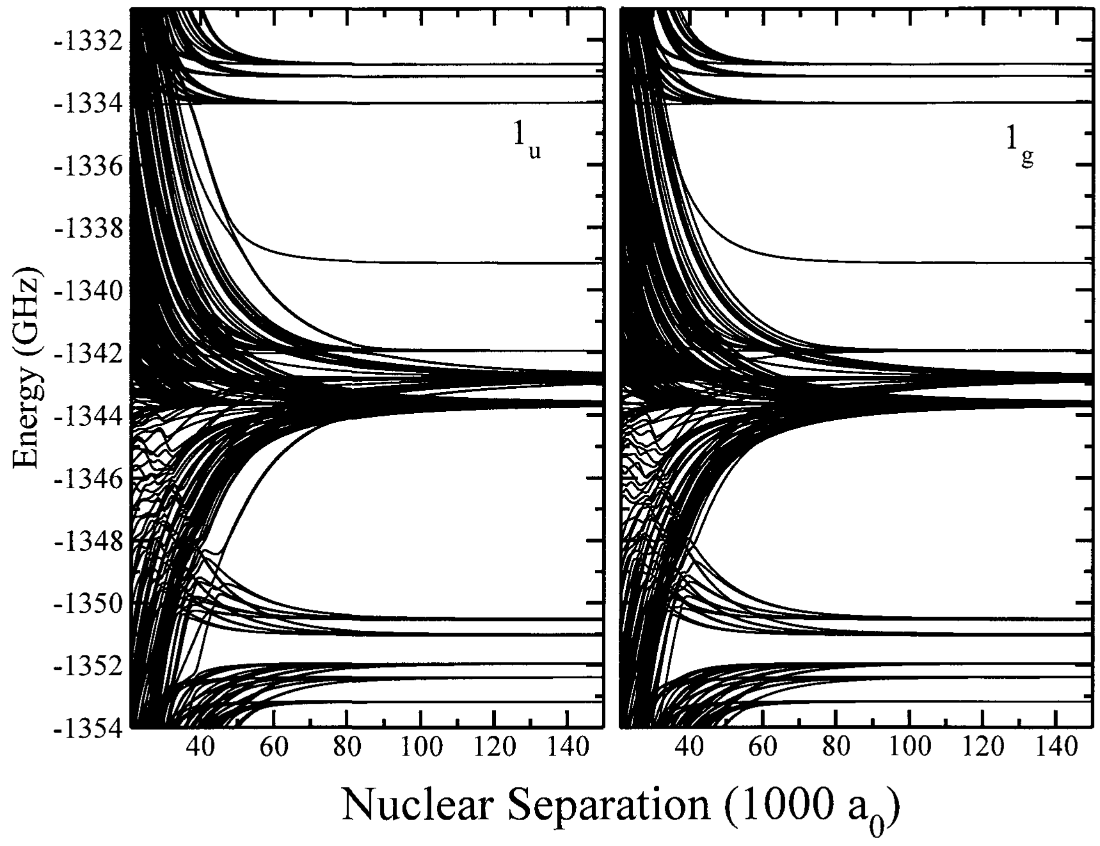

Fig. A.4: Same as Fig. A.3 for the 1_u (left panel) and 1_g (right panel) symmetries of Li.

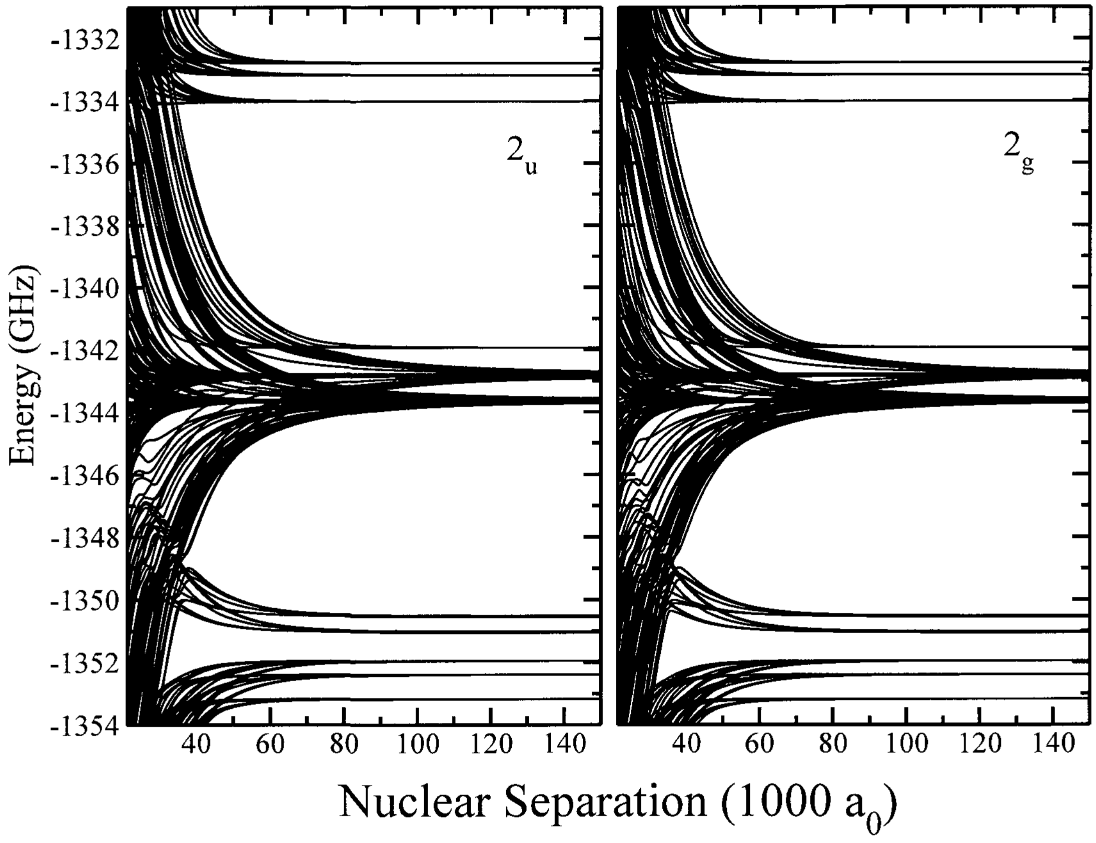

Fig. A.5: Same as Fig. A.3 for the 2_u (left panel) and 2_g (right panel) symmetries of Li.

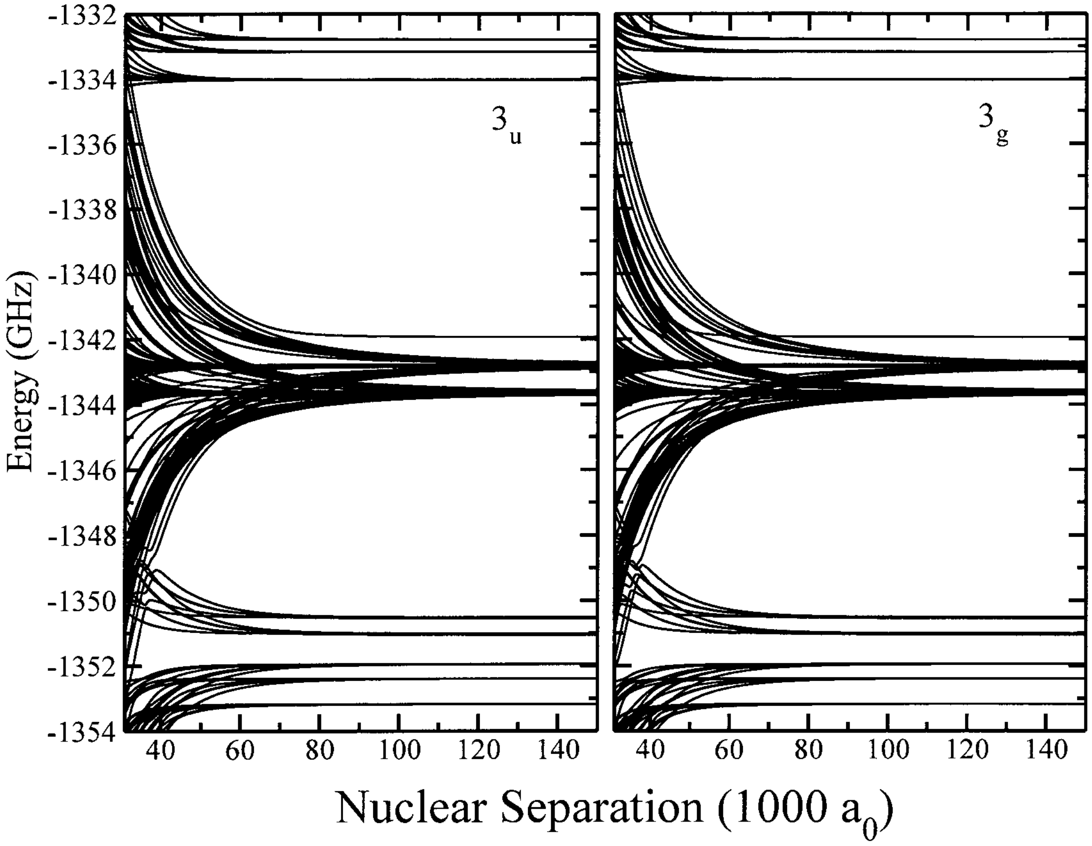

Fig. A.6: Same as Fig. A.3 for the 3_u (left panel) and 3_g (right panel) symmetries of Li.

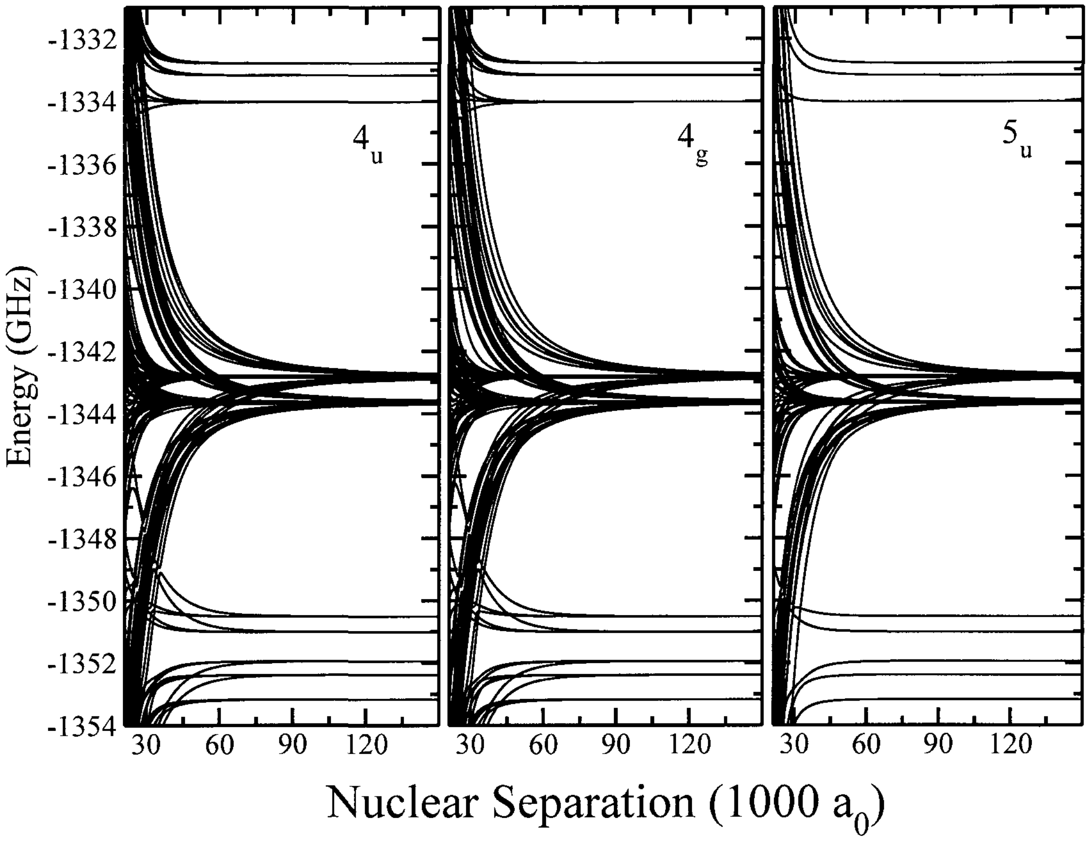

Fig. A.7: Same as Fig. A.3 for the 4_u (left panel) and 4_g (center panel) and 5_u (right panel) symmetries of Li.

A.2 Sodium

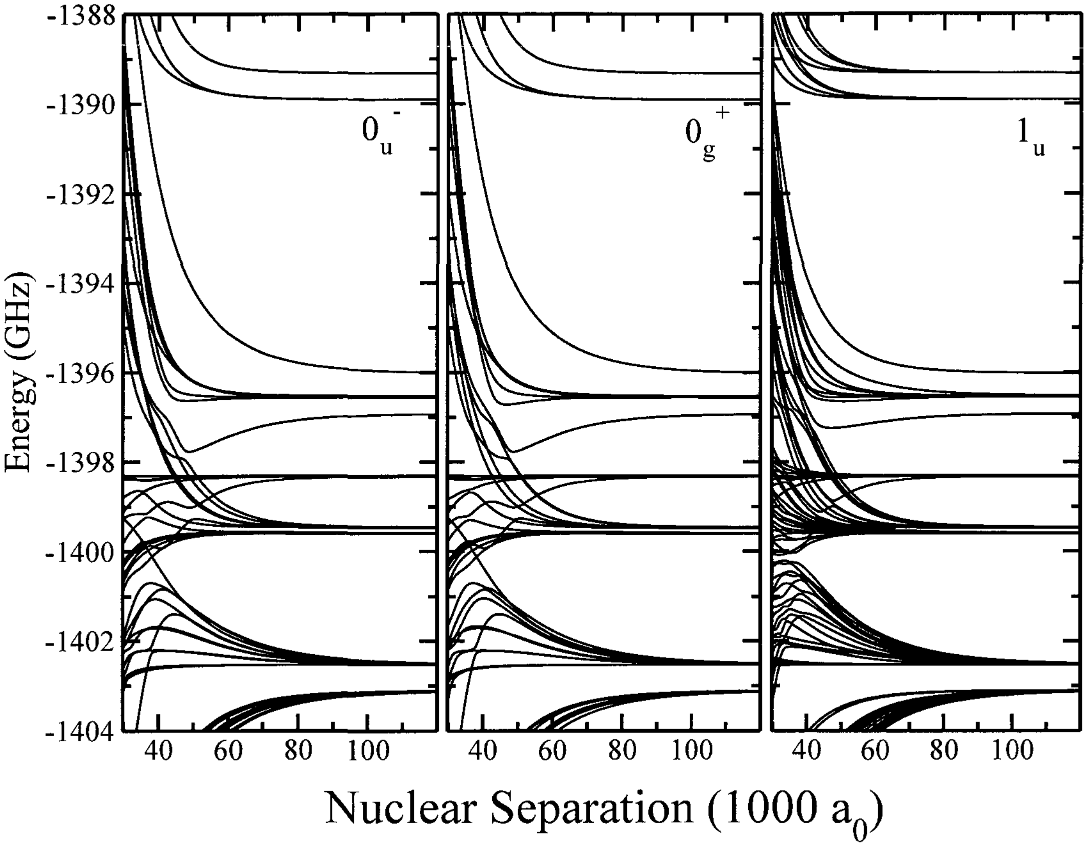

Fig. A.8: Potential energy curves for the 0_u^- (left panel), 0_g^+ (center panel), and 1_u (right panel) symmetries for the doubly-excited *ns* Rydberg state of sodium.

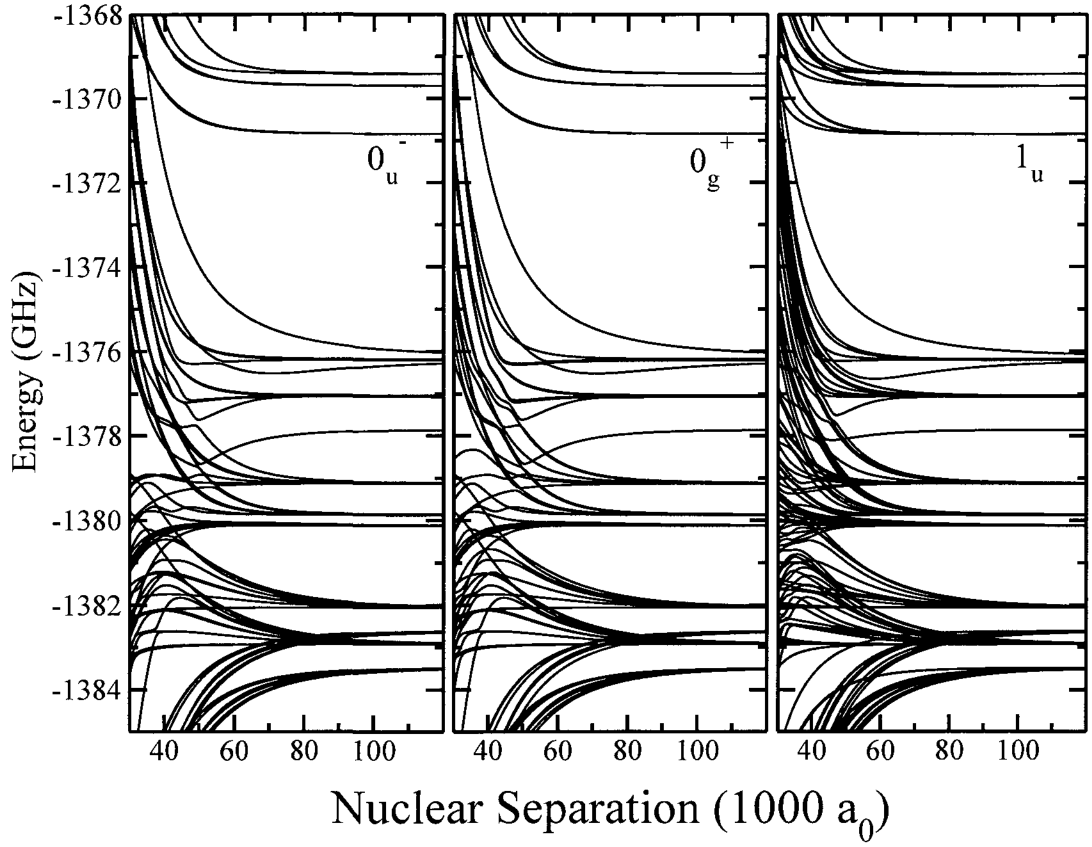

Fig. A.9: Same as Fig. A.8 for the doubly excited *np* Rydberg state of Na.

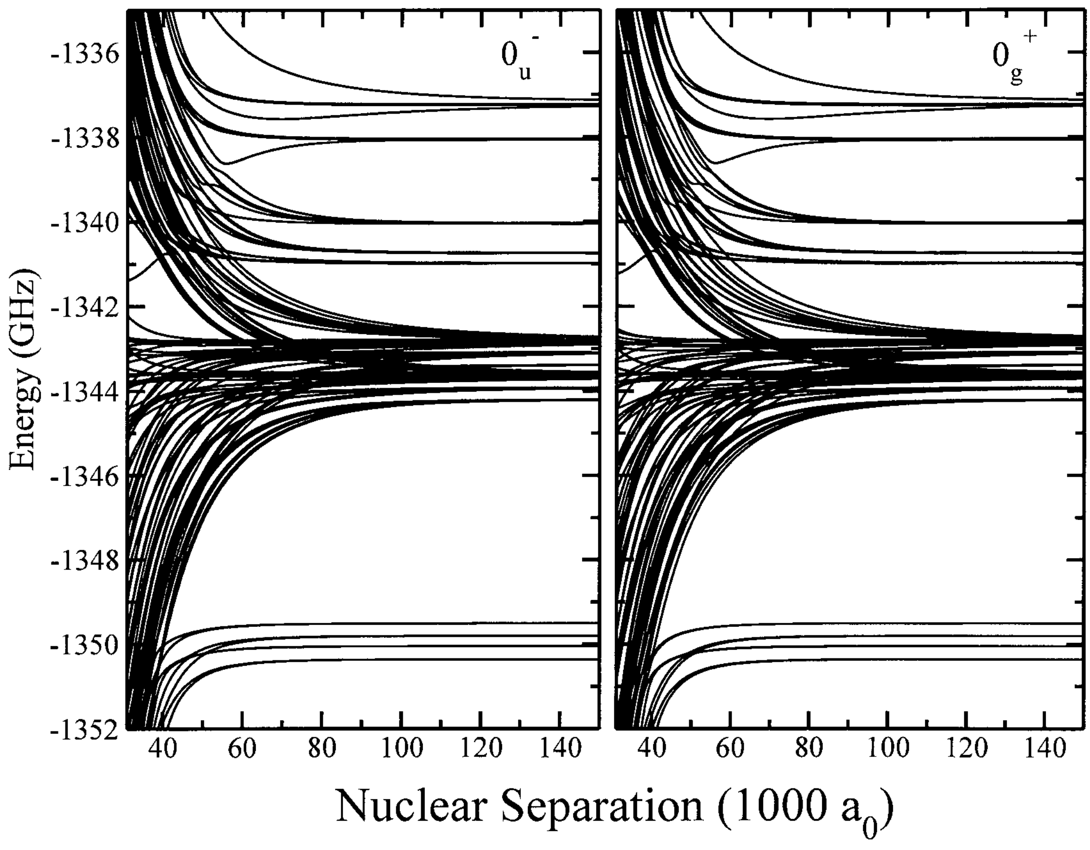

Fig. A.10: Potential energy curves for the 0_u^- (left panel) and 0_g^+ (right panel) symmetries for the doubly-excited *nd* Rydberg state of sodium.

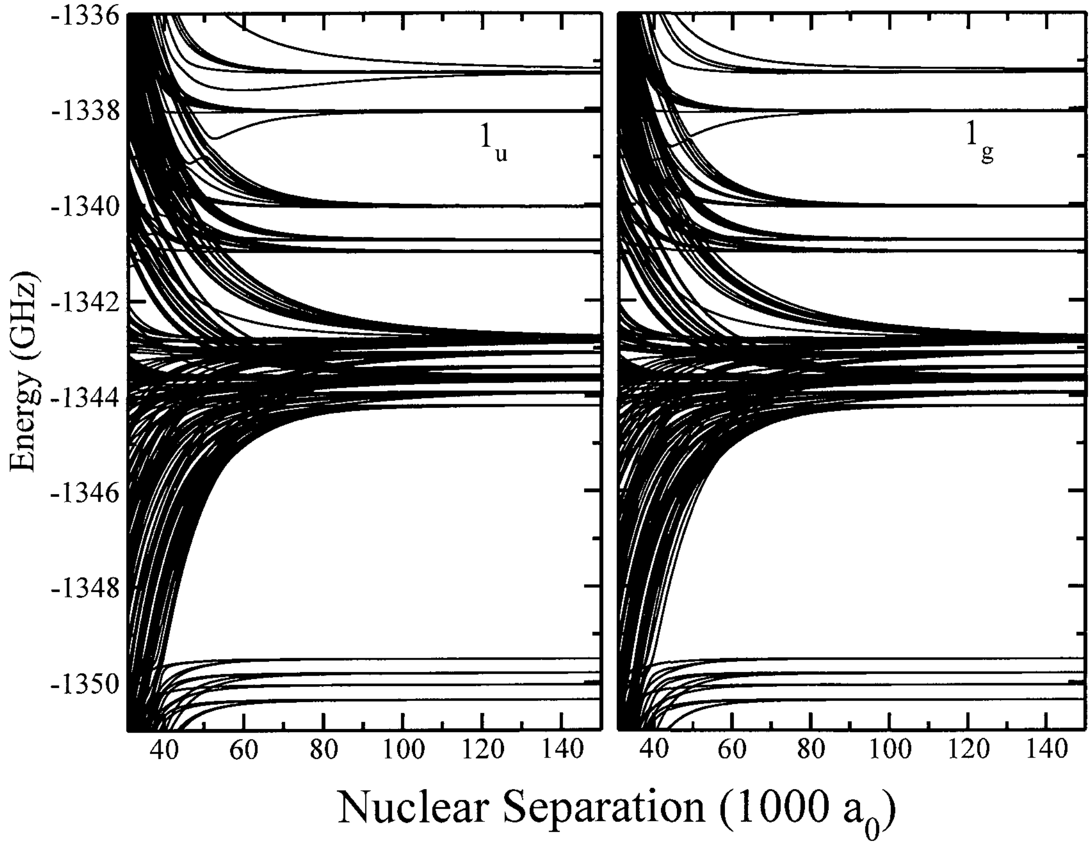

Fig. A.11: Same as Fig. A.10 for the 1_u (left panel) and 1_g (right panel) symmetries of Na.

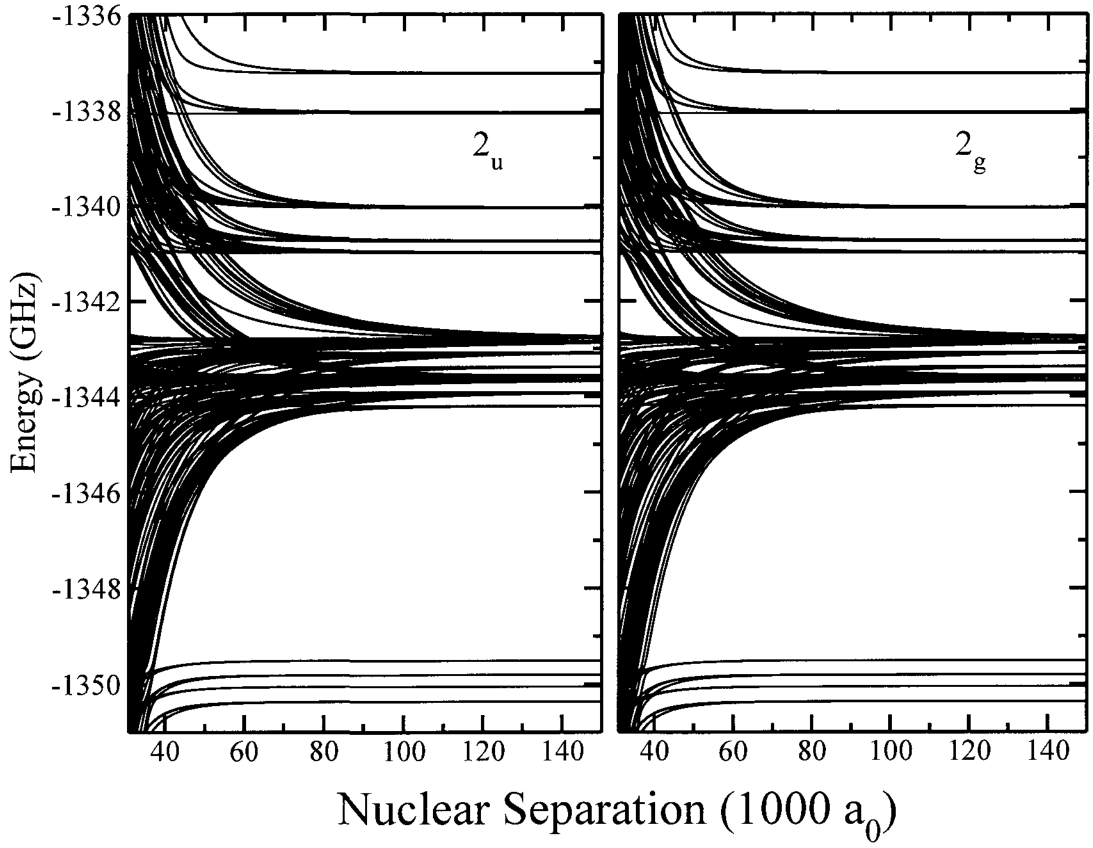

Fig. A.12: Same as Fig. A.10 for the 2_u (left panel) and 2_g (right panel) symmetries of Na.

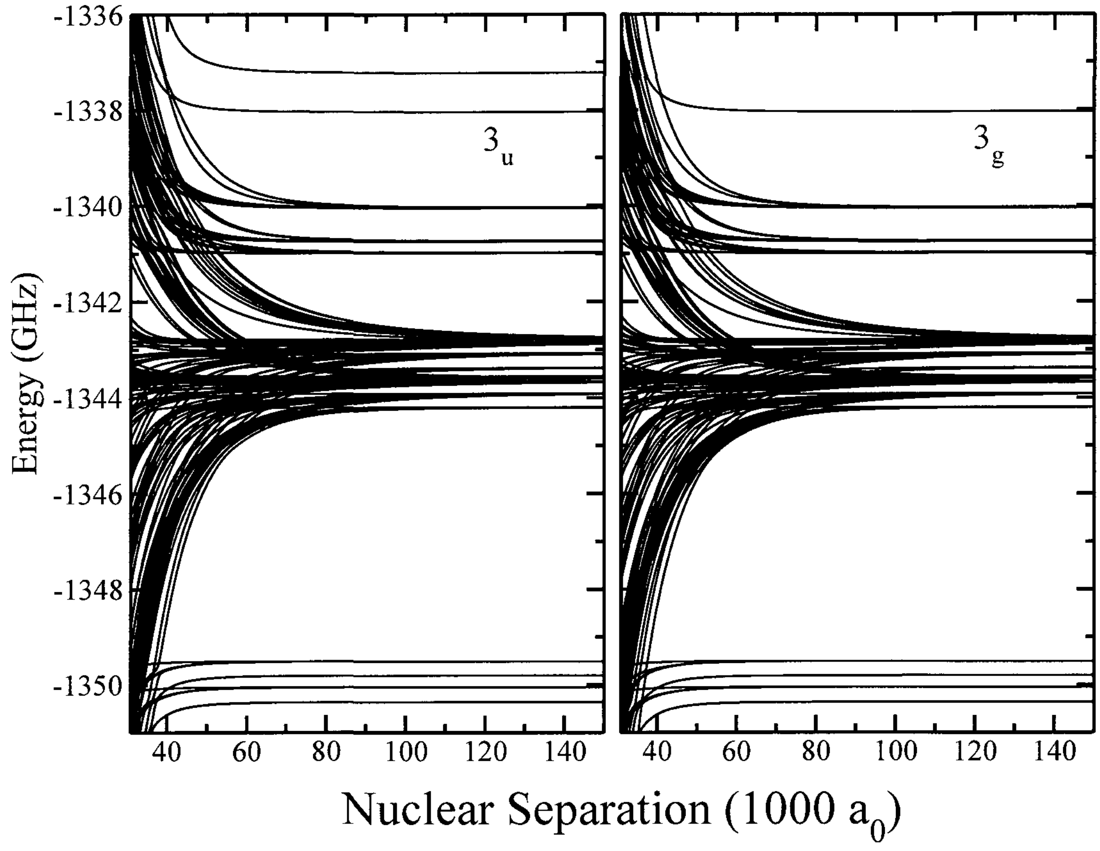

Fig. A.13: Same as Fig. A.10 for the 3_u (left panel) and 3_g (right panel) symmetries of Na.

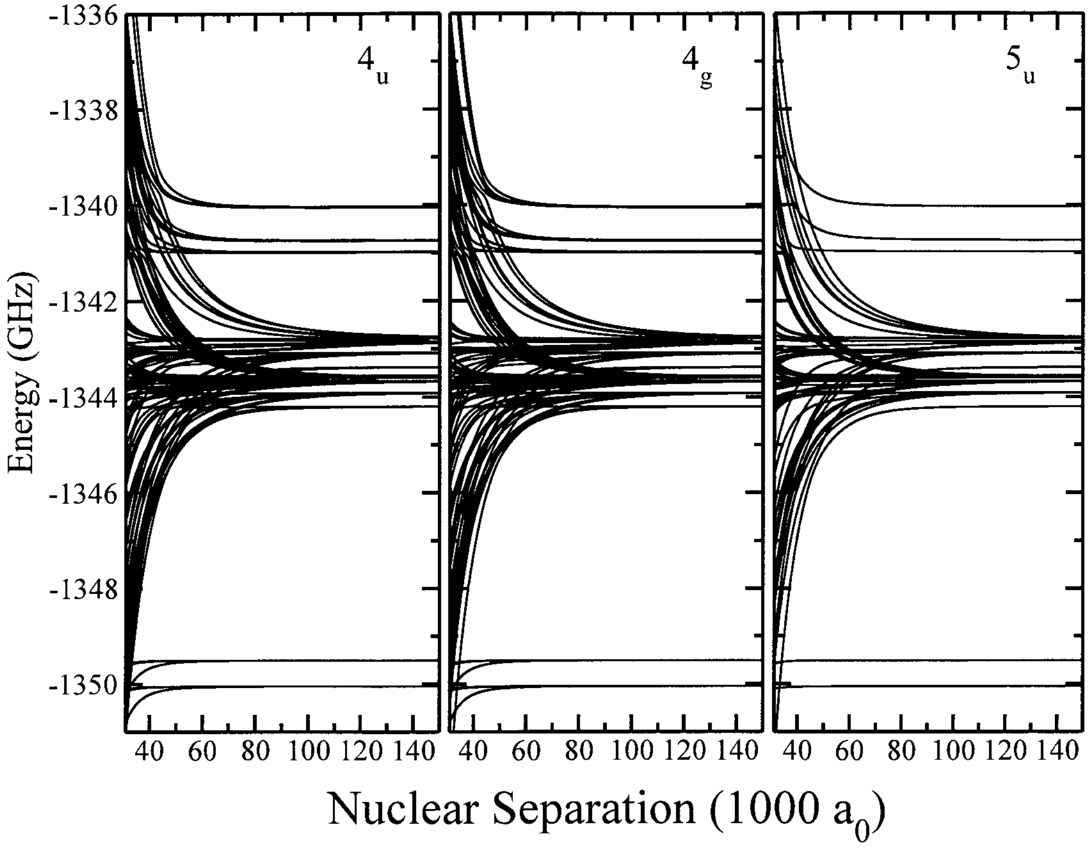

Fig. A.14: Same as Fig. A.10 for the 4_u (left panel), 4_g (center panel) and 5_u (right panel) symmetries of Na.

A.3 Potassium

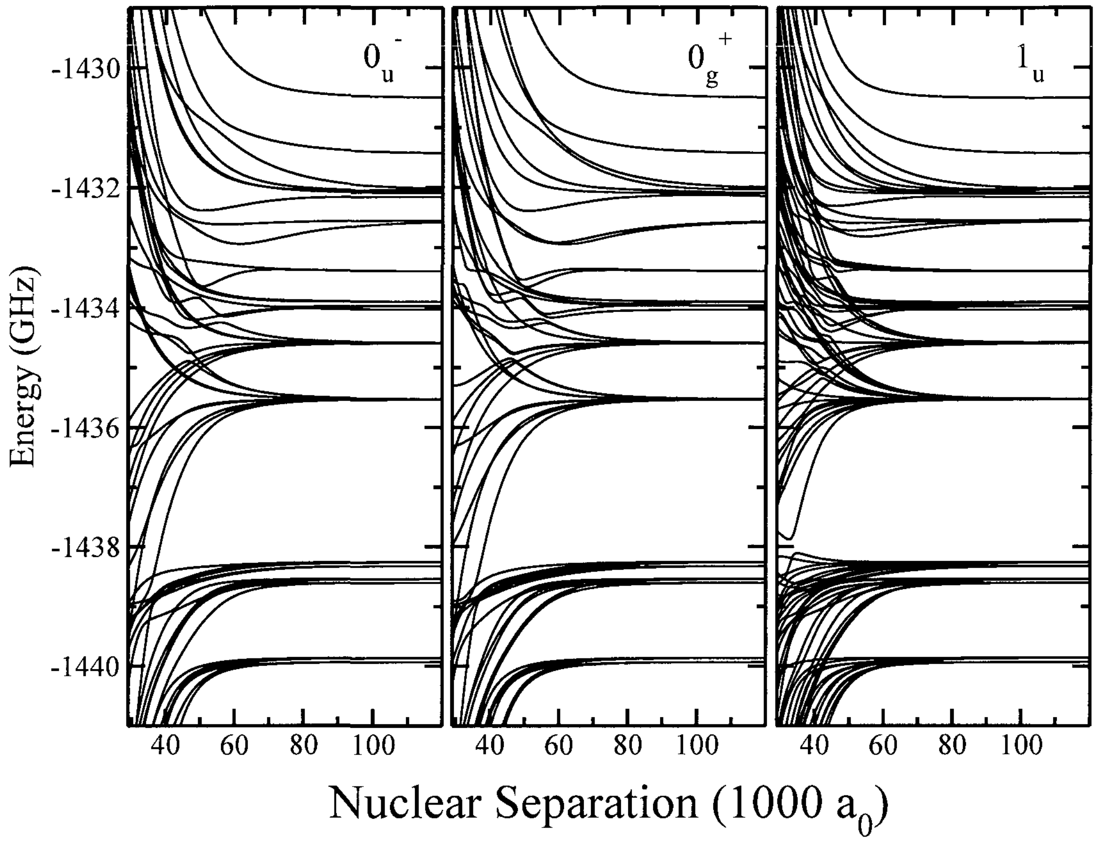

Fig. A.15: Potential energy curves for the 0_u^- (left panel), 0_g^+ (center panel), and 1_u (right panel) symmetries for the doubly-excited ns Rydberg state of potassium.

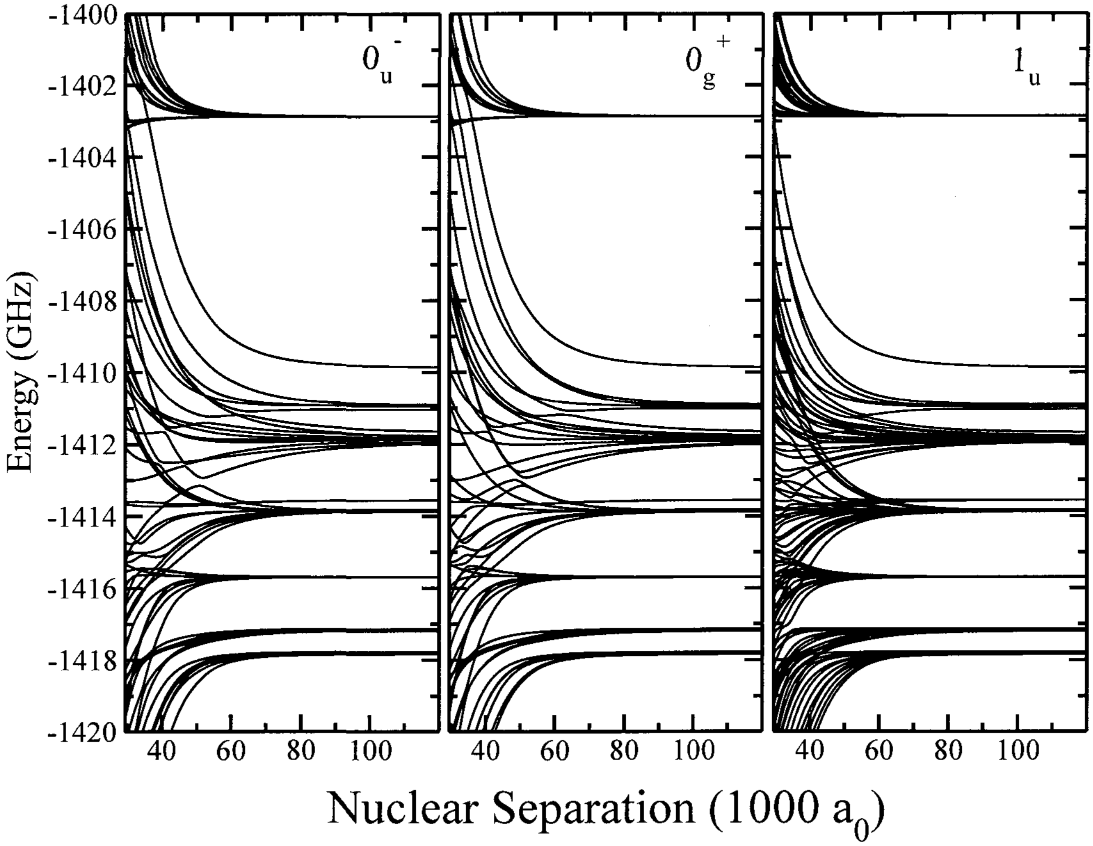

Fig. A.16: Same as Fig. A.15 for the doubly excited *np* Rydberg state of K.

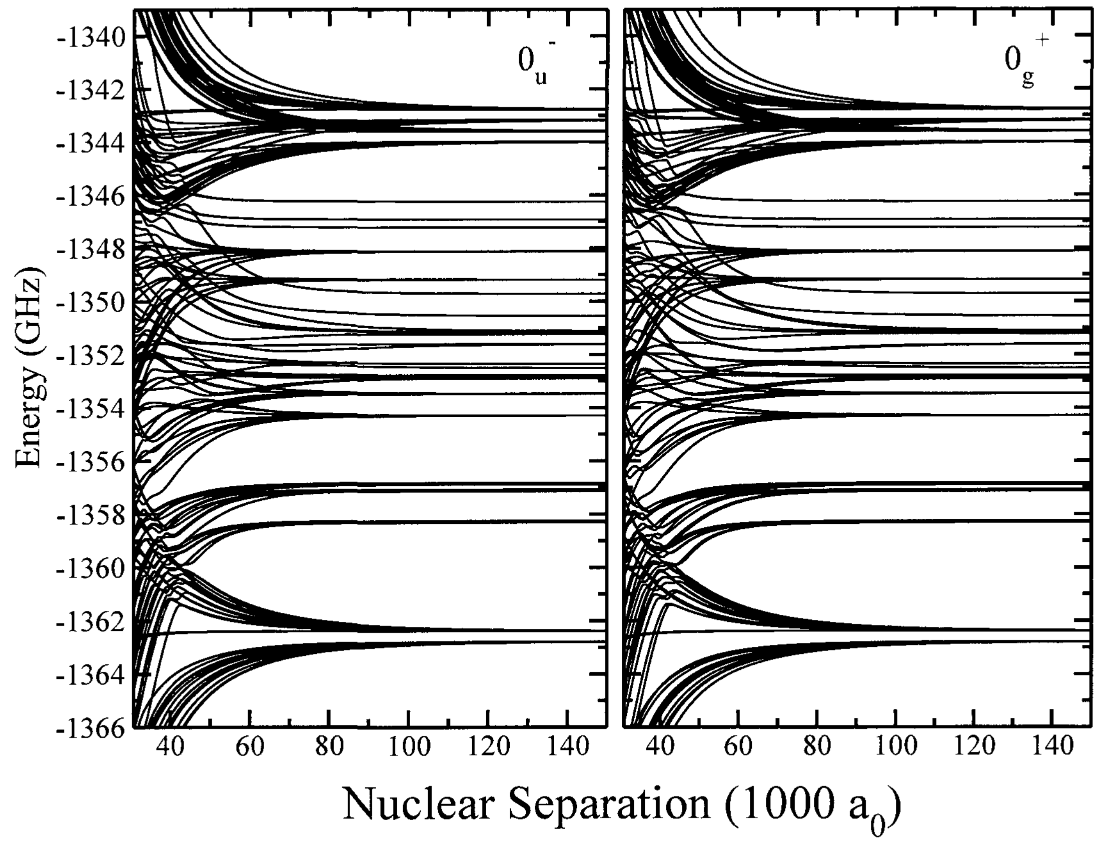

Fig. A.17: Potential energy curves for the 0_u^- (left panel) and 0_g^+ (right panel) symmetries for the doubly-excited *nd* Rydberg state of potassium.

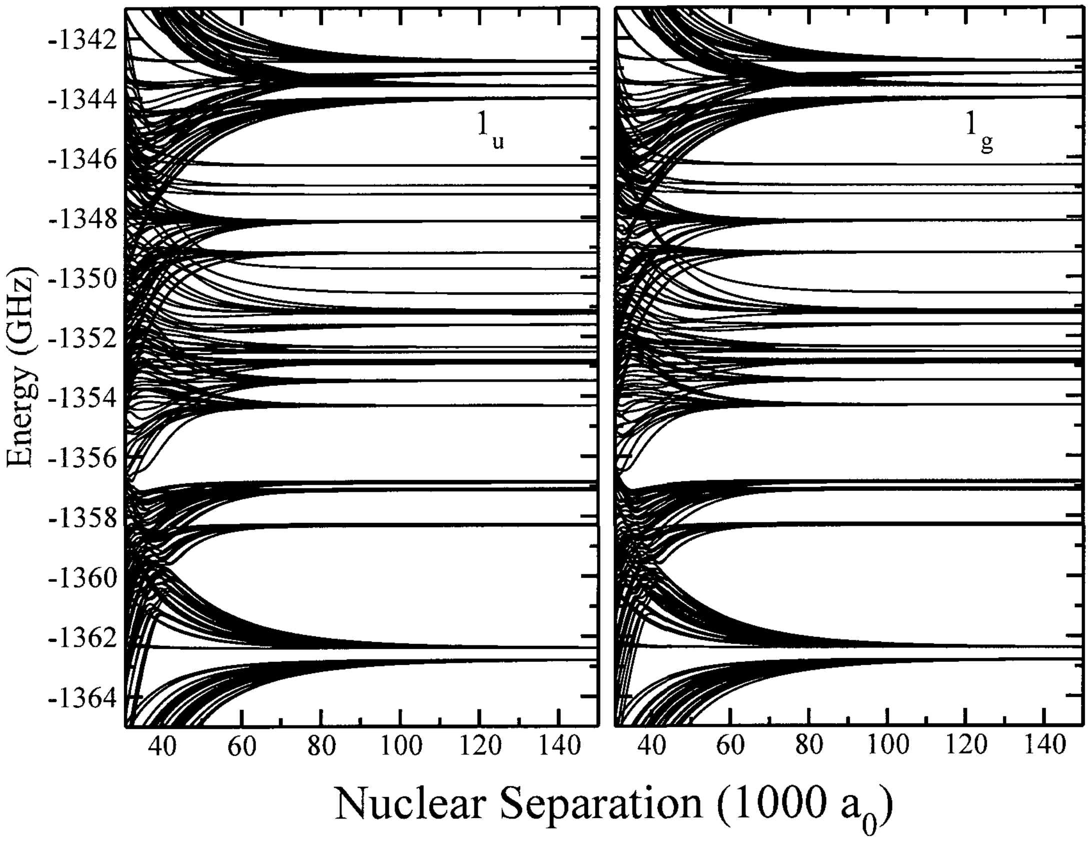

Fig. A.18: Same as Fig. A.17 for the 1_u (left panel) and 1_g (right panel) symmetries of K.

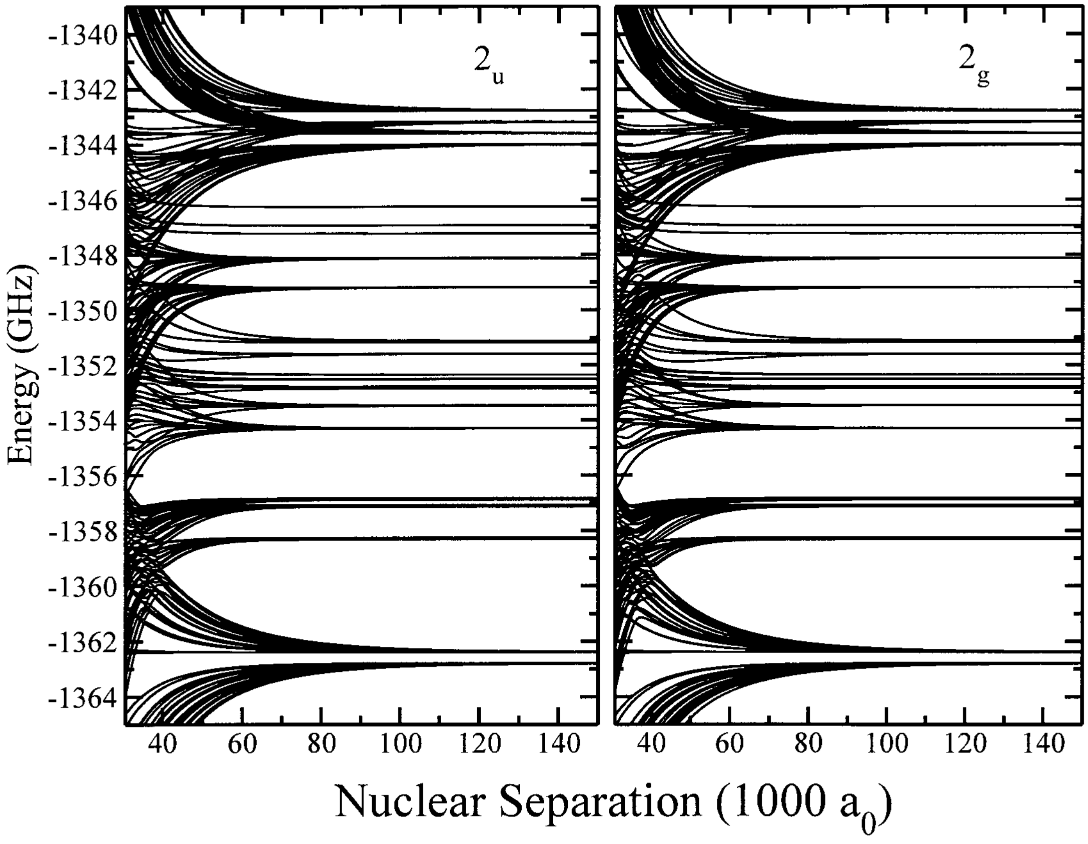

Fig. A.19: Same as Fig. A.17 for the 1_u (left panel) and 1_g (right panel) symmetries of K.

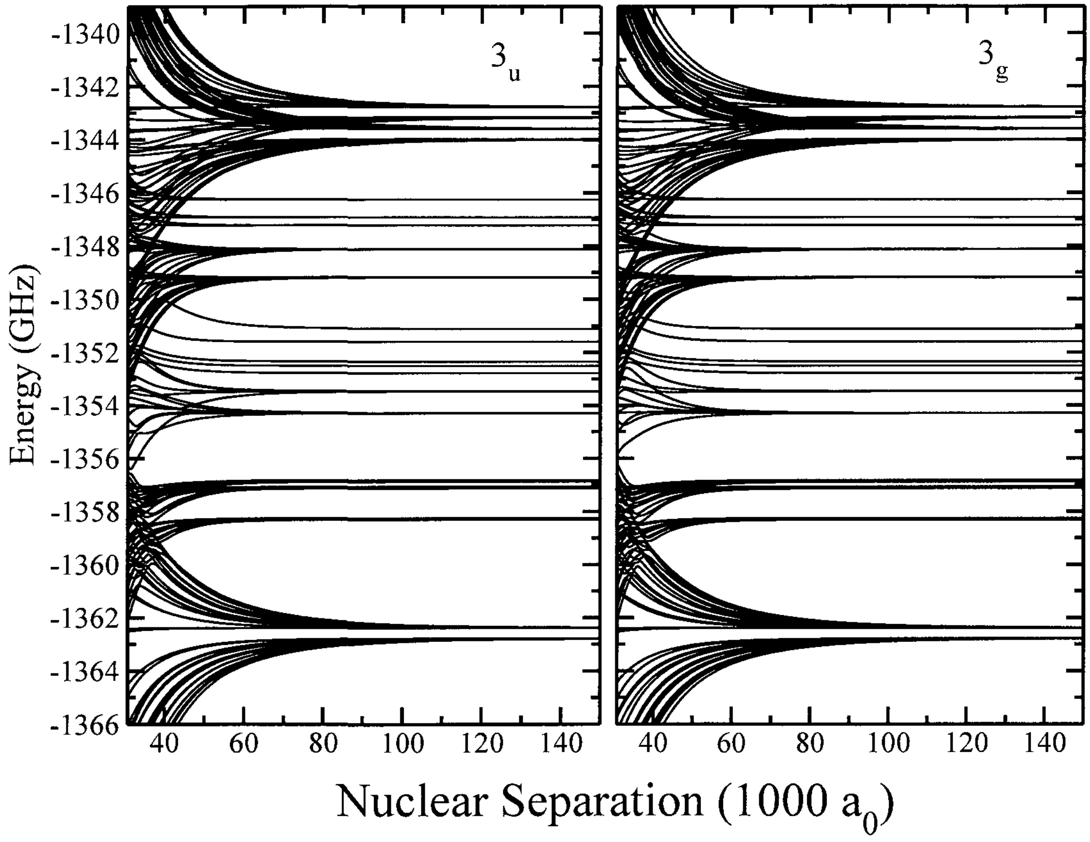

Fig. A.20: Same as Fig. A.17 for the 1_u (left panel) and 1_g (right panel) symmetries of K.

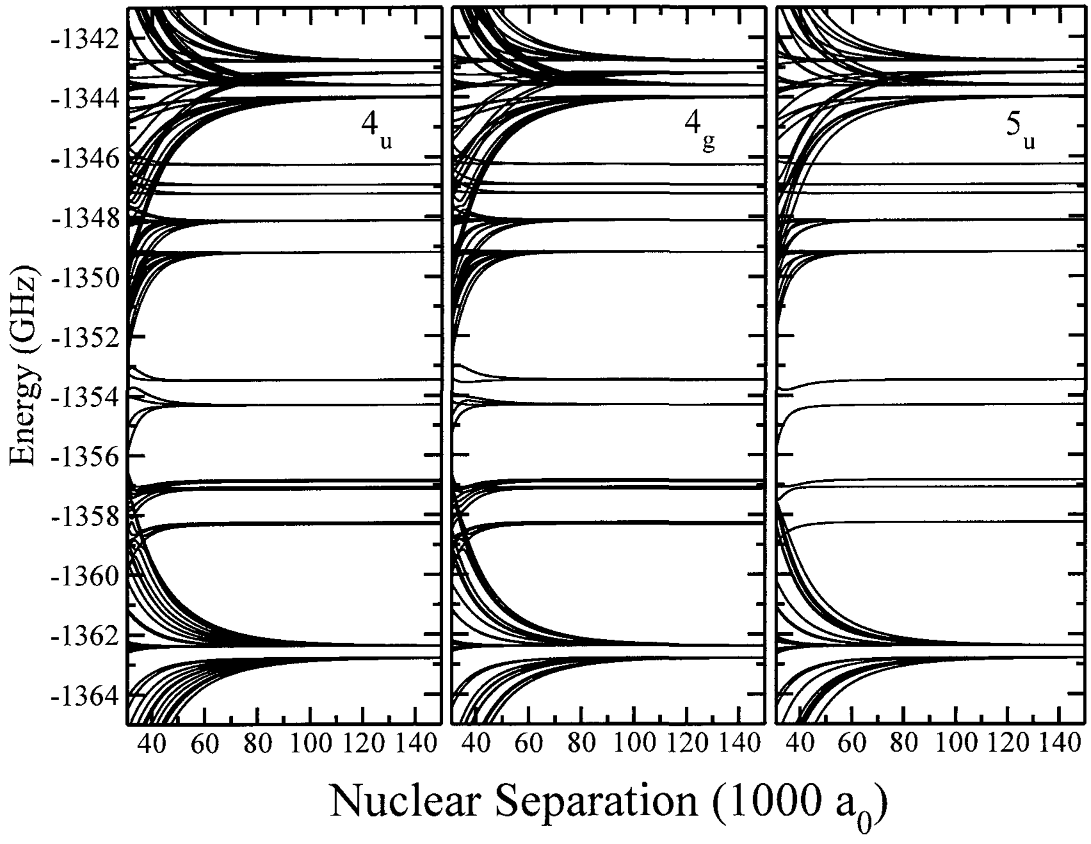

Fig. A.21: Same as Fig. A.17 for the 4_u (left panel), 4_g (center panel), and 5_u (right panel) symmetries of K.

A.4 Rubidium

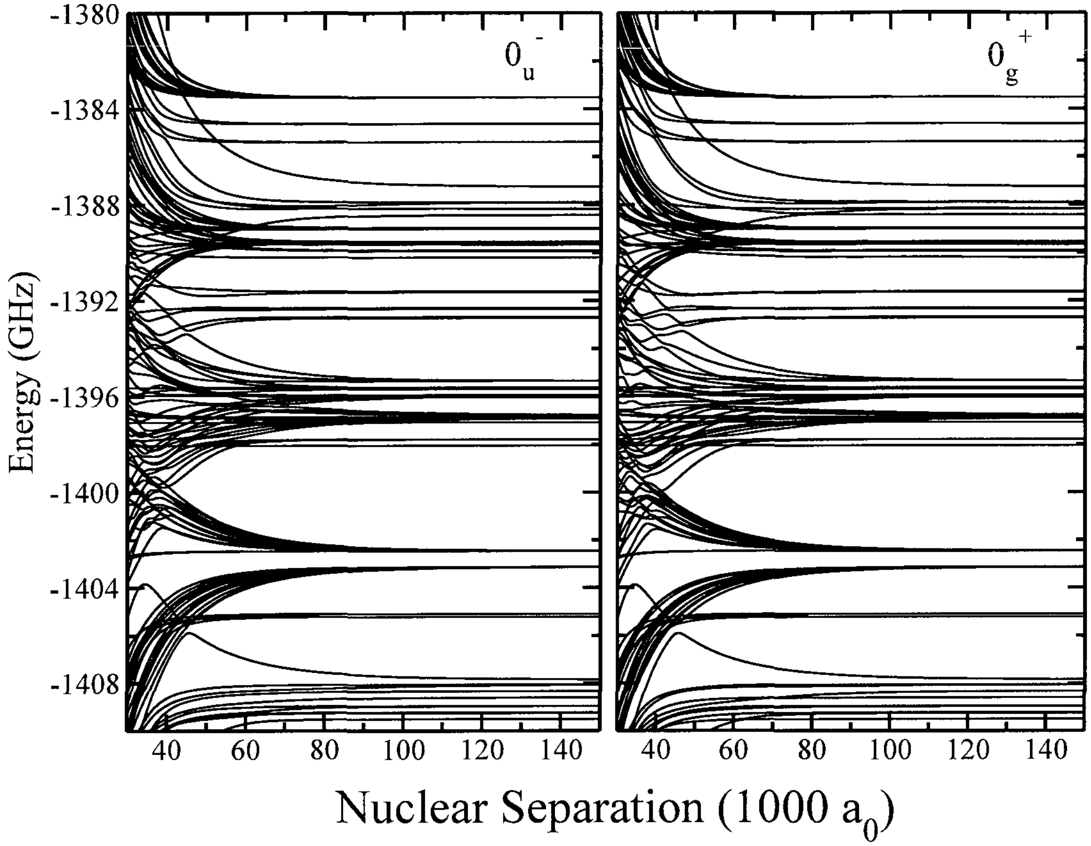

Fig. A.22: Potential energy curves for the 0_u^- (left panel) and 0_g^+ (right panel) symmetries for the doubly-excited *nd* Rydberg state of rubidium.

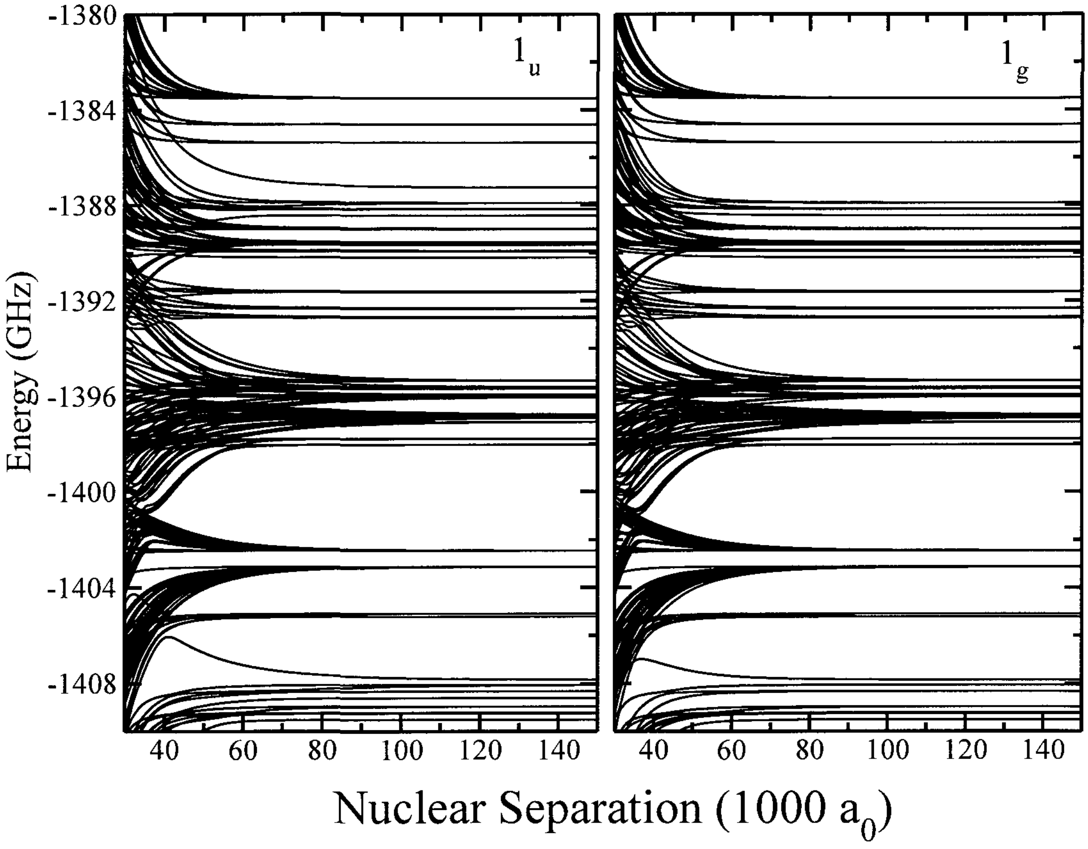

Fig. A.23: Same as Fig. A.22 for the 1_u (left panel) and 1_g (right panel) symmetries of Rb.

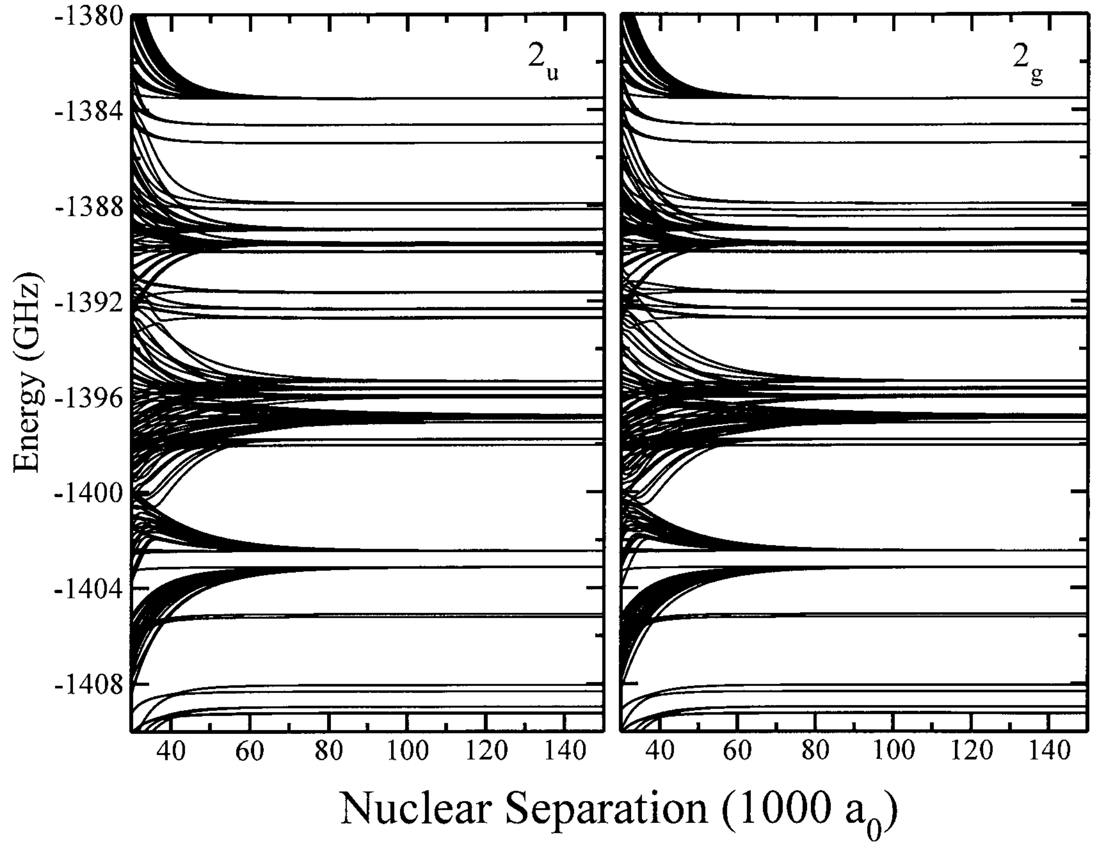

Fig. A.24: Same as Fig. A.22 for the 2_u (left panel) and 2_g (right panel) symmetries of Rb.

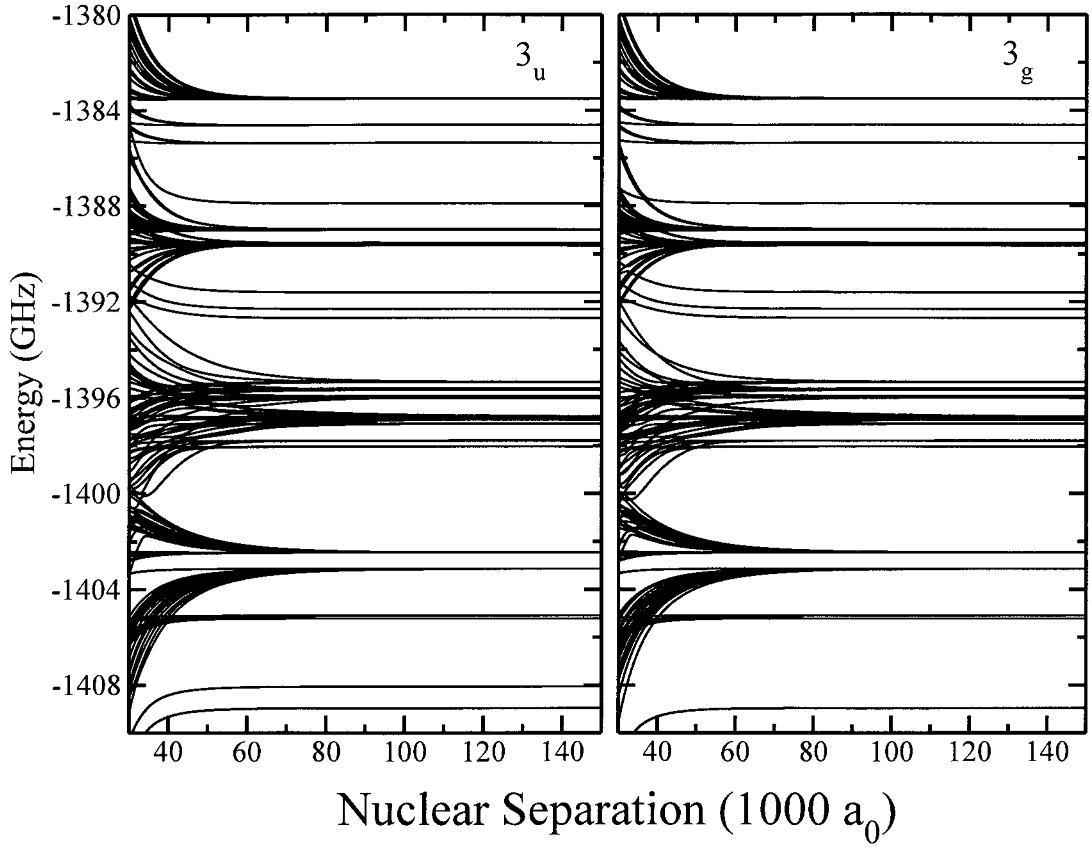

Fig. A.25: Same as Fig. A.22 for the 3_u (left panel) and 3_g (right panel) symmetries of Rb.

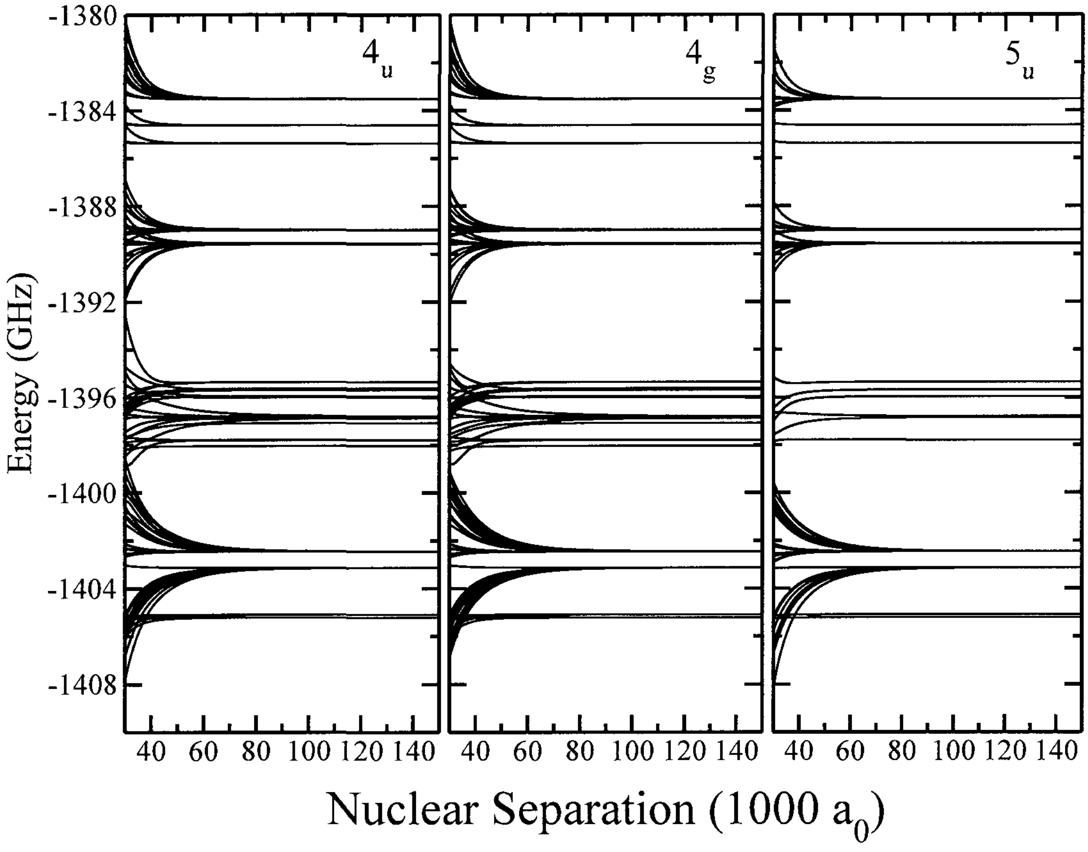

Fig. A.26: Same as Fig. A.22 for the 4_u (left panel), 4_g (center panel), and 5_u (right panel) symmetries of Rb.

A.5 Cesium

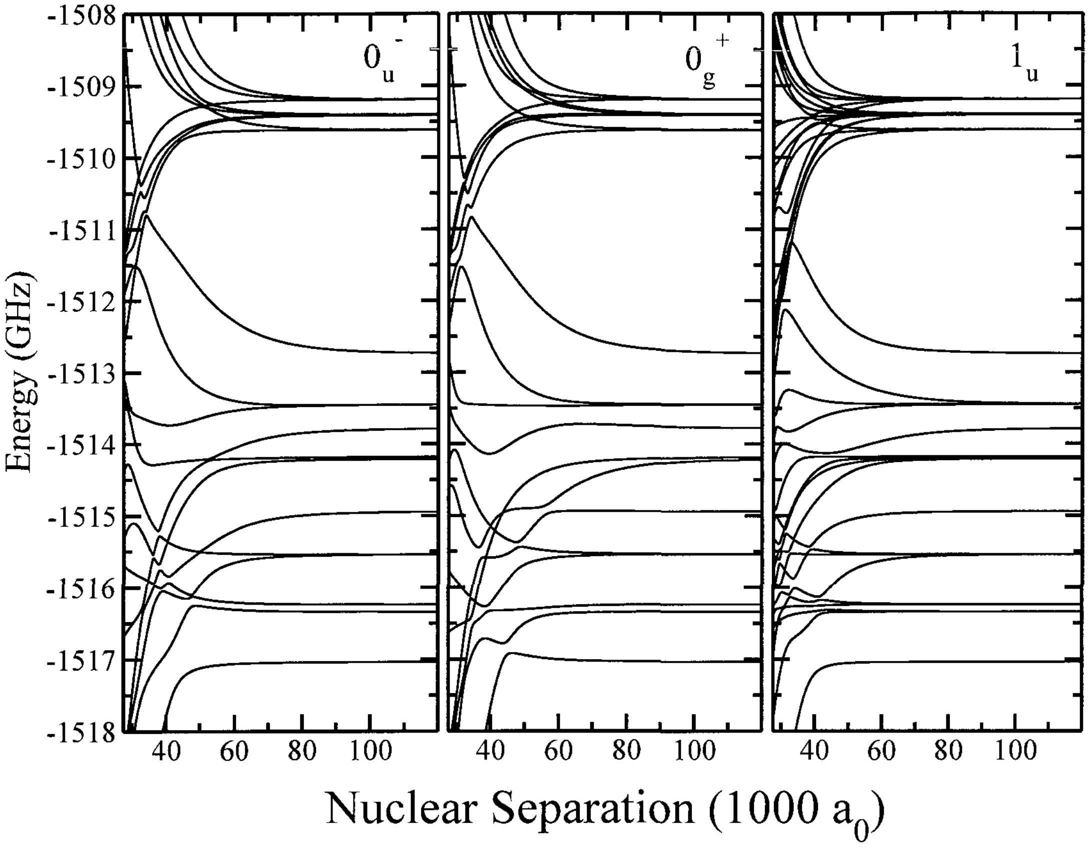

Fig. A.27: Potential energy curves for the 0_u^- (left panel), 0_g^+ (center panel), and 1_u (right panel) symmetries for the doubly-excited *ns* Rydberg state of cesium.

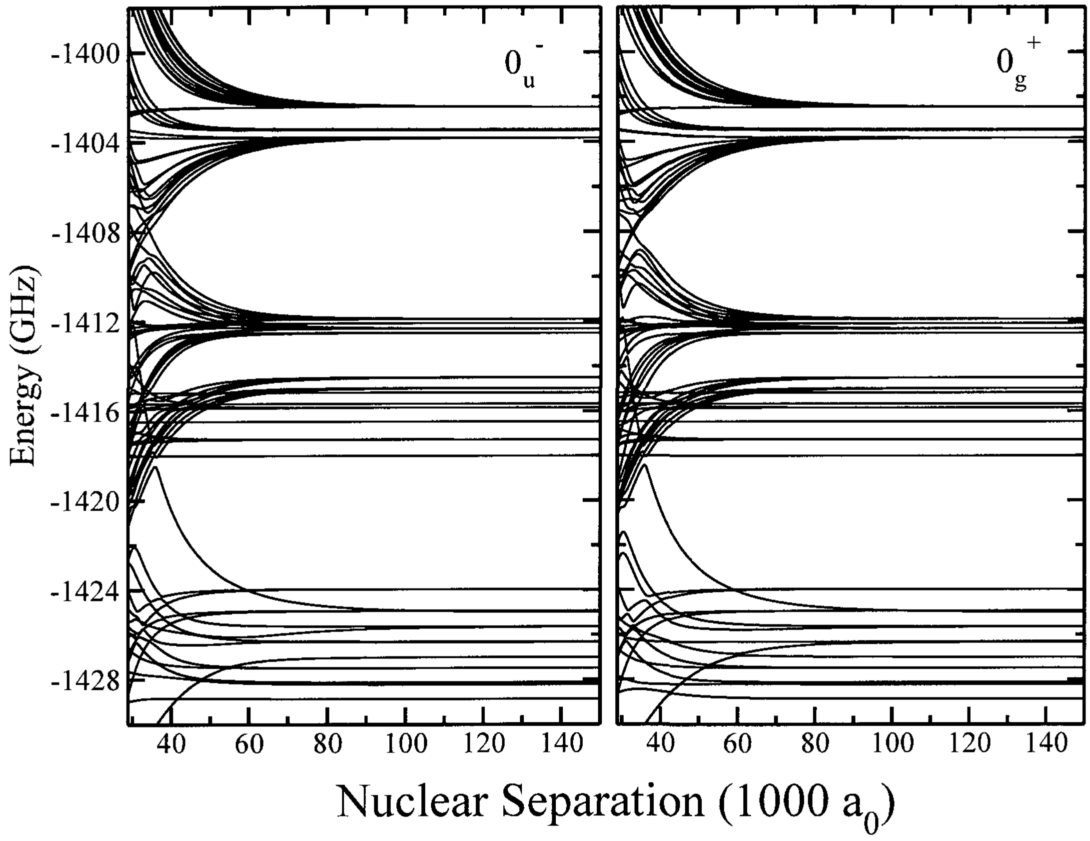

Fig. A.28: Potential energy curves for the 0_u^- (left panel) and 0_g^+ (right panel) symmetries for the doubly-excited *nd* Rydberg state of cesium.

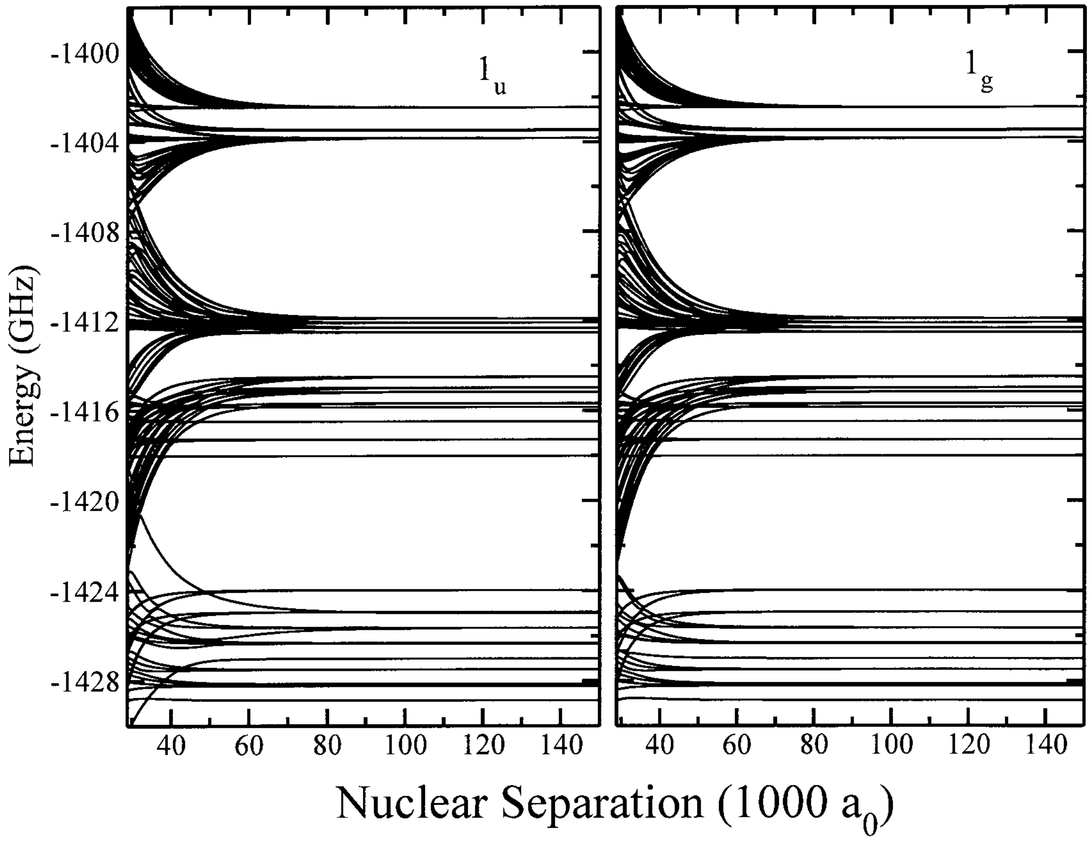

Fig. A.29: Same as Fig. A.28 for the 1_u (left panel) and 1_g (right panel) symmetries of Cs.

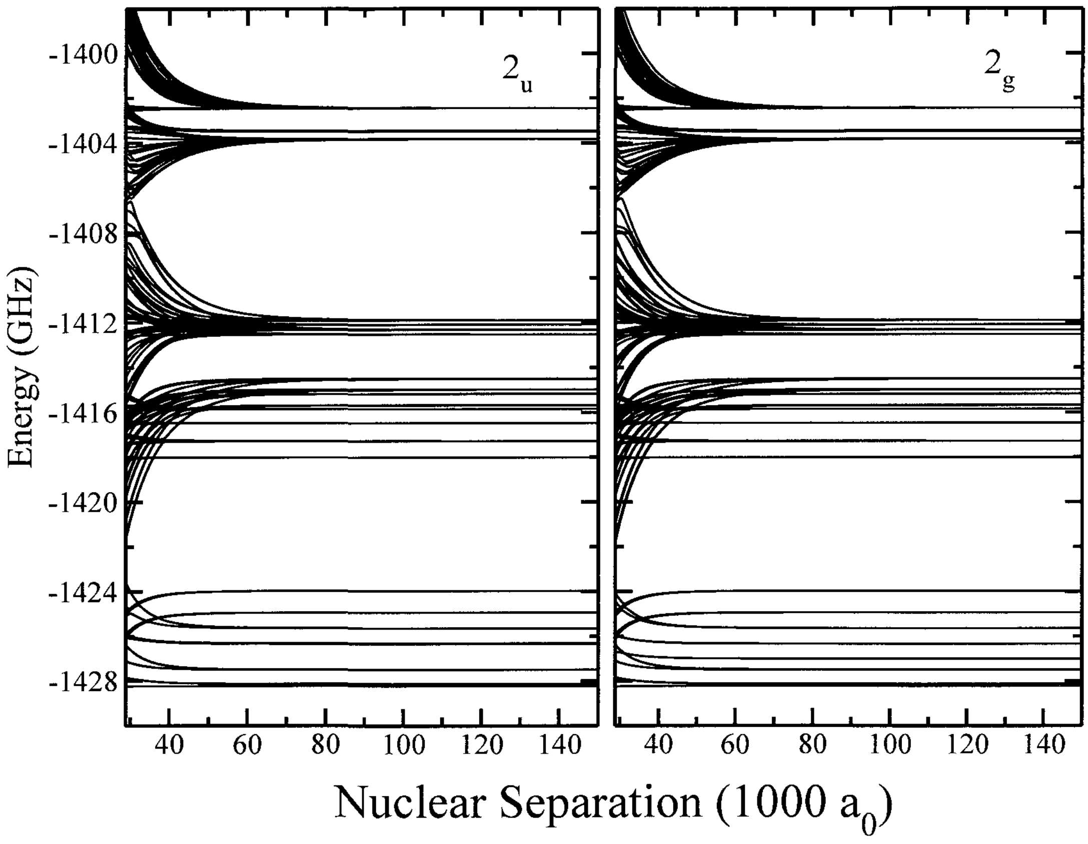

Fig. A.30: Same as Fig. A.28 for the 2_u (left panel) and 2_g (right panel) symmetries of Cs.

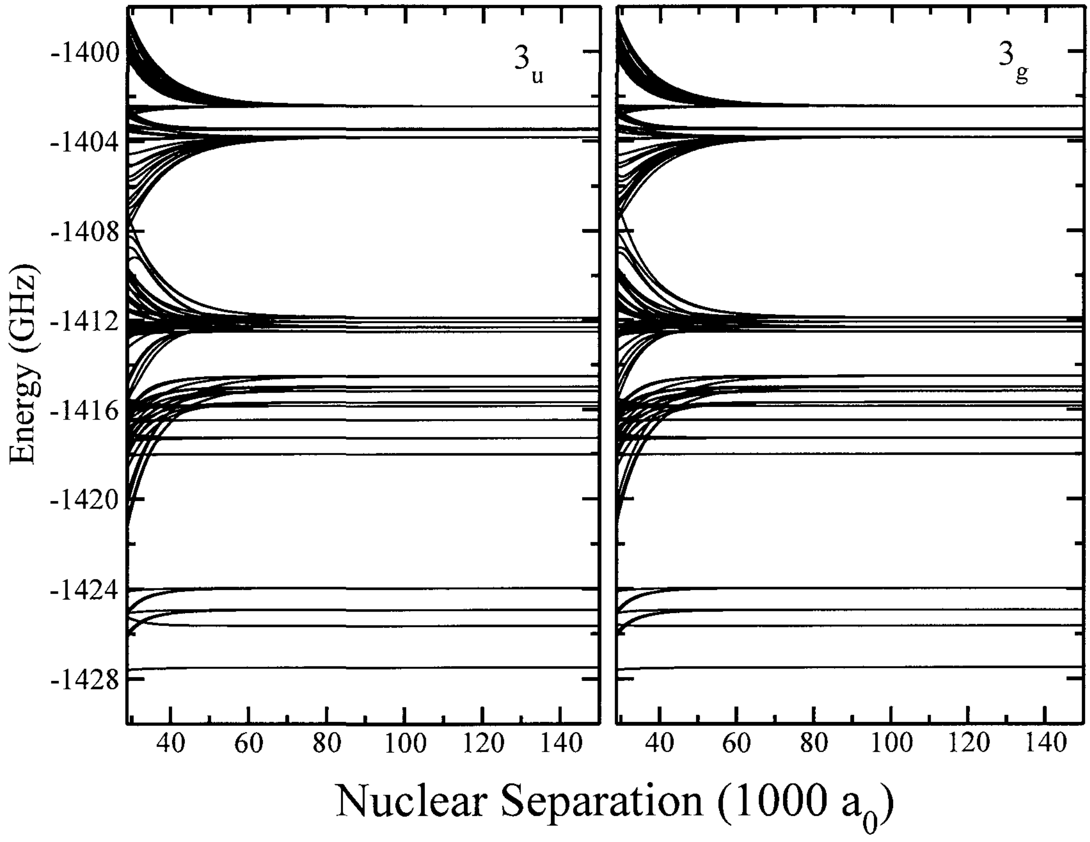

Fig. A.31: Same as Fig. A.28 for the 3_u (left panel) and 3_g (right panel) symmetries of Cs.

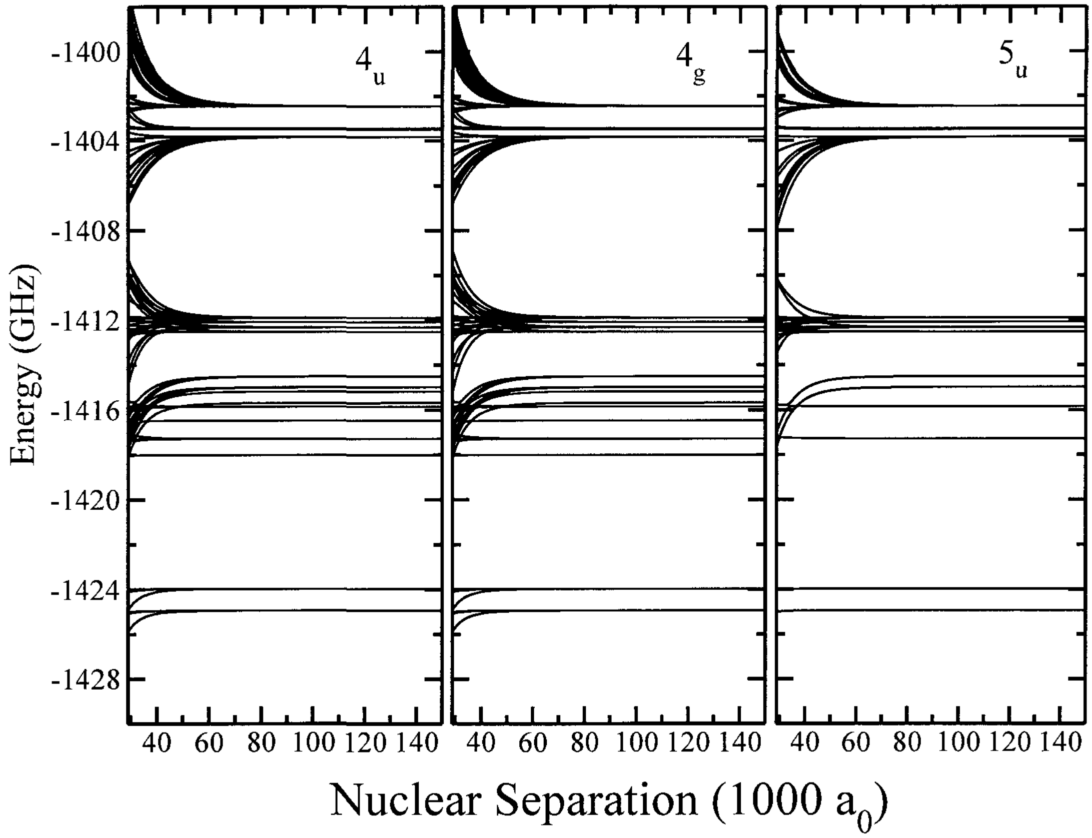

Fig. A.32: Same as Fig. A.28 for the 4_u (left panel), 4_g (right panel), and 5_u symmetries of Cs.

Appendix B

Derivations

B.1 Asymptotic form of the molecular Rydberg states in Hund's case (c)

B.1.1 Two-body

As has been discussed, the spacing of degenerate energy levels due to atomic fine-structure splitting is comparable to the energy separations between local $n\ell + n\ell'$ asymptotes near the doubly excited Rydberg states that we consider. This means that fine structure cannot be ignored and the asymptotic basis states should be built in the Hund's case (c). In this basis, the good quantum number is the projection Ω of the electron's total angular momentum $\vec{j}_{\text{tot}} = \vec{j}_1 + \vec{j}_2$. We construct the asymptotic basis states from atomic wave functions given by $\phi_i^k(\mathbf{r}_q)$, where $i \equiv n_i \ell_i j_i m_{j_i}$ is the quantum state describing electron q associated with atom k.

Given two nuclei, A and B and two electrons, 1 and 2, the general asymptotic form of the electronic wave function is given by:

$$\begin{aligned} \Psi &= C_1 \phi_1^A(\mathbf{r}_1)\phi_2^B(\mathbf{r}_2) + C_2 \phi_1^B(\mathbf{r}_1)\phi_2^A(\mathbf{r}_2) \\ &+ C_3 \phi_2^A(\mathbf{r}_1)\phi_1^B(\mathbf{r}_2) + C_4 \phi_2^B(\mathbf{r}_1)\phi_1^A(\mathbf{r}_2) \; . \end{aligned} \qquad \text{(B.1.1)}$$

Under the exchange of the two electrons, the total wave function Ψ must be antisymmetric, *i.e.* $\hat{P}_{12}\Psi = -\Psi$. Thus,

$$\begin{aligned} \hat{P}_{12}\Psi = -\Psi &= C_1\phi_1^A(\mathbf{r}_2)\phi_2^B(\mathbf{r}_1) + C_2\phi_1^B(\mathbf{r}_2)\phi_2^A(\mathbf{r}_1) \\ &+ C_3\phi_2^A(\mathbf{r}_2)\phi_1^B(\mathbf{r}_1) + C_4\phi_2^B(\mathbf{r}_2)\phi_1^A(\mathbf{r}_1) \ . \end{aligned} \tag{B.1.2}$$

Comparing equations B.1.1 and B.1.2, we find:

$$C_1 = -C_4$$

$$C_2 = -C_3$$

and so equation B.1.1 becomes:

$$\begin{aligned} \Psi &= C_1\left[\phi_1^A(\mathbf{r}_1)\phi_2^B(\mathbf{r}_2) - \phi_2^B(\mathbf{r}_1)\phi_1^A(\mathbf{r}_2)\right] \\ &+ C_2\left[\phi_1^B(\mathbf{r}_1)\phi_2^A(\mathbf{r}_2) - \phi_2^A(\mathbf{r}_1)\phi_1^B(\mathbf{r}_2)\right] \ . \end{aligned} \tag{B.1.3}$$

The wave function is further symmetrized by the inversion operator $\hat{\imath}$, which acts to exchange each electron with the other's atomic core while inverting the coordinates, *i.e.*

$$\hat{\imath}\phi_1^A(\mathbf{r}_1)\phi_2^B(\mathbf{r}_2) = \phi_2^A(-\mathbf{r}_2)\phi_1^B(-\mathbf{r}_1) = (-1)^{\ell_1+\ell_2}\phi_2^A(\mathbf{r}_2)\phi_1^B(\mathbf{r}_1) \ . \tag{B.1.4}$$

The molecular wave function either is unaffected by this exchange (gerade state) or becomes negative (ungerade state): $\hat{\imath}\Psi = p\Psi$, where $p = +1(-1)$ for the gerade (ungerade) case.

Applying the inversion operator to equation (B.1.3) and using (B.1.4) yields:

$$\begin{aligned}
\hat{\imath}\Psi &= p(C_1\left[\phi_1^A(\mathbf{r}_1)\phi_2^B(\mathbf{r}_2) - \phi_2^B(\mathbf{r}_1)\phi_1^A(\mathbf{r}_2)\right]) + p(C_2\left[\phi_1^B(\mathbf{r}_1)\phi_2^A(\mathbf{r}_2) - \phi_2^A(\mathbf{r}_1)\phi_1^B(\mathbf{r}_2)\right]) \\
&= (-1)^{\ell_1+\ell_2}(C_1\left[\phi_2^A(\mathbf{r}_2)\phi_1^B(\mathbf{r}_1) - \phi_1^B(\mathbf{r}_2)\phi_2^A(\mathbf{r}_1)\right]) \\
&+ (-1)^{\ell_1+\ell_2}(C_2\left[\phi_2^B(\mathbf{r}_2)\phi_1^A(\mathbf{r}_1) - \phi_1^A(\mathbf{r}_2)\phi_2^B(\mathbf{r}_1)\right]) \ ,
\end{aligned}$$

from which we can say $C_1 = p(-1)^{\ell_1+\ell_2}C_2$, and thus:

$$\begin{aligned}
\Psi &= C_1(\left[\phi_1^A(\mathbf{r}_1)\phi_2^B(\mathbf{r}_2) - \phi_2^B(\mathbf{r}_1)\phi_1^A(\mathbf{r}_2)\right] \\
&+ p(-1)^{\ell_1+\ell_2}\left[\phi_1^B(\mathbf{r}_1)\phi_2^A(\mathbf{r}_2) - \phi_2^A(\mathbf{r}_1)\phi_1^B(\mathbf{r}_2)\right]) \ . \qquad \text{(B.1.5)}
\end{aligned}$$

Under the long-range assumption, electron 1 stays around nucleus A and electron 2 stays around nucleus B. Therefore, we can finally write:

$$\Psi = \frac{1}{\sqrt{2}}\left[\phi_1^A(\mathbf{r}_1)\phi_2^B(\mathbf{r}_2) - p(-1)^{\ell_1+\ell_2}\phi_2^A(\mathbf{r}_1)\phi_1^B(\mathbf{r}_2)\right] \ , \qquad \text{(B.1.6)}$$

where we have let $C_1 = \dfrac{1}{\sqrt{2}}$ for normalization.

B.1.2 Three-body

As in the two-electron case, the asymptotic basis states for the three-electron system are constructed from atomic wave functions given by $\phi_\imath^k(\mathbf{r}_q)$, where $\imath \equiv n_\imath \ell_\imath j_\imath m_{j_\imath}$ is the quantum state describing electron q associated with atom k.

Given three nuclei A, B, and C and three electrons 1, 2 and 3, the general asymptotic form of the electronic wave function is given by the superposition of possible combinations of $\phi_\imath^A(\mathbf{r}_q)\phi_{\imath'}^B(\mathbf{r}_{q'})\phi_{\imath''}^C(\mathbf{r}_{q''})$, where all indices run from 1 to 3, with

$\imath \neq \imath' \neq \imath''$ and $q \neq q' \neq q''$. This results in 36 different possibilities, meaning the initial wave function Ψ has 36 unique terms. For simplicity, we write

$$\Psi = \sum_{\jmath=1}^{36} c_\jmath \psi_\jmath \ , \tag{B.1.7}$$

where each $\psi_\jmath$ term represents a $\phi_\imath^A(\mathbf{r}_q)\phi_{\imath'}^B(\mathbf{r}_{q'})\phi_{\imath''}^C(\mathbf{r}_{q''})$ wave form and $c_\jmath$ is a weighting coefficient. For the two-electron case, it is sufficient to apply the $\hat{P}_{12}$ operator to antisymmetrize the general wave function. However, the three-electron case is more complex and requires use of the antisymmetrizing operator $\hat{\mathcal{A}} = \frac{1}{\sqrt{6}}\sum_{\hat{P}}(-1)^P\hat{P}$ to properly antisymmetrize the general wave function. Here, the sum is over all possible permutations of the electrons $\hat{P}$ and the $(-1)^P$ coefficient is 1 for even permutations and -1 for odd. For electrons, the overall wave function must be odd. Therefore,

$$\hat{\mathcal{A}}\Psi = -\Psi = \sum_{\jmath} c_\jmath \hat{\mathcal{A}}\psi_\jmath \ , \tag{B.1.8}$$

where each $\psi_\jmath$ term is permuted according to $\hat{\mathcal{A}}$. As this is quite cumbersome, we do not write down the results of these expansions. However, we point out that as in the two-electron case, performing this antisymmetrization allows for comparisons to be made between the coefficients, with the net result given by:

$$\begin{aligned}
|\Psi\rangle = c_1 \big[\big(& \phi_1^A(\mathbf{r}_1)\phi_2^B(\mathbf{r}_2)\phi_3^C(\mathbf{r}_3) - \phi_1^A(\mathbf{r}_1)\phi_3^C(\mathbf{r}_2)\phi_2^B(\mathbf{r}_3) - \phi_1^B(\mathbf{r}_1)\phi_3^A(\mathbf{r}_2)\phi_2^C(\mathbf{r}_3) \\
& + \phi_1^B(\mathbf{r}_1)\phi_2^C(\mathbf{r}_2)\phi_3^A(\mathbf{r}_3) + \phi_1^C(\mathbf{r}_1)\phi_2^A(\mathbf{r}_2)\phi_3^B(\mathbf{r}_3) - \phi_1^C(\mathbf{r}_1)\phi_3^B(\mathbf{r}_2)\phi_2^A(\mathbf{r}_3) \\
& + \phi_2^A(\mathbf{r}_1)\phi_3^B(\mathbf{r}_2)\phi_1^C(\mathbf{r}_3) - \phi_2^A(\mathbf{r}_1)\phi_1^C(\mathbf{r}_2)\phi_3^B(\mathbf{r}_3) + \phi_2^B(\mathbf{r}_1)\phi_3^C(\mathbf{r}_2)\phi_1^A(\mathbf{r}_3) \\
& - \phi_2^B(\mathbf{r}_1)\phi_1^A(\mathbf{r}_2)\phi_3^C(\mathbf{r}_3) - \phi_2^C(\mathbf{r}_1)\phi_1^B(\mathbf{r}_2)\phi_3^A(\mathbf{r}_3) + \phi_2^C(\mathbf{r}_1)\phi_3^A(\mathbf{r}_2)\phi_1^B(\mathbf{r}_3) \\
& + \phi_3^A(\mathbf{r}_1)\phi_1^B(\mathbf{r}_2)\phi_2^C(\mathbf{r}_3) - \phi_3^A(\mathbf{r}_1)\phi_2^C(\mathbf{r}_2)\phi_1^B(\mathbf{r}_3) + \phi_3^B(\mathbf{r}_1)\phi_1^C(\mathbf{r}_2)\phi_2^A(\mathbf{r}_3) \\
& - \phi_3^B(\mathbf{r}_1)\phi_2^A(\mathbf{r}_2)\phi_1^C(\mathbf{r}_3) + \phi_3^C(\mathbf{r}_1)\phi_1^A(\mathbf{r}_2)\phi_2^B(\mathbf{r}_3) - \phi_3^C(\mathbf{r}_1)\phi_2^B(\mathbf{r}_2)\phi_1^A(\mathbf{r}_3)\big) \\
+ c_2 \big(& \phi_1^A(\mathbf{r}_1)\phi_3^B(\mathbf{r}_2)\phi_2^C(\mathbf{r}_3) - \phi_1^A(\mathbf{r}_1)\phi_2^C(\mathbf{r}_2)\phi_3^B(\mathbf{r}_3) - \phi_1^B(\mathbf{r}_1)\phi_2^A(\mathbf{r}_2)\phi_3^C(\mathbf{r}_3) \\
& + \phi_1^B(\mathbf{r}_1)\phi_3^C(\mathbf{r}_2)\phi_2^A(\mathbf{r}_3) - \phi_1^C(\mathbf{r}_1)\phi_2^B(\mathbf{r}_2)\phi_3^A(\mathbf{r}_3) + \phi_1^C(\mathbf{r}_1)\phi_3^A(\mathbf{r}_2)\phi_2^B(\mathbf{r}_3) \\
& + \phi_2^A(\mathbf{r}_1)\phi_1^B(\mathbf{r}_2)\phi_3^C(\mathbf{r}_3) - \phi_2^A(\mathbf{r}_1)\phi_3^C(\mathbf{r}_2)\phi_1^B(\mathbf{r}_3) - \phi_2^B(\mathbf{r}_1)\phi_3^A(\mathbf{r}_2)\phi_1^C(\mathbf{r}_3) \\
& + \phi_2^B(\mathbf{r}_1)\phi_1^C(\mathbf{r}_2)\phi_3^A(\mathbf{r}_3) + \phi_2^C(\mathbf{r}_1)\phi_1^A(\mathbf{r}_2)\phi_3^B(\mathbf{r}_3) - \phi_2^C(\mathbf{r}_1)\phi_3^B(\mathbf{r}_2)\phi_1^A(\mathbf{r}_3) \\
& + \phi_3^A(\mathbf{r}_1)\phi_2^B(\mathbf{r}_2)\phi_1^C(\mathbf{r}_3) - \phi_3^A(\mathbf{r}_1)\phi_1^C(\mathbf{r}_2)\phi_2^B(\mathbf{r}_3) - \phi_3^B(\mathbf{r}_1)\phi_1^A(\mathbf{r}_2)\phi_2^C(\mathbf{r}_3) \\
& + \phi_3^B(\mathbf{r}_1)\phi_2^C(\mathbf{r}_2)\phi_1^A(\mathbf{r}_3) + \phi_3^C(\mathbf{r}_1)\phi_2^A(\mathbf{r}_2)\phi_1^B(\mathbf{r}_3) - \phi_3^C(\mathbf{r}_1)\phi_1^B(\mathbf{r}_2)\phi_2^A(\mathbf{r}_3)\big)\big] \ .
\end{aligned}$$

Finally, we relate c_1 and c_2 via the inversion operator $\hat{\imath}$ as in the two-electron case. By centering the inversion on atom B, $\hat{\imath}$ acts in the following manner:

$$\begin{aligned}
\hat{\imath}\phi_n^A(\mathbf{r}_i)\phi_m^B(\mathbf{r}_j)\phi_q^C(\mathbf{r}_k) &= \phi_q^A(-\mathbf{r}_k)\phi_m^B(-\mathbf{r}_j)\phi_n^C(-\mathbf{r}_i) \\
&= \phi_q^A(\mathbf{r}_k)\phi_m^B(\mathbf{r}_j)\phi_n^C(\mathbf{r}_i)\,(-1)^{\ell_i+\ell_j+\ell_k} \, . \qquad \text{(B.1.9)}
\end{aligned}$$

Carrying out $\hat{\imath}\Psi = p\Psi$, where $p = +1(-1)$ for gerade (ungerade) states, we conveniently find $c_2 = c_1 p(-1)^{\ell_1+\ell_2+\ell_3}$ and arrive at the most general form for the three-electron wave function:

$$\begin{aligned}
|\Psi\rangle =& c_1 \big[\big(\phi_1^A(\mathbf{r}_1)\phi_2^B(\mathbf{r}_2)\phi_3^C(\mathbf{r}_3) - \phi_1^A(\mathbf{r}_1)\phi_3^C(\mathbf{r}_2)\phi_2^B(\mathbf{r}_3) - \phi_1^B(\mathbf{r}_1)\phi_3^A(\mathbf{r}_2)\phi_2^C(\mathbf{r}_3)\\
&+ \phi_1^B(\mathbf{r}_1)\phi_2^C(\mathbf{r}_2)\phi_3^A(\mathbf{r}_3) + \phi_1^C(\mathbf{r}_1)\phi_2^A(\mathbf{r}_2)\phi_3^B(\mathbf{r}_3) - \phi_1^C(\mathbf{r}_1)\phi_3^B(\mathbf{r}_2)\phi_2^A(\mathbf{r}_3)\\
&+ \phi_2^A(\mathbf{r}_1)\phi_3^B(\mathbf{r}_2)\phi_1^C(\mathbf{r}_3) - \phi_2^A(\mathbf{r}_1)\phi_1^C(\mathbf{r}_2)\phi_3^B(\mathbf{r}_3) + \phi_2^B(\mathbf{r}_1)\phi_3^C(\mathbf{r}_2)\phi_1^A(\mathbf{r}_3)\\
&- \phi_2^B(\mathbf{r}_1)\phi_1^A(\mathbf{r}_2)\phi_3^C(\mathbf{r}_3) - \phi_2^C(\mathbf{r}_1)\phi_1^B(\mathbf{r}_2)\phi_3^A(\mathbf{r}_3) + \phi_2^C(\mathbf{r}_1)\phi_3^A(\mathbf{r}_2)\phi_1^B(\mathbf{r}_3)\\
&+ \phi_3^A(\mathbf{r}_1)\phi_1^B(\mathbf{r}_2)\phi_2^C(\mathbf{r}_3) - \phi_3^A(\mathbf{r}_1)\phi_2^C(\mathbf{r}_2)\phi_1^B(\mathbf{r}_3) + \phi_3^B(\mathbf{r}_1)\phi_1^C(\mathbf{r}_2)\phi_2^A(\mathbf{r}_3)\\
&-\phi_3^B(\mathbf{r}_1)\phi_2^A(\mathbf{r}_2)\phi_1^C(\mathbf{r}_3) + \phi_3^C(\mathbf{r}_1)\phi_1^A(\mathbf{r}_2)\phi_2^B(\mathbf{r}_3) - \phi_3^C(\mathbf{r}_1)\phi_2^B(\mathbf{r}_2)\phi_1^A(\mathbf{r}_3)\big)\\
-p(-1)^{\ell_1+\ell_2+\ell_3}& \big(\phi_1^A(\mathbf{r}_1)\phi_3^B(\mathbf{r}_2)\phi_2^C(\mathbf{r}_3) - \phi_1^A(\mathbf{r}_1)\phi_2^C(\mathbf{r}_2)\phi_3^B(\mathbf{r}_3) - \phi_1^B(\mathbf{r}_1)\phi_2^A(\mathbf{r}_2)\phi_3^C(\mathbf{r}_3)\\
&+ \phi_1^B(\mathbf{r}_1)\phi_3^C(\mathbf{r}_2)\phi_2^A(\mathbf{r}_3) - \phi_1^C(\mathbf{r}_1)\phi_2^B(\mathbf{r}_2)\phi_3^A(\mathbf{r}_3) + \phi_1^C(\mathbf{r}_1)\phi_3^A(\mathbf{r}_2)\phi_2^B(\mathbf{r}_3)\\
&+ \phi_2^A(\mathbf{r}_1)\phi_1^B(\mathbf{r}_2)\phi_3^C(\mathbf{r}_3) - \phi_2^A(\mathbf{r}_1)\phi_3^C(\mathbf{r}_2)\phi_1^B(\mathbf{r}_3) - \phi_2^B(\mathbf{r}_1)\phi_3^A(\mathbf{r}_2)\phi_1^C(\mathbf{r}_3)\\
&+ \phi_2^B(\mathbf{r}_1)\phi_1^C(\mathbf{r}_2)\phi_3^A(\mathbf{r}_3) + \phi_2^C(\mathbf{r}_1)\phi_1^A(\mathbf{r}_2)\phi_3^B(\mathbf{r}_3) - \phi_2^C(\mathbf{r}_1)\phi_3^B(\mathbf{r}_2)\phi_1^A(\mathbf{r}_3)\\
&+ \phi_3^A(\mathbf{r}_1)\phi_2^B(\mathbf{r}_2)\phi_1^C(\mathbf{r}_3) - \phi_3^A(\mathbf{r}_1)\phi_1^C(\mathbf{r}_2)\phi_2^B(\mathbf{r}_3) - \phi_3^B(\mathbf{r}_1)\phi_1^A(\mathbf{r}_2)\phi_2^C(\mathbf{r}_3)\\
&+\phi_3^B(\mathbf{r}_1)\phi_2^C(\mathbf{r}_2)\phi_1^A(\mathbf{r}_3) + \phi_3^C(\mathbf{r}_1)\phi_2^A(\mathbf{r}_2)\phi_1^B(\mathbf{r}_3) - \phi_3^C(\mathbf{r}_1)\phi_1^B(\mathbf{r}_2)\phi_2^A(\mathbf{r}_3)\big)\big] \; .
\end{aligned}$$

However, under the long-range assumption, electron 1 is localized at atom A, electron 2 is localized at atom B, and electron 3 is localized at atom C. When we neglect terms contrary to this configuration, the above expression greatly reduces to:

$$\begin{aligned}
|\Psi\rangle = \frac{1}{\sqrt{6}} &\big[\big(\phi_1^A(\mathbf{r}_1)\phi_2^B(\mathbf{r}_2)\phi_3^C(\mathbf{r}_3) + \phi_2^A(\mathbf{r}_1)\phi_3^B(\mathbf{r}_2)\phi_1^C(\mathbf{r}_3) + \phi_3^A(\mathbf{r}_1)\phi_1^B(\mathbf{r}_2)\phi_2^C(\mathbf{r}_3)\big)\\
- p(-1)^{\ell_1+\ell_2} &\big(\phi_1^A(\mathbf{r}_1)\phi_3^B(\mathbf{r}_2)\phi_2^C(\mathbf{r}_3) + \phi_2^A(\mathbf{r}_1)\phi_1^B(\mathbf{r}_2)\phi_3^C(\mathbf{r}_3) + \phi_3^A(\mathbf{r}_1)\phi_2^B(\mathbf{r}_2)\phi_1^C(\mathbf{r}_3)\big)\big] \; ,
\end{aligned}$$

where we have let $c_1 = \dfrac{1}{\sqrt{6}}$ for normalization.

B.2 Long-range interactions

B.2.1 Rydberg-Rydberg energy

The long-range Rydberg-Rydberg interaction energy is derived from an expansion of the Coulomb potential between two charge distributions. In general, there are many methods of performing such an expansion, but we will use the classical spherical multipole expansion as in [82].

We consider two charge distributions I and II, with centers A and B, respectively. We let any charge in region I be described as $q_\imath$ and any charge in region II as $q_\jmath$, so that the vector pointing from A to charge $q_\imath$ is $\vec{\boldsymbol{r}}_\imath$ and the vector pointing from B to charge $q_\jmath$ is $\vec{\boldsymbol{r}}_\jmath$. Under the long-range conditions that we consider in this dissertation, the charge distributions do not overlap. That is to say, the distance R between centers A and B is much larger than the distance $|\vec{\boldsymbol{r}}_k|$ of any charge q_k from its respective center. Under these conditions, the total potential at R due to distribution I is given by a sum of all of the charges in distribution I, *i.e.*

$$\begin{aligned}\Phi(\vec{\boldsymbol{R}}) &= \sum_\imath \frac{q_\imath}{|\vec{\boldsymbol{R}} - \vec{\boldsymbol{r}}_\imath|} \\ &= \sum_\imath q_\imath \sum_{L=0}^{\infty} \frac{4\pi}{2L+1} \sum_{M=-L}^{L} (-1)^M \frac{r_\imath^L}{R^{L+1}} Y_L^{-M}(\hat{\boldsymbol{R}})\, Y_L^M(\hat{\boldsymbol{r}}_\imath)\ , \end{aligned} \tag{B.2.1}$$

where $r_\imath \equiv |\vec{\boldsymbol{r}}_\imath|$, L and M define the multipole terms, and $Y_\ell^m(\hat{\boldsymbol{x}})$ are the spherical harmonics. The interaction energy V between the two charge distributions is then given by the sum of the Coulomb energies between any two charges q_i and q_j:

$$\begin{aligned} V &= \sum_j q_j \Phi(\vec{\boldsymbol{R}} + \vec{\boldsymbol{r}}_j) \\ &= \sum_j q_j \sum_i \frac{q_i}{|\vec{\boldsymbol{R}} + \vec{\boldsymbol{r}}_j - \vec{\boldsymbol{r}}_i|} \\ &= \sum_{i,j} q_i q_j \sum_{L=0}^{\infty} (-1)^M \frac{4\pi}{2L+1} \sum_{M=-L}^{L} \frac{u_{ij}^L}{R^{L+1}} Y_L^{-M}(\hat{\boldsymbol{R}})\; Y_L^M(\hat{\boldsymbol{u}}_{ij}) \; . \end{aligned} \tag{B.2.2}$$

Here, we have defined $\vec{\boldsymbol{u}}_{ij} \equiv \vec{\boldsymbol{r}}_i - \vec{\boldsymbol{r}}_j$ as the vector between charges q_i and q_j: $u_{ij} \equiv |\vec{\boldsymbol{u}}_{ij}|$ represents its magnitude and $\hat{\boldsymbol{u}}_{ij}$ represents its direction. At this point, we will follow the approach given by [83] and use rescaled spherical harmonics, known as the *solid harmonics*. Defining the regular solid harmonic as:

$$R_\ell^m(\vec{\boldsymbol{x}}) = \left(\frac{4\pi}{2\ell+1}\right)^{1/2} |\vec{\boldsymbol{x}}|^\ell \, Y_\ell^m(\hat{\boldsymbol{x}}) \; , \tag{B.2.3}$$

and the irregular solid harmonic as:

$$I_\ell^m(\vec{\boldsymbol{x}}) = \left(\frac{4\pi}{2\ell+1}\right)^{1/2} |\vec{\boldsymbol{x}}|^{-\ell-1} \, Y_\ell^m(\hat{\boldsymbol{x}}) \; , \tag{B.2.4}$$

we rewrite Equation (B.2.2) as:

$$V = \sum_{i,j} q_i q_j \sum_{L=0}^{\infty} \sum_{M=-L}^{L} (-1)^M I_L^{-M}(\vec{\boldsymbol{R}})\, R_L^M(\vec{\boldsymbol{u}}_{ij}) \; . \tag{B.2.5}$$

Making use of the addition theorem for solid harmonics, $R_L^M(\vec{\boldsymbol{u}}_{ij}) = R_L^M(\vec{\boldsymbol{r}}_i - \vec{\boldsymbol{r}}_j)$ can be expanded as:

$$R_L^M(\vec{\boldsymbol{r}}_i - \vec{\boldsymbol{r}}_j) = \sum_{\ell_A}^{L} \left(B_{2L}^{2\ell_A}\right)^{1/2} \sum_{m_A=-\ell_A}^{\ell_A} R_{\ell_A}^{m_A}(\vec{\boldsymbol{r}}_i)\, R_{L-\ell_A}^{M-m_A}(-\vec{\boldsymbol{r}}_j) \\ \times \langle \ell_A, m_A; L-\ell_A, M-m_A | LM \rangle \ , \tag{B.2.6}$$

where $B_n^k \equiv \frac{n!}{k!(n-k)!}$ is the binomial coefficient and $\langle \cdots | \cdots \rangle$ represents a Clebsch-Gordan coefficient. Using Equations (B.2.3), (B.2.4), (B.2.6), and the identities

$$R_\ell^m(-\vec{\boldsymbol{x}}) \equiv (-1)^\ell R_\ell^m(\vec{\boldsymbol{x}}) \tag{B.2.7}$$

and

$$\langle \ell_A, m_A; L-\ell_A, M-m_A | LM \rangle = \left(B_{L+M}^{\ell_A+m_A}\, B_{L-M}^{\ell_A-m_A}\right)^{1/2} \left(B_{2L}^{2\ell_A}\right)^{-1/2} \ , \tag{B.2.8}$$

we express Equation (B.2.5) as:

$$V = \sum_{i,j} q_i q_j \sum_{L=0}^{\infty} \sum_{M=-L}^{L} (-1)^{M+L-\ell_A} \left(\frac{4\pi}{2L+1}\right)^{1/2} \frac{Y_L^{-M}(\hat{\boldsymbol{R}})}{R^{L+1}} \\ \times \sum_{\ell_A=0}^{L} \sum_{m_A=-\ell_A}^{\ell_A} \left(B_{L+M}^{\ell_A+m_A}\, B_{L-M}^{\ell_A-m_A}\right)^{1/2} \left(\frac{4\pi}{2\ell_A+1}\right)^{1/2} r_i^{\ell_A}\, Y_{\ell_A}^{m_A}(\hat{\boldsymbol{r}}_i) \\ \times \left(\frac{4\pi}{2(L-\ell_A)+1}\right)^{1/2} r_j^{L-\ell_A}\, Y_{L-\ell_A}^{M-m_A}(\hat{\boldsymbol{r}}_j) \ . \tag{B.2.9}$$

If the vector $\vec{\boldsymbol{R}}$ that connects centers A and B is taken to be along the z-axis, *i.e.* $\vec{\boldsymbol{R}} = R\hat{z}$, then $Y_L^{-M}(\hat{\boldsymbol{R}}) \equiv Y_L^{-M}(\hat{z}) = \left(\frac{(2L+1)(L+M)!}{4\pi\,(L-M)!}\right)^{1/2} \delta_{-M,0}$, with $\delta_{-M,0}$

beging the Kronecker delta function. Equation (B.2.9) then becomes

$$\begin{aligned} V = \sum_{\imath,\jmath} q_\imath q_\jmath \sum_{L=0}^{\infty} \sum_{\ell_A=0}^{L} \frac{(-1)^{\ell_B}}{R^{\ell_A+\ell_B+1}} \sum_{m_A=-\ell_A}^{\ell_A} \left(B_{\ell_A+\ell_B}^{\ell_A+m_A}\, B_{\ell_A+\ell_B}^{\ell_A-m_A} \right)^{1/2} \\ \times \left(\frac{4\pi}{2\ell_A+1} \right)^{1/2} \left(\frac{4\pi}{2\ell_B+1} \right)^{1/2} r_\imath^{\ell_A}\, Y_{\ell_A}^{m_A}(\hat{\boldsymbol{r}}_\imath)\, r_\jmath^{\ell_B}\, Y_{\ell_B}^{-m_A}(\hat{\boldsymbol{r}}_\jmath) \,, \end{aligned} \tag{B.2.10}$$

where we have also let $\ell_B = L - \ell_A$.

Finally, we assume that each distribution contains only one Rydberg atom, with their respective nuclei located at centers A and B; the electron associated to core $A(B)$ is subscripted as $1(2)$. Using the definition of the binomial coefficient, it can easily be shown that $B_{\ell_A+\ell_B}^{\ell_A-m_A} = B_{\ell_A+\ell_B}^{\ell_B+m_A}$. Dropping the summations over $\imath$ and $\jmath$, letting $e_1 = e_2 = 1$ in atomic units, and reordering the sums over L and ℓ_A (note: this is only allowed for infinite sums), we define the Rydberg-Rydberg interaction energy as:

$$\begin{aligned} V = \sum_{\ell_A=0}^{\infty} \sum_{\ell_B=0}^{\infty} \frac{(-1)^{\ell_B} 4\pi}{R^{\ell_A+\ell_B+1}} \left(\frac{1}{(2\ell_A+1)(2\ell_B+1)} \right)^{1/2} r_\imath^{\ell_A}\, r_\jmath^{\ell_B} \\ \times \sum_{m_A=-\ell_A}^{\ell_A} \left(B_{\ell_A+\ell_B}^{\ell_A+m_A}\, B_{\ell_A+\ell_B}^{\ell_B+m_A} \right)^{1/2} Y_{\ell_A}^{m_A}(\hat{\boldsymbol{r}}_\imath)\, Y_{\ell_B}^{-m_A}(\hat{\boldsymbol{r}}_\jmath) \,. \end{aligned} \tag{B.2.11}$$

As discussed in Chapter 2, we only consider dipole-dipole ($\ell_A = \ell_B = 1$) interactions and quadrupole-quadrupole ($\ell_A = \ell_B = 2$) interactions. In this manner, we define their respective terms in the expansion *via*

$$V_\ell(R) = \frac{(-1)^\ell\, 4\pi\, r_1^\ell r_2^\ell}{(2\ell+1) R^{2\ell+1}} \sum_m B_{2\ell}^{\ell+m} Y_\ell^m(\hat{r}_1) Y_\ell^{-m}(\hat{r}_2) \,. \tag{B.2.12}$$

where $\ell = 1(2)$ for dipolar (quadrupolar) interactions.

B.2.2 Hamiltonian matrix elements

The interaction Hamiltonian that we diagonalize has matrix elements $\langle n_1\ell_1\jmath_1 m_{\jmath_1}|\langle n_2\ell_2\jmath_2(\Omega - m_{\jmath_1})|V_\ell(R)|n_3\ell_3\jmath_3 m_{\jmath_3}\rangle|n_4\ell_4\jmath_4(\Omega - m_{\jmath_3})\rangle$, defined by:

$$\begin{aligned}\langle 1;2|V_\ell(R)|3;4\rangle &= (-1)^\ell \frac{4\pi}{(2\ell+1)}\frac{1}{R^{2\ell+1}}\sum_m B_{2\ell}^{\ell+m}\langle n_1\ell_1\jmath_1|r_1^\ell|n_3\ell_3\jmath_3\rangle\langle n_2\ell_2\jmath_2|r_2^\ell|n_4\ell_4\jmath_4\rangle \\ &\times \langle \ell_1\jmath_1 m_{\jmath_1}|Y_\ell^m(\hat{\mathbf{r}}_1)|\ell_3\jmath_3 m_{\jmath_3}\rangle\langle \ell_2\jmath_2\Omega - m_{\jmath_1}|Y_\ell^{-m}(\hat{\mathbf{r}}_2)|\ell_4\jmath_4\Omega - m_{\jmath_2}\rangle\,, \quad \text{(B.2.13)}\end{aligned}$$

where the summation runs from $m = -\ell$ to ℓ. For the angular portions of (B.2.13), it is more convenient to express the angular wave functions in the uncoupled basis using the standard angular momentum addition. For example,

$$\langle \ell_1\jmath_1 m_{\jmath_1}| = \sum_{m_{\ell_1}}\sum_{m_{s_1}}\langle \jmath_1 m_{\jmath_1}|\ell_1 s_1; m_{\ell_1} m_{s_1}\rangle\langle \ell_1 s_1; m_{\ell_1} m_{s_1}|\ , \qquad \text{(B.2.14)}$$

where $\langle \jmath_1 m_{\jmath_1}|\ell_1 s_1; m_{\ell_1} m_{s_1}\rangle$ is the Clebsch-Gordan Coefficient and can be expressed in terms of the Wigner $3\jmath$ symbol as:

$$\langle \jmath_1 m_{\jmath_1}|\ell_1 s_1; m_{\ell_1} m_{s_1}\rangle = \sqrt{2\jmath_1 + 1}\,(-1)^{s_1-\ell_1-m_{\jmath_1}}\begin{pmatrix} \ell_1 & s_1 & \jmath_1 \\ m_{\ell_1} & m_{s_1} & -m_{\jmath_1}\end{pmatrix}.$$

We express the other three wave functions in the uncoupled basis as in (B.2.14) and substitute into equation (B.2.13):

$$\begin{aligned}
\langle 1;2|V_\ell(R)|3;4\rangle &= (-1)^\ell\,(-1)^{s_1+s_2+s_3+s_4-(\ell_1+\ell_2+\ell_3+\ell_4)-2\Omega}\,\frac{4\pi}{(2\ell+1)}\frac{1}{R^{2\ell+1}} \\
&\times \sum_m B_{2\ell}^{\ell+m}\mathcal{R}_{13}^\ell\mathcal{R}_{24}^\ell \sum_{\substack{m_{\ell_1}\\ m_{\ell_2}\\ m_{\ell_3}\\ m_{\ell_4}}}\sum_{\substack{m_{s_1}\\ m_{s_2}\\ m_{s_3}\\ m_{s_4}}} \sqrt{(2j_1+1)(2j_2+1)(2j_3+1)(2j_4+1)} \\
&\times \ \langle \ell_1 m_{\ell_1}|Y_\ell^m(\hat{\mathbf{r}}_1)|\ell_3 m_{\ell_3}\rangle\langle \ell_2 m_{\ell_2}|Y_\ell^{-m}(\hat{\mathbf{r}}_2)|\ell_4 m_{\ell_4}\rangle \qquad\qquad \text{(B.2.15)} \\
&\times \begin{pmatrix} \ell_1 & s_1 & j_1 \\ m_{\ell_1} & m_{s_1} & -m_{j_1} \end{pmatrix}\begin{pmatrix} \ell_2 & s_2 & j_2 \\ m_{\ell_2} & m_{s_2} & -(\Omega-m_{j_1}) \end{pmatrix} \\
&\times \begin{pmatrix} \ell_3 & s_3 & j_3 \\ m_{\ell_3} & m_{s_3} & -m_{j_3} \end{pmatrix}\begin{pmatrix} \ell_4 & s_4 & j_4 \\ m_{\ell_4} & m_{s_4} & -(\Omega-m_{j_3}) \end{pmatrix} \\
&\times \ \delta_{s_2 s_4}\delta_{s_1 s_3}\delta_{m_{s_2} m_{s_4}}\delta_{m_{s_1} m_{s_3}}\ ,
\end{aligned}$$

where $\delta_{s_i s_j} = \langle s_i|s_j\rangle$ and $\delta_{m_{s_i} m_{s_j}} = \langle m_{s_i}|m_{s_j}\rangle$ are Kronecker delta functions arising from the spin component interactions in the uncoupled basis representation and $\mathcal{R}_{ij}^\ell$ are the radial matrix elements, $\langle i|r^\ell|j\rangle$.

To simplify expression (B.2.15), we make use of the following identities:

$$\begin{aligned}
\langle \ell_i m_{\ell_i}|Y_L^M|\ell_j m_{\ell_j}\rangle &= (-1)^{m_{\ell_i}}\sqrt{\frac{(2\ell_i+1)(2L+1)(2\ell_j+1)}{4\pi}} \\
&\times \begin{pmatrix} \ell_i & L & \ell_j \\ 0 & 0 & 0 \end{pmatrix}\begin{pmatrix} \ell_i & L & \ell_j \\ -m_{\ell_i} & M & m_{\ell_j} \end{pmatrix} \qquad\qquad \text{(B.2.16)}
\end{aligned}$$

and

$$\sum_{m_6}\sum_{m_5}\sum_{m_4}(-1)^{j_4+j_5+j_6-m_4-m_5-m_6}$$
$$\times\begin{pmatrix} j_5 & j_1 & j_6 \\ m_5 & -m_1 & -m_6 \end{pmatrix}\begin{pmatrix} j_6 & j_2 & j_4 \\ m_6 & -m_2 & -m_4 \end{pmatrix}\begin{pmatrix} j_4 & j_3 & j_5 \\ m_4 & -m_3 & -m_5 \end{pmatrix}$$
$$= \begin{pmatrix} j_1 & j_2 & j_3 \\ m_1 & m_2 & m_3 \end{pmatrix}\begin{Bmatrix} j_1 & j_2 & j_3 \\ j_4 & j_5 & j_6 \end{Bmatrix} . \tag{B.2.17}$$

Using these identities in (B 2.15), we arrive at the final expression for the interaction matrix elements:

$$\langle 12|V_\ell(R)|34\rangle = (-1)^{j_1+j_2+j_3+j_4+\ell-1-\Omega}\sqrt{\hat{\ell}_1\hat{\ell}_2\hat{\ell}_3\hat{\ell}_4\hat{j}_1\hat{j}_2\hat{j}_3\hat{j}_4}\;\frac{\mathcal{R}_{13}\mathcal{R}_{24}}{R^{2\ell+1}}$$
$$\times\begin{pmatrix} \ell_1 & \ell & \ell_3 \\ 0 & 0 & 0 \end{pmatrix}\begin{pmatrix} \ell_2 & \ell & \ell_4 \\ 0 & 0 & 0 \end{pmatrix}\begin{Bmatrix} j_1 & \ell & j_3 \\ \ell_3 & \frac{1}{2} & \ell_1 \end{Bmatrix}\begin{Bmatrix} j_2 & \ell & j_4 \\ \ell_4 & \frac{1}{2} & \ell_2 \end{Bmatrix} \tag{B 2.18}$$
$$\times\sum_m B_{2\ell}^{\ell+m}\begin{pmatrix} j_1 & \ell & j_3 \\ -m_{j_1} & m & m_{j_3} \end{pmatrix}\begin{pmatrix} j_2 & \ell & j_4 \\ -\Omega+m_{j_1} & -m & \Omega-m_{j_3} \end{pmatrix} .$$

B.3 Radial matrix elements via the Numerov method

We calculate the radial matrix elements $\langle n\ell_j | r^\sigma | n'\ell'_{j'} \rangle$, $\sigma \geq 0$ using an inward-numerical-integration scheme based on the Numerov algorithm as was done in [38]. In general, the radial form of the electronic Schrödinger equation is given in atomic units by:

$$\frac{1}{r^2}\frac{d}{dr}\left(r^2\frac{dR(r)}{dr}\right) - \left(2\left[V(r) - E\right] + \frac{\ell(\ell+1)}{r^2}\right)R(r) = 0\ , \tag{B.3.1}$$

where $R(r)$ is the radial wave function of an electron with spatial coordinate r and angular quantum number ℓ. For Rydberg atoms, the potential experienced by the orbiting electron is essentially Coulombic, *i.e.* $V(r) \sim -\frac{1}{r}$, and the total energy E is the Rydberg energy $E = -\frac{1}{2(n-\delta_\ell)^2}$, where δ_ℓ is the quantum defect (see table 2.1). By appropriately rescaling the spatial variable and the wave function as $x = \ln r$ and $X = r^{1/2}R$, respectively, we eliminate the first derivative from expression B.3.1:

$$\frac{d^2X(x)}{dx^2} = g(x)X(x)\ . \tag{B.3.2}$$

Here, $g(x) = 2e^{2x}\left[V(x) - E\right] + \left(\ell + \frac{1}{2}\right)^2$, with $V(x) = -\frac{1}{e^x}$.

The Numerov algorithm is a multi-step method, meaning it utilizes previous iteration points to gain efficiency. The iteration points are determined from Taylor expanding the scaled wave function about a step h above and below the current point, *i.e.*

$$\begin{aligned}X(x+h) &\cong X(x) + hX'(x) + \frac{h^2}{2}X''(x) \\ &\qquad + \frac{h^3}{3!}X'''(x) + \frac{h^4}{4!}X^{(\mathrm{iv})}(x) + \ldots \qquad \text{(B.3.3)} \\ X(x-h) &\cong X(x) - hX'(x) + \frac{h^2}{2}X''(x) \\ &\qquad - \frac{h^3}{3!}X'''(x) + \frac{h^4}{4!}X^{(\mathrm{iv})}(x) - \ldots \qquad \text{(B.3.4)}\end{aligned}$$

These two equations are added together to obtain an expression for the second derivative, which we then set equal to equation B.3.2:

$$g(x)X(x) = \frac{X(x+h) + X(x-h) - 2X(x)}{h^2} - \frac{h^2}{12}X^{(\mathrm{iv})}(x)\ . \qquad \text{(B.3.5)}$$

Finally, we take the second derivative of equation B.3.2, and use the result to replace the fourth order derivative term in equation B.3.5. After some manipulation, the final result is given in iterative form as:

$$X_{k+1} = \frac{2X_k - X_{k-1} + \frac{h^2}{12}\left(10\,g_k^2\,X_k + g_{k-1}^2 X_{k-1}\right)}{1 - \frac{h^2}{12}\,g_{k+1}^2}\ , \qquad \text{(B.3.6)}$$

where $g_k^2 = \left(\ell + \frac{1}{2}\right)^2 + 2e^{2x_k}(-e^{-x_k} - E)$, with k being the counting index.

For bound electrons, only the outer boundary condition of the respective wave function is well defined. Thus, we begin in the classically forbidden range $r \gtrsim 2(n-\delta_\ell)^2$, where the wave function is a decaying exponential, and integrate inward until the solution begins to diverge (typically right around the inner turning point $r \sim \ell(\ell+1)$). Since the major contributions to the matrix elements occur at larger distances, there is little loss of accuracy in truncating the integration at the point of divergence. The matrix elements of r^σ are then given by:

$$\langle n, \ell_j | r^\sigma | n', \ell'_{j'} \rangle = \frac{\sum_k X_k X'_k r_k^{2+\sigma}}{N N'} \;, \tag{B.3.7}$$

where $N^{(')} = \left(\sum_k X_k^{(')2} r_k^2 \right)^{1/2}$ define the normalizations for X and X' and r_k is replaced with the scaled variable x_k as defined above.

References

[1] J. Millen, G. Lochead, and M. P. A. Jones, *Two-Electron Excitation of an Interacting Cold Rydberg Gas*, Phys. Rev. Lett. **105**, 21 213004 (2010).

[2] T. Gallagher, *Rydberg Atoms*, Cambridge University Press, Cambridge, United Kingdom (1994).

[3] T. Calarco, H. Briegel, D. Jaksch, J. Cirac, and P. Zoller, *Entangling neutral atoms for quantum information processing*, J. Mod. Opt. **47**, 12 2137 (2000).

[4] K. G. H. Vollbrecht, E. Solano, and J. I. Cirac, *Ensemble Quantum Computation with Atoms in Periodic Potentials*, Phys. Rev. Lett. **93**, 22 220502 (2004).

[5] G. K. Brennen, I. H. Deutsch, and P. S. Jessen, *Entangling dipole-dipole interactions for quantum logic with neutral atoms*, Phys. Rev. A **61**, 6 062309 (2000).

[6] D. Jaksch, J. I. Cirac, P. Zoller, S. L. Rolston, R. Côté, and M. D. Lukin, *Fast Quantum Gates for Neutral Atoms*, Phys. Rev. Lett. **85**, 10 2208 (2000).

[7] I. E. Protsenko, G. Reymond, N. Schlosser, and P. Grangier, *Operation of a quantum phase gate using neutral atoms in microscopic dipole traps*, Phys. Rev. A **65**, 5 052301 (2002).

[8] R. Côté, A. Russell, E. Eyler, and P. L. Gould, *Quantum random walk with Rydberg atoms in an optical lattice*, New Journal of Physics **8**, 156 1 (2006).

[9] M. D. Lukin, M. Fleischhauer, R. Cote, L. M. Duan, D. Jaksch, J. I. Cirac, and P. Zoller, *Dipole Blockade and Quantum Information Processing in Mesoscopic Atomic Ensembles*, Phys. Rev. Lett. **87**, 3 037901 (2001).

[10] D. Tong, S. M. Farooqi, J. Stanojevic, S. Krishnan, Y. P. Zhang, R. Côté, E. E. Eyler, and P. L. Gould, *Local Blockade of Rydberg Excitation in an Ultracold Gas*, Phys. Rev. Lett. **93**, 6 063001 (2004).

[11] K. Singer, M. Reetz-Lamour, T. Amthor, L. G. Marcassa, and M. Weidemüller, *Suppression of Excitation and Spectral Broadening Induced by Interactions in a Cold Gas of Rydberg Atoms*, Phys. Rev. Lett. **93**, 16 163001 (2004).

[12] T. C. Liebisch, A. Reinhard, P. R. Berman, and G. Raithel, *Atom Counting Statistics in Ensembles of Interacting Rydberg Atoms*, Phys. Rev. Lett. **95**, 25 253002 (2005).

[13] T. Vogt, M. Viteau, J. Zhao, A. Chotia, D. Comparat, and P. Pillet, *Dipole Blockade at Förster Resonances in High Resolution Laser Excitation of Rydberg States of Cesium Atoms*, Phys. Rev. Lett. **97**, 8 083003 (2006).

[14] R. Heidemann, U. Raitzsch, V. Bendkowsky, B. Butscher, R. Löw, and T. Pfau, *Rydberg Excitation of Bose-Einstein Condensates*, Phys. Rev. Lett. **100**, 3 033601 (2008).

[15] A. Gaëtan, Y. Miroshnychenko, T. Wilk, A. Chotia, M. Viteau, D. Comparat, P. Pillet, A. Browaeys, and P. Grangier, *Observation of collective excitation of two individual atoms in the Rydberg blockade regime*, Nature Physics **5** 115 (2009).

[16] E. Urban, T. A. Johnson, T. Henage, L. Isenhower, D. D. Yavuz, T. G. Walker, and M. Saffman, *Observation of Rydberg blockade between two atoms*, Nature Physics **5** 110 (2009).

[17] L. Isenhower, E. Urban, X. L. Zhang, A. T. Gill, T. Henage, T. A. Johnson, T. G. Walker, and M. Saffman, *Demonstration of a Neutral Atom Controlled-NOT Quantum Gate*, Phys. Rev. Lett. **104**, 1 010503 (2010).

[18] M. Saffman, T. G. Walker, and K. Mølmer, *Quantum information with Rydberg atoms*, Rev. Mod. Phys. **82**, 3 2313 (2010).

[19] C. H. Greene, A. S. Dickinson, and H. R. Sadeghpour, *Creation of Polar and Nonpolar Ultra-Long-Range Rydberg Molecules*, Phys. Rev. Lett. **85**, 12 2458 (2000).

[20] V. Bendowsky, B. Butscher, J. Nipper, J. P. Shaffer, R. Löw, and T. Pfau, *Observation of ultralong-range Rydberg molecules*, Nature **458** 1005 (2009).

[21] C. Boisseau, I. Simbotin, and R. Côté, *Macrodimers: Ultralong Range Rydberg Molecules*, Phys. Rev. Lett. **88**, 13 133004 (2002).

[22] A. Schwettmann, J. Crawford, K. R. Overstreet, and J. P. Shaffer, *Cold Cs Rydberg-gas interactions*, Phys. Rev. A **74**, 2 020701 (2006).

[23] K. R. Overstreet, A. Schwettmann, J. Tallant, D. Booth, and J. P. Shaffer, *Observation of electric-field-induced Cs Rydberg atom macrodimers*, Nature Physics **5** 581 (2009).

[24] S. M. Farooqi, D. Tong, S. Krishnan, J. Stanojevic, Y. P. Zhang, J. R. Ensher, A. S. Estrin, C. Boisseau, R. Côté, E. E. Eyler, and P. L. Gould, *Long-Range Molecular Resonances in a Cold Rydberg Gas*, Phys. Rev. Lett. **91**, 18 183002 (2003).

[25] K. R. Overstreet, A. Schwettmann, J. Tallant, and J. P. Shaffer, *Photoinitiated collisions between cold Cs Rydberg atoms*, Phys. Rev. A **76**, 1 011403 (2007).

[26] K. Singer, J. Stanojevic, M. Weidermüller, and R. Côté, *Long-range interactions between alkali Rydberg atom pairs correlated to the ns-ns, np-np and nd-nd asymptotes*, J. Phys. B: At. Mol. Opt. Phys. **38**, 2 S295 (2005).

[27] J. Stanojevic, R. Côté, D. Tong, S. Farooqi, E. Eyler, and P. Gould, *Long-range Rydberg-Rydberg interactions and molecular resonances*, Eur. Phys. J. D **40** 3 (2006).

[28] J. Stanojevic, R. Côté, D. Tong, E. E. Eyler, and P. L. Gould, *Long-range potentials and $(n-1)d+ns$ molecular resonances in an ultracold Rydberg gas*, Phys. Rev. A **78**, 5 052709 (2008).

[29] P. Bernath, *Spectra of Atoms and Molecules*, Oxford University Press, New York, New York (2005).

[30] I. Mourachko, D. Comparat, F. de Tomasi, A. Fioretti, P. Nosbaum, V. M. Akulin, and P. Pillet, *Many-Body Effects in a Frozen Rydberg Gas*, Phys. Rev. Lett. **80**, 2 253 (1998).

[31] W. R. Anderson, J. R. Veale, and T. F. Gallagher, *Resonant Dipole-Dipole Energy Transfer in a Nearly Frozen Rydberg Gas*, Phys. Rev. Lett. **80**, 2 249 (1998).

[32] G. Arfken and H. Weber, *Mathematical Methods for Physicists*, Academic Press, San Diego, California (2001).

[33] L. Landau and E. Lifshitz, *Quantum Mechanics (Non-relativistic Theory), Third Edition*, Pergamon Press Ltd., Oxford, Great Britain (1997).

[34] J. Stanojevic, *Effects of Strong Interactions in Ultracold Rydberg Gases*, Ph.D. thesis, University of Connecticut (2007).

[35] J. Brown and A. Carrington, *Rotational Spectroscopy of Diatomic Molecules*, Cambridge University Press, Cambridge, United Kingdom (2003).

[36] W. Li, I. Mourachko, M. W. Noel, and T. F. Gallagher, *Millimeter-wave spectroscopy of cold Rb Rydberg atoms in a magneto-optical trap: Quantum defects of the ns, np, and nd series*, Phys. Rev. A **67**, 5 052502 (2003).

[37] J. Han, Y. Jamil, D. V. L. Norum, P. J. Tanner, and T. F. Gallagher, *Rb nf quantum defects from millimeter-wave spectroscopy of cold ^{85}Rb Rydberg atoms*, Phys. Rev. A **74**, 5 054502 (2006).

[38] M. L. Zimmerman, M. G. Littman, M. M. Kash, and D. Kleppner, *Stark structure of the Rydberg states of alkali-metal atoms*, Phys. Rev. A **20**, 6 2251 (1979).

[39] B. Carlson and G. Rushbrooke, *On the expansion of a Coulomb potential in spherical harmonics*, in *Mathematical Proceedings of the Cambridge Philosophical Society*, vol. 46, 626–633.

[40] R. J. Buehler and J. O. Hirschfelder, *Bipolar Expansion of Coulombic Potentials*, Phys. Rev. **83**, 3 628 (1951).

[41] R. J. LeRoy, *Long-Range Potential Coefficients From RKR Turning Points: C_6 and C_8 for $B(3\Pi_{0_u^+})$-State Cl_2, Br_2, and I_2*, Can. J. Phys. **52**, 3 246 (1974).

[42] A. Dalgarno and W. Davison, *The Calculation of Van Der Waals Interactions*, in D. Bates and I. Estermann, (Eds.) *Advances in Atomic and Molecular Physics*, vol. 2, 1 – 32, Academic Press (1966).

[43] M. Marinescu, *Dispersion coefficients for the nP-nP asymptote of homonuclear alkali-metal dimers*, Phys. Rev. A **56**, 6 4764 (1997).

[44] W. Press, S. Teukolsky, W. Vetterling, and B. Flannery, *Numerical Recipes in Fortran 77, The Art of Scientific Computing, Second Edition*, Cambridge University Press, New York, New York (1992).

[45] R. T. Pack, *Space-fixed vs body-fixed axes in atom-diatomic molecule scattering. Sudden approximations*, J. Chem. Phys. **60**, 2 633 (1974).

[46] R. Krems and A. Dalgarno, *Quantum-mechanical theory of atom-molecule and molecular collisions in a magnetic field: Spin depolarization*, J. Chem. Phys. **120**, 5 2296 (2004).

[47] T. Tscherbul, Y. Suleimanov, V. Aquilanti, and R. Krems, *Magnetic field modification of ultracold molecule-molecule collisions*, New J. Phys. **11**, 055021 1 (2009).

[48] T. Tscherbul and A. Dalgarno, *Quantum Theory of molecular collisions in a magnetic field: Efficient calculations based on the total angular momentum representation*, J. Chem. Phys. **133**, 184104 (2010).

[49] M. Viteau, M. Bason, J. Radogostowicz, N. Malossi, D. Ciampini, O. Morsch, and E. Arimondo, *Rydberg atoms in one-dimensional optical lattices*, arXiv:1103.4232v1 .

[50] V. Kokoouline, O. Dulieu, R. Kosloff, and F. Masnou-Seeuws, *Mapped Fourier methods for long-range molecules: Application to perturbations in the* $Rb_2(0_u^+)$ *photoassociation spectrum*, Journal of Chemical Physics **110**, 20 9865 (1999).

[51] I. I. Beterov, I. I. Ryabtsev, D. B. Tretyakov, and V. M. Entin, *Quasiclassical calculations of blackbody-radiation-induced depopulation rates and effective lifetimes of Rydberg* nS *,* nP *, and* nD *alkali-metal atoms with* $n \leq 80$, Phys. Rev. A **79**, 5 052504 (2009).

[52] A. Thiel, *The Landau-Zener effect in nuclear molecules*, J. Phys. G: Nucl. Part. Phys. **16** 867 (1990).

[53] J. R. Rubbmark, M. M. Kash, M. G. Littman, and D. Kleppner, *Dynamical effects at avoided level crossings: A study of the Landau-Zener effect using Rydberg atoms*, Phys. Rev. A **23**, 6 3107 (1981).

[54] C. Zener, *Non-Adiabatic Crossing of Energy Levels*, Proc. R. Lond. A **137** 696 (1932).

[55] N. Samboy, J. Stanojevic, and R. Côté, *Formation and properties of Rydberg macrodimers*, Phys. Rev. A **83**, 5 050501 (2011).

[56] H. Friedrich, *Theoretical Atomic Physics*, Springer-Verlag, Berlin Heidelberg (1990).

[57] M. Arndt, O. Nairz, J. Vos-Andreae, C. Keller, G. van der Zouw, and A. Zeilinger, *Wave-particle duality of* $C_6$0 *molecules*, Nature **401** 680 (1999).

[58] W. Marshall, C. Simon, R. Penrose, and D. Bouwmeester, *Towards Quantum Superpositions of a Mirror*, Phys. Rev. Lett. **91**, 13 130401 (2003).

[59] K. M. Jones, E. Tiesinga, P. D. Lett, and P. S. Julienne, *Ultracold photoassociation spectroscopy: Long-range molecules and atomic scattering*, Rev. Mod. Phys. **78**, 2 483 (2006).

[60] H. R. Thorsheim, J. Weiner, and P. S. Julienne, *Laser-induced photoassociation of ultracold sodium atoms*, Phys. Rev. Lett. **58**, 23 2420 (1987).

[61] J. Weiner, V. S. Bagnato, S. Zilio, and P. S. Julienne, *Experiments and theory in cold and ultracold collisions*, Rev. Mod. Phys. **71**, 1 1 (1999).

[62] W. C. Stwalley and H. Wang, *Photoassociation of Ultracold Atoms: A New Spectroscopic Technique*, Journal of Molecular Spectroscopy **195**, 2 194 (1999).

[63] R. Napolitano, J. Weiner, C. J. Williams, and P. S. Julienne, *Line Shapes of High Resolution Photoassociation Spectra of Optically Cooled Atoms*, Phys. Rev. Lett. **73**, 10 1352 (1994).

[64] J. L. Bohn and P. S. Julienne, *Semianalytic treatment of two-color photoassociation spectroscopy and control of cold atoms*, Phys. Rev. A **54**, 6 R4637 (1996).

[65] E. Taylor-Juarros, R. Côté, and K. Kirby, *Formation of ultracold polar molecules via Raman excitation*, Eur. Phys. J. D. **31**, 2 213 (2004).

[66] J. A. C. Weideman, *Numerical Integration of Periodic Functions: A Few Examples*, The American Mathematical Monthly **109**, 1 pp. 21 (2002).

[67] A. Ashkin, J. Dziedzic, J. Bjorkholm, and S. Chu, *Observation of a single-beam gradient force optical trap for dielectric particles*, Opt. Lett. **11**, 5 288 (1986).

[68] *Laser Cooling and Trapping of Atoms*, J. Opt. Soc. Am. B **6**, 11 2020 (1989).

[69] W. Petrich, M. H. Anderson, J. R. Ensher, and E. A. Cornell, *Stable, Tightly Confining Magnetic Trap for Evaporative Cooling of Neutral Atoms*, Phys. Rev. Lett. **74**, 17 3352 (1995).

[70] J. J. Tollett, C. C. Bradley, C. A. Sackett, and R. G. Hulet, *Permanent magnet trap for cold atoms*, Phys. Rev. A **51**, 1 R22 (1995).

[71] M. Anderson, J. Ensher, M. Matthews, C. Wieman, and E. Cornell, *Observation of Bose-Einstein Condensation in a Dilute Atomic Vapor*, Science **269**, 5221 198 (1995).

[72] C. C. Bradley, C. A. Sackett, J. J. Tollett, and R. G. Hulet, *Evidence of Bose-Einstein Condensation in an Atomic Gas with Attractive Interactions*, Phys. Rev. Lett. **75**, 9 1687 (1995).

[73] K. B. Davis, M. O. Mewes, M. R. Andrews, N. J. van Druten, D. S. Durfee, D. M. Kurn, and W. Ketterle, *Bose-Einstein Condensation in a Gas of Sodium Atoms*, Phys. Rev. Lett. **75**, 22 3969 (1995).

[74] J. N. Byrd, J. A. Montgomery, H. H. Michels, and R. Côté, *Potential energy surface of the 12A Li_2 + Li doublet ground state*, International Journal of Quantum Chemistry **109**, 13 3112 (2009).

[75] P. Soldán, M. T. Cvitaš, J. M. Hutson, P. Honvault, and J.-M. Launay, *Quantum Dynamics of Ultracold Na + Na_2 Collisions*, Phys. Rev. Lett. **89**, 15 153201 (2002).

[76] L. P. Parazzoli, N. J. Fitch, P. S. Żuchowski, J. M. Hutson, and H. J. Lewandowski, *Large Effects of Electric Fields on Atom-Molecule Collisions at Millikelvin Temperatures*, Phys. Rev. Lett. **106**, 19 193201 (2011).

[77] W. T. Zemke, J. N. Byrd, H. H. Michels, J. John A. Montgomery, and W. C. Stwalley, *Long range intermolecular interactions between the alkali diatomics Na_2, K_2 and NaK*, J. Chem. Phys. **132**, 244305 (2010).

[78] J. N. Byrd, J. A. Montgomery, and R. Côté, *Structure and thermochemistry of K_2Rb, KRb_2, and K_2Rb_2*, Phys. Rev. A **82**, 1 010502 (2010).

[79] S. T. Rittenhouse and H. R. Sadeghpour, *Ultracold Giant Polyatomic Rydberg Molecules: Coherent Control of Molecular Orientation*, Phys. Rev. Lett. **104**, 24 243002 (2010).

[80] I. C. H. Liu and J. M. Rost, *Polyatomic molecules formed with a Rydberg atom in an ultracold environment*, Eur. Phys. J. D **40**, 65 65 (2006).

[81] I. C. H. Liu, J. Stanojevic, and J. M. Rost, *Ultra-Long-Range Rydberg Trimers with a Repulsive Two-Body Interaction*, Phys. Rev. Lett. **102**, 17 173001 (2009).

[82] J. Jackson, *Classical Electrodynamics, 3rd ed.*, John Wiley & Sons, Inc., New York, New York, United States of America (1998).

[83] M. E. Rose, *The Electrostatic Interaction of Two Arbitrary Charge Distributions*, J. Phys. Math **37** 215 (1958).